

# Development of Higher Borides and Heusler Alloys as High and Low Temperature Thermoelectric Materials

SAUERSCHNIG Philipp

February 2020

Development of Higher Borides and Heusler Alloys as  
High and Low Temperature Thermoelectric Materials

SAUERSCHNIG Philipp

Doctoral Program in Materials Science and Engineering

Submitted to the Graduate School of  
Pure and Applied Sciences  
in Partial Fulfillment of the Requirements  
for the Degree of Doctor of Philosophy in  
Engineering

at the  
University of Tsukuba

## **Acknowledgements**

I wish to express my gratitude to Prof. Dr. Takao Mori for giving me the opportunity to work on this PhD thesis under his supervision. I want to thank him for his scientific insight shared throughout the course of my time as a student under his guidance. I also want to show my appreciation for his continued support and encouragement which made it possible to get through the challenging aspects of my studies and helped me grow as a researcher.

I would also like to thank Dr. Jean-Baptiste Vaney who helped me greatly as an instructor in both experimental and theoretical questions even long past the end of his time as a researcher in our group. He was always open for discussion and ready to offer scientific advice.

I wish to thank Dr. Naohito Tsujii for his help with the preparation and guidance with the low temperature measurements of magnetic and thermoelectric properties.

I want to thank Dr. Takaho Tanaka for his support and sharing his experience while learning single crystal growth on the optical floating zone apparatus.

I wish to thank the members of the PhD committee, Prof. Yoshikazu Suzuki, Prof. Seiji Mitani and Prof. Naoki Fukata for their kind advice for the improvement of my PhD thesis.

I want to thank Dr. Yuichi Michiue for his crystal structure refinements and analysis of the  $\text{YbB}_{66}$  and  $\text{SmB}_{66}$  single crystals.

I would like to thank Prof. Dr. S. Yin for the hardness measurements on  $\text{YbB}_{66}$ , Dr. Iwanade Akio and Dr. Takenouchi Satoshi for the ICP-AES measurements of  $\text{REB}_{66}$  samples and Keiko Suzuta for the specific heat measurements of  $\text{SmB}_{66}$  by DSC. I want to thank Dr. Shiro Funahashi, Dr. Naoto Hirosaki and Dr. Yoshitaka Matsushita for the measurement of single-crystal X-ray diffraction on  $\text{YbB}_{66}$  and  $\text{SmB}_{66}$  single crystals.

I wish to thank Dr. Joshua Watts for the preparation of the high purity boron carbide and the analysis of the boron carbide powders by Rietveld refinement of the XRD patterns.

I also want to thank the members of our laboratory, postdoctoral researchers and students, who I was able to work with and who were always supportive and helped create a pleasant working environment.

I also wish to thank Erika Arisumi-Guelou, Sayaka Latumeten, Yuki Yoshioka and Xiaoyin Wang for their kind support with the many administrative tasks that arose during my time in Japan.

Finally, I want to thank my family and friends for their support and belief in me. Without you I would not have been able to make it. I am grateful to have you in my life despite the current spatial separation.

## Thesis Outline

This thesis deals with the development of thermoelectric materials which can directly convert heat into electrical energy through the so called Seebeck effect. Thermoelectric materials are characterized by the figure of merit  $ZT = \frac{\alpha^2}{\rho \cdot \kappa} T$  with  $\alpha$ ,  $\rho$  and  $\kappa$  being the Seebeck coefficient, the electrical resistivity and the thermal conductivity respectively. To maximize the thermoelectric performance, the Seebeck coefficient should be high while the electrical resistivity needs to be as low as possible. The interrelated nature of these properties makes the development of efficient thermoelectric materials a challenging task. Different thermoelectric materials have different temperatures at which their performance is maximized.[1,2] Depending on the intended application, the appropriate material needs to be selected. So far thermoelectric generators for waste heat recovery, for example in cars, has not been successfully commercialized due to insufficient efficiency and high material cost. [3] For this purpose, we decided to investigate the so far less explored temperature ranges of thermoelectric research.

Higher borides possess properties (high Seebeck coefficient, low thermal conductivity, high thermal stability) [4,5] that make them interesting materials for potential high temperature ( $T > 850$  K) applications, for instance in thermal power plants ( $T > 1500$  K).[6] Recently relatively good thermoelectric properties were reported for  $\text{SmB}_{66}$  and  $\text{YB}_{48}$  which motivated us to look further into  $\text{REB}_{66}$  compounds.[7,8] Boron carbide, the highest performance higher boride thermoelectric material was investigated in the course of this thesis.[9]

Full Heusler alloys are of interest as low temperature ( $T < 450$  K) thermoelectric materials.[10] Possible applications include powering IoT devices, e.g. sensing devices wirelessly connected to a network. [11]

Chapter 1 gives a short introduction to thermoelectricity and the challenges in the development of materials for thermoelectric application. The physical properties central to thermoelectrics are being briefly discussed. This chapter also contains an overview over the state of research on the investigated materials, i.e. higher boride materials in general as well as  $\text{REB}_{66}$  and boron carbide in particular as well as Heusler alloys. An overview of the most relevant experimental techniques for the synthesis and measurement of physical properties utilized in the course of this work is given.

Chapter 2 contains the results of the study of  $\text{YbB}_{66}$  single crystals grown by the optical floating zone method. Previous work on  $\text{SmB}_{66}$  suggested that mixed valence  $\text{Sm}(+2)/\text{Sm}(+3)$  might be responsible for the enhanced thermoelectric properties compared to  $\text{YB}_{66}$ . Mixed valence was reported for  $\text{YbB}_{12}$  [12] so  $\text{YbB}_{66}$  was chosen for the investigation of this phenomenon. The results of the magnetic susceptibility and the effective magnetic moment suggest a trivalent oxidation state for Yb in  $\text{YbB}_{66}$ . However, the thermoelectric properties of  $\text{YbB}_{66}$  are quite similar to those of  $\text{SmB}_{66}$ . A figure of merit  $ZT = 0.1$  at 973 K was achieved for  $\text{YbB}_{66}$  which is very close to those reported for  $\text{SmB}_{66}$  and  $\text{YB}_{48}$  ( $\text{YB}_{66}$  with a high Y content). The chemical analysis and the single crystal structure refinement independently found a composition richer in Yb. The single crystal structure refinement of  $\text{YbB}_{66}$  and  $\text{SmB}_{66}$  is also discussed in this chapter.

Chapter 3 is dedicated to the work on polycrystalline  $\text{REB}_{66}$ . The difficulties of the floating zone single crystals growth required the exploration of alternative synthesis methods. It was possible to obtain  $\text{REB}_{66}$  with high density (close to 100% of the theoretical density) and with little to no secondary phases. The process includes the borothermal reduction of the reactants (amorphous boron and rare earth oxide powders) in an HF induction furnace, arc melting to form the  $\text{REB}_{66}$  phase and densification of the hand milled powder by spark plasma sintering. Surprisingly, the thermoelectric properties of the sintered polycrystalline samples were found to be comparable to the single crystalline samples prepared by the optical floating zone. Typically, single crystalline materials have lower electrical resistivity and higher thermal conductivity due to reduced scattering of charge carriers and phonons compared to polycrystalline materials. This can most likely be attributed to the complex crystal structure of  $\text{REB}_{66}$ . The results suggest that mainly differences in composition lead to differences in the thermoelectric properties instead of differences due to different rare earth elements.

Chapter 4 is about the investigation of phase pure boron carbide ( $\text{B}_{4.05}\text{C}$ ) which was synthesized by a solution-based process. Typical boron carbide made by conventional methods (carbothermal reaction at high temperatures) contains free carbon as an impurity phase and boron-rich boron carbide secondary phases.[13] The sintering and the thermoelectric properties of this phase pure boron carbide and commercially available powders are discussed in this chapter. So far there is no consensus on the mechanism of electrical conduction in boron carbide.[14,15] Different models have been discussed based on the results of the temperature dependences of the measured electrical resistivity and Seebeck coefficient.

Chapter 5 deals with the investigation of the spin fluctuation enhancement of the Seebeck coefficient in the Full Heusler alloy  $\text{Fe}_2\text{VAl}$  for low temperature applications. For this purpose, weakly ferromagnetic  $\text{Fe}_2\text{V}_{1-x}\text{M}_x\text{Al}$  ( $\text{M} = \text{Co}, \text{Mn}$ ;  $x = 0.1 - 0.3$ ) samples were synthesized by arc melting and spark plasma sintering. The transport properties were measured in the temperature range 10 – 373 K with and without an applied magnetic field. Applying a magnetic field can suppress the spin fluctuation and its contribution to the Seebeck coefficient can be estimated from the comparison with the measurement without magnetic field. The Seebeck enhancement is largest around the Curie temperature. [16] Therefore, the first objective was to find a material with a Curie temperature close to room temperature. An increase of the Curie temperature with increased Co content was observed which was accompanied by a shift of the Seebeck enhancement maximum. However, the thermoelectric performance was greatly reduced which will make further optimization necessary.

# Table of Contents

<b>Acknowledgements</b>	<b>1</b>
<b>Thesis Outline</b>	<b>2</b>
<b>Chapter 1: Introduction</b>	<b>7</b>
<b>1.1 Thermoelectricity</b>	<b>7</b>
<b>1.2 Thermoelectric Materials</b>	<b>11</b>
1.2.1 Higher Borides	11
1.2.1.2 REB <sub>66</sub>	12
1.2.1.4 Boron carbide	14
1.2.2 Full Heusler Fe <sub>2</sub> VAl	16
<b>1.3 Experimental Techniques</b>	<b>19</b>
1.3.1 Sample Preparation	19
1.3.1.1 Optical Floating Zone	19
1.3.1.2 Spark Plasma Sintering	21
1.3.2 Physical Properties Measurements	23
1.3.2.1 Seebeck Coefficient and Electrical Resistivity Measurement	23
1.3.2.2 Thermal Conductivity Measurement	25
1.3.2.3 Magnetic Properties Measurement	27
<b>Chapter 2: Physical Properties (RE = Yb) and Crystal Structure (RE = Sm, Yb) of Higher Boride REB<sub>66</sub> Single Crystals</b>	<b>28</b>
<b>2.1 Introduction</b>	<b>28</b>
<b>2.2 Experimental</b>	<b>29</b>
<b>2.3 Results and Discussion</b>	<b>30</b>
2.3.1 Density, Chemical Composition and Surface XRD	30
2.3.2 Single Crystal XRD	32
2.3.3 Magnetic Properties	38
2.3.4 Thermoelectric Properties	39
<b>2.4 Conclusion</b>	<b>46</b>
<b>2.5 Acknowledgements</b>	<b>47</b>
<b>Chapter 3: Thermoelectric and Magnetic Properties of Spark Plasma Sintered REB<sub>66</sub> (RE = Y, Sm, Ho, Tm, Yb)</b>	<b>48</b>
<b>3.1 Introduction</b>	<b>48</b>
<b>3.2 Experimental</b>	<b>48</b>
<b>3.3 Results and Discussion</b>	<b>50</b>
3.3.1 Characterization REB <sub>66</sub> Prepared by Spark Plasma Sintering	50

3.3.2 Magnetic Properties	55
3.3.3 Thermoelectric Properties	58
<b>3.4 Conclusion</b>	<b>64</b>
<b>3.5 Acknowledgement</b>	<b>64</b>
<b>Chapter 4: Thermoelectric Properties of Phase Pure Boron Carbide Prepared by a Solution-Based Method</b>	<b>65</b>
<b>4.1 Introduction</b>	<b>65</b>
<b>4.2 Experimental</b>	<b>65</b>
4.2.1 Synthesis	65
4.2.2 Characterization	66
4.2.3 Sintering	66
4.2.4 Physical Properties Measurements	67
<b>4.3 Results and Discussion</b>	<b>68</b>
4.3.1 Powder Characterization	68
4.3.2 Characterization After Sintering	70
4.3.3 Electrical Properties	73
4.3.4 Thermal Properties	79
4.3.5 Figure of Merit	81
<b>4.4 Conclusion</b>	<b>81</b>
<b>4.5 Acknowledgements</b>	<b>82</b>
<b>Chapter 5: Study of Seebeck Enhancement by Spin Fluctuation in Ferromagnetic <math>\text{Fe}_2\text{V}_{1-x}\text{M}_x\text{Al}_{1-y}</math> (M=Mn, Co) Full Heusler Alloys</b>	<b>83</b>
<b>5.1 Introduction</b>	<b>83</b>
<b>5.2 Experimental</b>	<b>83</b>
<b>5.3 Results and Discussion</b>	<b>85</b>
5.3.1 Characterization	85
5.3.2 Magnetic Properties	87
5.3.3 Thermoelectric Properties	88
<b>5.4 Conclusion</b>	<b>92</b>
<b>5.5 Acknowledgements</b>	<b>93</b>
<b>Conclusion and Outlook</b>	<b>94</b>
<b>List of Publications</b>	<b>96</b>
<b>List of Figures</b>	<b>97</b>

<b>List of Tables</b>	<b>102</b>
<b>List of Abbreviations</b>	<b>103</b>
<b>List of Physical Quantities, Natural Constants and Their Units</b>	<b>104</b>
<b>References</b>	<b>106</b>

## Chapter 1: Introduction

### 1.1 Thermoelectricity

Thermoelectric materials are able to generate an electrical voltage from temperature gradients and can be used to convert heat into electrical energy through the Seebeck effect, named after T.J. Seebeck [17] who first observed this phenomenon in 1821. He found that the needle of a compass was deflected when one end of a connected pair of different metals (e.g. copper, gold, platinum) was heated.[1] Thermoelectric modules generally consist of pairs of p- and n-type materials. When heat is supplied to one end of this pair high energy/entropy charge carriers (holes and electrons respectively) move from the hot side to the cold side of the material. [18] This induces a voltage  $\Delta V$  along the material according to

$$\Delta V = \alpha \Delta T \quad (1.1)$$

with  $\alpha$  and  $T$  being the Seebeck coefficient and temperature respectively. Alternatively, heat can either be absorbed or released at the junction of two different materials when a current is run through it, depending on the direction of the current. [1] This is the so called Peltier effect given by

$$\pi = \frac{\dot{Q}}{I} \quad (1.2)$$

with  $\pi$ ,  $\dot{Q}$  and  $I$  being the Peltier coefficient, the absorbed or released heat per unit time and the electrical current. The two effects were found to be related through [1]

$$\pi = \alpha T \quad (1.3)$$

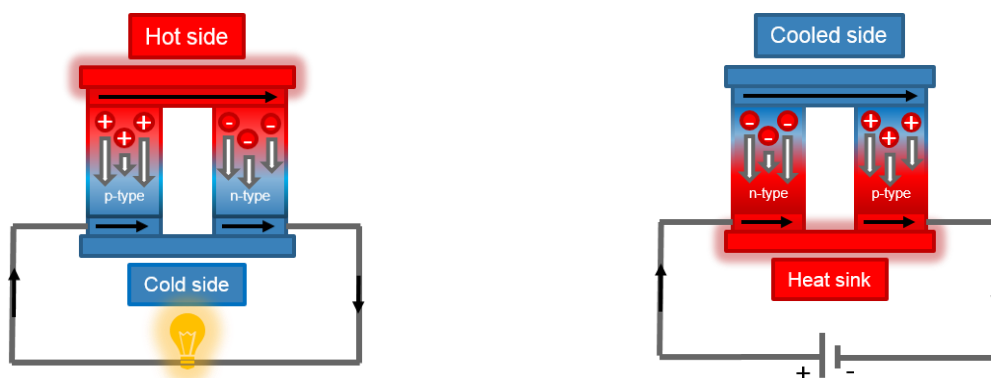


**Figure 1.1** Thermoelectric generator (left) and Peltier element (right)

Thermoelectric materials are generally evaluated using the dimensionless figure of merit

$$ZT = \frac{\alpha^2 T}{\rho (\kappa_l + \kappa_e)} \quad (1.4)$$

with  $\alpha$ ,  $\rho$ ,  $\kappa_l$  and  $\kappa_e$  being the Seebeck coefficient, the electric resistivity and the lattice and electrical part of the thermal conductivity. [19] It can be seen from the equation for the figure of merit that a good thermoelectric material should possess a high Seebeck coefficient ( $> 100\mu\text{V K}^{-1}$ ), low electrical resistivity and low thermal conductivity. Achieving such properties is the challenge of the development of thermoelectric materials. There are many approaches that have been employed to enhance the thermoelectric properties of different materials. [1,18,20–23]

All of the aforementioned physical properties depend very strongly on the charge carrier concentration of the material.[22] The general trend for each property can be seen in Figure 1.2.

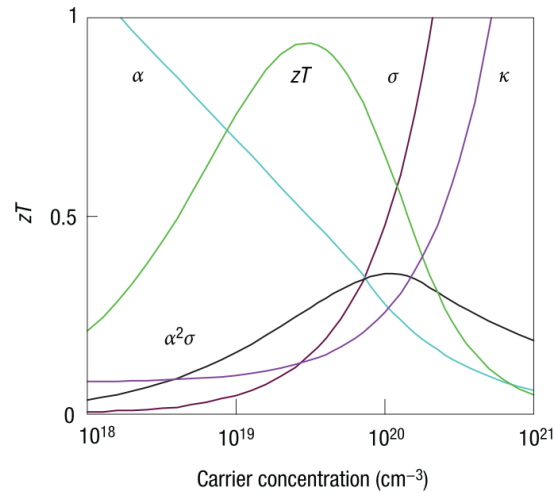


**Figure 1.2** Carrier concentration dependence of the thermoelectric properties. Copyright Nature Publishing Group[22]

The Figure of Merit  $ZT$  shows a maximum for materials with a carrier concentration that falls somewhere in the range of  $10^{19} - 10^{20} \text{ cm}^{-3}$  which means that generally heavily doped semiconductors are the most promising materials for high thermoelectric performance.[1]

The Seebeck coefficient for metals and degenerate semiconductors can be approximated by

$$\alpha = \frac{8\pi^2 k_B^2}{3eh^2} m^* T \left(\frac{\pi}{3n}\right)^{2/3} \quad (1.5)$$

with  $m^*$  and  $n$  being the effective mass of the charge carrier and the carrier concentration respectively. [22] A low carrier concentration and high effective mass therefore are beneficial to achieve a high Seebeck coefficient.

On the other hand, the electrical conductivity  $\sigma$  is given by

$$\sigma = n e \mu \quad (1.6)$$

with  $e$  and  $\mu$  being the elemental charge and the charge carrier mobility respectively. [22] The electrical conductivity increases with increasing charge carrier concentration and mobility.

The Figure of Merit  $ZT$ , more precisely the average  $ZT$ , is directly related to the thermal-electrical conversion efficiency  $\eta$ . [19] The efficiency is defined as the fraction of heat that can be converted into work and can be calculated from

$$\eta = \frac{T_h - T_c}{T_h} \frac{\sqrt{1 + \overline{ZT}} - 1}{\sqrt{1 + \overline{ZT}} + \frac{T_c}{T_h}} \quad (1.7)$$

with  $T_h$  and  $T_c$  being the temperature at the hot and cold end of the module respectively. [1] The theoretical maximum efficiency of a thermoelectric generator is the Carnot-efficiency

$$\eta_{Carnot} = \frac{T_h - T_c}{T_h} \quad (1.8)$$

which depends solely on the temperature difference between the hot and cold reservoir. This theoretical maximum efficiency can however not be realized in practice. Figure 1.3 shows the actual conversion efficiencies of different kinds of heat engines.

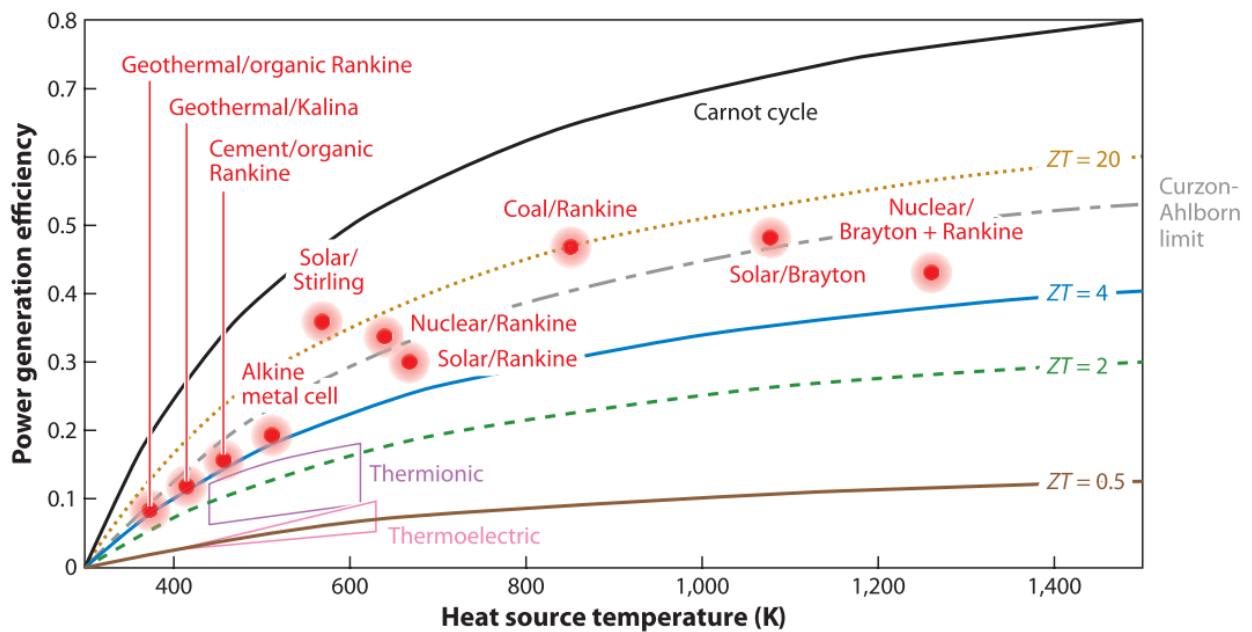


**Figure 1.3** Conversion efficiency for several types of heat engines with  $T_{cold} = 300$  K.

Copyright by Annual Reviews [18]

Both an increase in the Figure of Merit  $ZT$  and the temperature difference increase the thermal-electrical conversion efficiency. Currently the highest performance thermoelectric materials reach a conversion efficiency of roughly 10%.[24] Compared to established technology this value is still low. It is therefore necessary to find areas for application in which the advantages of thermoelectric materials (high reliability for long term operation without maintenance thanks to the lack of moving parts) can be leveraged.

An example of this are RTG (Radioisotope thermoelectric generators) which are used in space missions lasting several decades. [25] These RTGs consist of a radioactive heat source, for example  $^{238}\text{PuO}_2$ , and thermoelectric modules which convert the heat into electric energy. In most cases PbTe and SiGe based materials were used for the materials achieving conversion efficiencies close to 7%.

## 1.2 Thermoelectric Materials

### 1.2.1 Higher Borides

Several higher borides or icosahedral borides (i.e. compounds with  $B_{12}$  icosahedra as basic structural elements) have been investigated in the past for the potential application as high-temperature thermoelectric materials. [4,5] Higher borides are in general materials with several physical properties that are advantageous for this purpose. Among these properties are high Seebeck coefficients, low density, high melting temperatures (easily exceeding 2000 K), and high hardness. [26,27] However, there are also several drawbacks that have to be overcome. Due to the electron deficient nature of the  $B_{12}$  icosahedra, which make up their basic framework, higher boride materials are in general p-type semiconductors. Thermoelectric generators generally require both p- and n-type legs for the highest efficiency. There have however been efforts to develop uni-leg thermoelectric modules with geometries that work with a single leg type which could help to overcome this issue. [28] Alternatively, icosahedral borides with n-type conduction have been found and investigated, namely RE-B-C-(N) and YAIB<sub>14</sub>. [29,30] The ideal structure of  $\alpha$ -rhombohedral boron is a semiconductor, all other compounds built from  $B_{12}$  icosahedra are predicted to be metallic in character. However, high amounts of defects in the structures (e.g. atomic site vacancies, Jahn-Teller distortion) result in semiconducting behavior. [15,31–33] The bonding in  $B_{12}$  icosahedra can be described as each boron atom at the vertices of the  $B_{12}$  icosahedron supplying one electron to external bonds, leaving a total of 24 electrons for internal bonds for 13 bonding orbitals. This results in a deficiency of 2 electrons. [33–36]

The thermal properties of higher borides stand out for their unusual characteristics and have been studied intensively in the past. [37–39] A study on crystals of  $\beta$ -rhombohedral boron,  $B_{12}P_2$ ,  $B_{12}As_2$  and  $YB_{66}$  showed the general trend of increasing thermal conductivity with the increasing complexity of the crystal structures. Between  $\alpha$ -rhombohedral boron (here the structurally related compounds  $B_{12}P_2$  and  $B_{12}As_2$  have been investigated due to experimental difficulties in the synthesis of  $\alpha$ -rhombohedral boron crystals of suitable size for the necessary measurements) over  $\beta$ -rhombohedral boron to  $YB_{66}$  the number of atoms in the primitive unit cell increases from 12 to 402 atoms. [39] Due to the low charge carrier concentrations in these materials [37] heat conduction can be described to almost exclusively occur by phonons. Experimentally thermal conductivities at 300 K of  $120 \text{ W m}^{-1} \text{ K}^{-1}$ ,  $38 \text{ W m}^{-1} \text{ K}^{-1}$ ,  $26 \text{ W m}^{-1} \text{ K}^{-1}$  and  $2 \text{ W m}^{-1} \text{ K}^{-1}$  were observed for  $B_{12}As_2$ ,  $B_{12}P_2$ ,  $\beta$ -rhombohedral boron (anisotropy in the thermal conductivity is low at 300 K with  $\lambda_{\parallel}/\lambda_{\perp} \approx 1.1$ ) and  $YB_{66}$  respectively, supporting the previous argument connecting complexity of the crystal structure and thermal conductivity. Additionally, it is found that the fraction of phonon energies in the acoustic branch which are responsible for heat conduction decreases from  $B_{12}As_2$ ,  $B_{12}P_2$  over  $\beta$ -rhombohedral boron to  $YB_{66}$ . [39]

Figure 1.4 shows an overview of the  $ZT$  values for different higher boride which have been investigated up to this point. It can be seen that the majority of materials are p-type due to the electron deficient nature of  $B_{12}$ -icosahedra as mentioned previously.

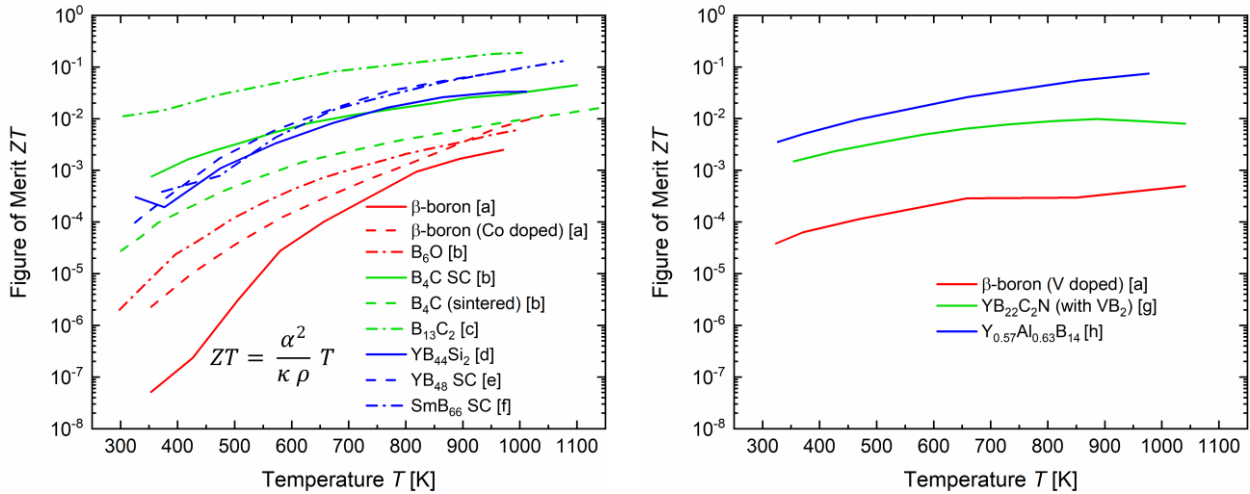


**Figure 1.4** Literature  $ZT$  values for higher boride materials. References: [a] H.K. Kim et al. [40], [b] T. Akashi et al. [41], [c] J.-L. Innocent et al. [42], M.A. Hossain et al. [43], [e] M.A. Hossain et al. [8], [f] A. Sussardi et al. [7], [g] A. Prytuliak et al. [44], [h] S. Maruyama et al. [30].

### 1.2.1.2 REB<sub>66</sub>

The compound YB<sub>66</sub> was originally discovered in 1960. [45] Its crystal structure was first solved by Richards and Kaspar in 1969. [46] They described the structure to belong to the cubic crystal system with a large lattice parameter  $a = 23.440 \text{ \AA}$  and the space group  $Fm\bar{3}c$ . In total there were 1584 boron atoms and 24 yttrium atoms found in the unit cell consisting of an icosahedral framework with units of 12 B<sub>12</sub> icosahedra connected to a central icosahedron making up units of 156 atoms (B1 to B9). The unit cell contains 8 of these units leading to a total of 1248 boron atoms. There are channels in the structure of this framework parallel to the fourfold axes at  $x \frac{1}{4} \frac{1}{4}$  with Y atoms in these channels in the  $8a \ 0.05448 \ \frac{1}{4} \frac{1}{4}$  positions in pairs of two. However, due to the short interatomic distance of 1.955 Å of the two Y atoms in these positions it is expected that only one position is filled at a time, leading to an occupancy of 0.5. Within the same channels, above and below the Y positions, there are cage-like arrangements formed (B10 to B13) which are also only partially occupied. The Y atoms are coordinated by up to 12 boron atoms. The structure model was later modified by Slack et al. [47] due to inconsistencies between the measured density of the investigated YB<sub>66</sub> crystal and the theoretical density calculated from the lattice parameter determined by X-ray diffraction. Slack et al. described the model with  $1628 \pm 4$  boron atoms per unit cell (in 8 units of (B<sub>12</sub>)<sub>13</sub> units and 8 clusters of 48 boron atoms each) compared to Richards and Kaspar's [46]  $1584 \pm 48$  boron atoms per unit cell. Additionally, the number of Y atoms was adjusted to 26.4 atoms per unit cell (from 24 Y atoms proposed by Richards and Kaspar [46]) for a composition of YB<sub>61.75</sub> and an occupancy of 0.55 in the Y position. In this model the number of boron atoms is almost constant for different compositions and only the Y occupancy changes. If the Y occupancy exceeds 0.5 both positions of the Y-Y pairs need to be occupied in some cases which is expected to cause distortion or expansion of the boron framework in the vicinity.

Further work on the structure model of  $\text{YB}_{66}$  was done for crystals of more metal-rich compositions of  $\text{YB}_{62}$  and  $\text{YB}_{56}$  by Higashi and Kobayashi.[48] It was found that with the increase in Y content, the boron framework changed little, but the occupancy in the Y position increased from 0.5 for  $\text{YB}_{66}$  [46] to 0.532(4) for  $\text{YB}_{62}$  and 0.575(5) for  $\text{YB}_{56}$ . Y was assumed to exist as  $\text{Y}^{3+}$  ions for the structure refinement. With increasing Y occupancy an increase in the anisotropy of the atomic displacement parameters and the interatomic distance between the atoms of the Y-Y pair was observed. This is consistent with the expected repulsion of  $\text{Y}^{3+}$  pairs when the site occupancy exceeds 50%. Tanaka et al. [49] introduced a split position for Y (Y1 in 0.0546(3)  $\frac{1}{4}$   $\frac{1}{4}$  with occ.=0.442 and Y2 in 0.0736(2)  $\frac{1}{4}$   $\frac{1}{4}$  with occ.=0.0638) to describe cases in which either one or both positions of the Y-Y pair are occupied.

Schwetz et al. did a systematic study on the existence of compounds of the  $\text{YB}_{66}$  structure type of all lanthanides and the actinides Th and Pu. [50] The  $\text{REB}_{66}$  (RE = rare earth) structure was found for all investigated elements with the exception of La, Ce, Pr, Nd and Eu. The criterion for the existence of  $\text{REB}_{66}$  was described to be related to the atomic radius of the elements.  $\text{REB}_{66}$  was found to exist for atomic radii  $1.73 \text{ \AA} < r < 1.82 \text{ \AA}$ .

The earliest reports of the physical properties of  $\text{REB}_{66}$  were done in 1971 by Oliver and Brower on crystals grown from a water-cooled metal crucible with RF heating. [51,52] The  $\text{YB}_{66}$  phase was described to melt congruently at roughly 2373 K and to form eutectics with both  $\text{YB}_{12}$  as well as  $\beta$ -rhombohedral boron. The congruent composition was estimated to be close to  $\text{YB}_{62}$  to  $\text{YB}_{64}$ . They found the thermal conductivity to be  $2 \text{ W m}^{-1} \text{ K}^{-1}$  at room temperature and described it to be similar to that of glasses. The Debye temperature  $\theta = 1300 \text{ K}$  was calculated from the elastic constants.[51] Further studies were carried out in 1977 by Slack et al. [47] on  $\text{YB}_{66}$  crystals grown by Oliver and Bower. [53] Measurements of the electrical resistivity of  $\text{YB}_{66}$  samples with compositions ranging from  $\text{YB}_{61}$  to  $\text{YB}_{66}$  showed little compositional dependence and resulted in  $\rho = 3.6 \text{ \Omega m}$  at room temperature. They described the material as p-type in all cases with low mobility hopping type conduction.

The first reports of the thermoelectric properties of  $\text{REB}_{66}$  compounds (RE=Y, Sm, Gd, Dy, Yb) showed overall relatively low performance. [37,54] The temperature dependence of the electrical conductivity and Seebeck coefficient were measured up to high temperatures for  $\text{SmB}_{66}$  (Seebeck coefficient  $\alpha \approx 60 \text{ \mu V K}^{-1}$  and electrical conductivity  $\sigma \approx 180 \text{ \Omega}^{-1} \text{ cm}^{-1}$  at 1110 K giving a power factor  $pf = \alpha^2 \sigma \approx 0.06 \text{ mW m}^{-1} \text{ K}^{-2}$ , values were estimated from the graphs in [54]) and  $\text{DyB}_{66}$  (Seebeck coefficient  $\alpha \approx 200 \text{ \mu V K}^{-1}$  and electrical conductivity  $\sigma \approx 22 \text{ \Omega}^{-1} \text{ cm}^{-1}$  at 1060 K giving a power factor  $pf = \alpha^2 \sigma \approx 0.09 \text{ mW m}^{-1} \text{ K}^{-2}$ , values were estimated from the graphs in [37]) Due to common dependencies of the Seebeck coefficient and electrical conductivity on the charge carrier concentration determined from Hall measurements of it was determined that  $\text{REB}_{66}$  should be analogous materials.

Later on, the influence of doping with Nb on the thermoelectric properties of  $\text{YB}_{66}$  single crystals grown by the optical floating zone technique was investigated. [55] The Nb atoms substituted B-B dumbbells in the  $\frac{1}{4} \frac{1}{4} \frac{1}{4}$  position and occupancies up to 97% were achieved. The Nb doping lead to an overall decrease of the electrical

resistivity and Seebeck coefficient compared to undoped YB<sub>66</sub> at lower temperatures. Noteworthy is the very high value of the Seebeck coefficient ( $\alpha \approx 750 \mu\text{V K}^{-1}$  of the undoped YB<sub>66</sub> at 323 K) compared to previous reports of REB<sub>66</sub> compounds. [37,54] Overall the thermoelectric properties could not be improved by the introduction of Nb. Conversely, the substitution of the B-B dumbbell in the  $\frac{1}{4}\frac{1}{4}\frac{1}{4}$  position, which is argued to be a phonon scattering center partly responsible for the amorphous-like thermal conductivity in YB<sub>66</sub>, lead to an increase in the thermal conductivity by a factor of 2 at room temperature. [49] The addition of carbon (YB<sub>66</sub>C<sub>0.6</sub>) lowered the resistivity and Seebeck coefficient at lower temperatures similarly to the Nb doping. The high temperature thermoelectric properties are almost identical to the undoped YB<sub>66</sub>. Due to a reduction in the thermal conductivity the  $ZT$  was estimated to increase by a factor of 2 throughout the whole temperature range. [56] SmB<sub>66</sub> crystals grown by the optical floating zone technique [7] showed surprisingly good thermoelectric properties compared to previously studied REB<sub>66</sub> compounds reaching a power factor  $pf = 0.3 \text{ mW m}^{-1} \text{ K}^{-2}$  and  $ZT = 0.13$  at 1050 K. These values are significantly higher than the previous reports of YB<sub>66</sub> [56] grown by the same crystal growth technique as well as other REB<sub>66</sub>. [37,54] Compared to YB<sub>66</sub>, SmB<sub>66</sub> had a significantly reduced electrical resistivity throughout the whole temperature range by roughly 2 orders of magnitude with similar values in the Seebeck coefficient. The value of the effective magnetic moment derived from the measurement of the temperature dependent magnetic susceptibility of SmB<sub>66</sub> was interpreted to be connected to (Sm(+2)/Sm(+3)) mixed valence. This was suspected to be responsible for the enhancement in the thermoelectric properties. Around the same time a similar enhancement was achieved in YB<sub>66</sub> through the realization of a very metal-rich composition YB<sub>48</sub> [8] through optical floating zone single crystal growth. Similar to SmB<sub>66</sub> a  $ZT = 0.1$  at 990 K could be realized. Unlike in the case of SmB<sub>66</sub>, the origin of the enhancement appears to be related to the change towards a metal-rich composition. An additional Y site to the previous reports of YB<sub>56</sub> and YB<sub>62</sub> was introduced for the single crystal XRD structure refinement. Similar to the Nb doping mentioned before [56] the additional Y replaces the B-B dumbbell formed by the B13 atoms in the  $\frac{1}{4}\frac{1}{4}\frac{1}{4}$  position. However, the occupancy of Y in this position is very low (0.15) and the thermal conductivity did not increase significantly compared to YB<sub>66</sub>. Delocalization of the charge carriers from the determination of the localization length  $\xi$  which increased from  $\xi = 0.56 \text{ \AA}$  for YB<sub>66</sub> to  $\xi = 2.14 \text{ \AA}$  for YB<sub>48</sub>.

#### 1.2.1.4 Boron carbide

Boron carbide has a rhombohedral crystal structure with two distinct structural units in the unit cell: B12 icosahedra connected by chains of three atoms. Originally C-C-C chains [57] were proposed but following studies showed that C-B-C chains [58] are a better description. The boron carbide phase was found to exist within a wide homogeneity range from roughly 8.6 – 18.8 at.% carbon. [59] The most carbon rich composition has been reported to be B<sub>4.3</sub>C, not B<sub>4</sub>C. [59] Early phase diagram investigations suggested the existence of separate boron- and carbon-rich boron carbide phases. The current consensus appears to be that there is only one thermodynamically stable boron carbide phase which melts congruently at a composition of 13.3 – 18.5 at.% carbon. [60] Lattice parameter of the hexagonal unit cell vary depending on the composition,  $a = 5.607 \text{ \AA} / c = 12.095 \text{ \AA}$  and  $a = 5.651 \text{ \AA} / c = 12.196 \text{ \AA}$  for the carbon-rich and boron-rich ends of the

homogeneity region respectively. [61] The crystal structure of boron carbide is characterized by a high amount of defects including B/C substitution in the icosahedra giving  $B_{12}$ ,  $B_{11}C$ ,  $B_{10}C_2$  and chains with B/C substitution (examples are  $-C-B-C-$ ,  $-C-C-B-$  or  $-C-C-C-$ ) or vacancies leading to boron carbides of different compositions.[62] The positions of boron and carbon atoms are difficult to unambiguously identify due to the very similar behavior of boron and carbon atoms in X-Ray and neutron diffraction.[62]

The thermoelectric properties of boron carbide vary very strongly with the composition of the phase. [9,63] A maximum in the electrical conductivity of boron carbide has been reported for compositions of 13.3 at.% [64] and 13.5% [15]. Seebeck coefficients have been reported in a range of typically  $150 - 300 \mu V K^{-1}$  with a minimum close to the composition where the electrical conductivity is maximized. [9,63]

The thermal conductivity has a maximum at the highest carbon content (up to  $30 W m^{-1} K^{-1}$  at 400 K for single crystalline [63] and at 300 K for hot-pressed [9] carbon-rich boron carbide). Increasing the boron content reduces the thermal conductivity of boron carbides dramatically to values below  $10 W m^{-1} K^{-1}$ . [9,63]

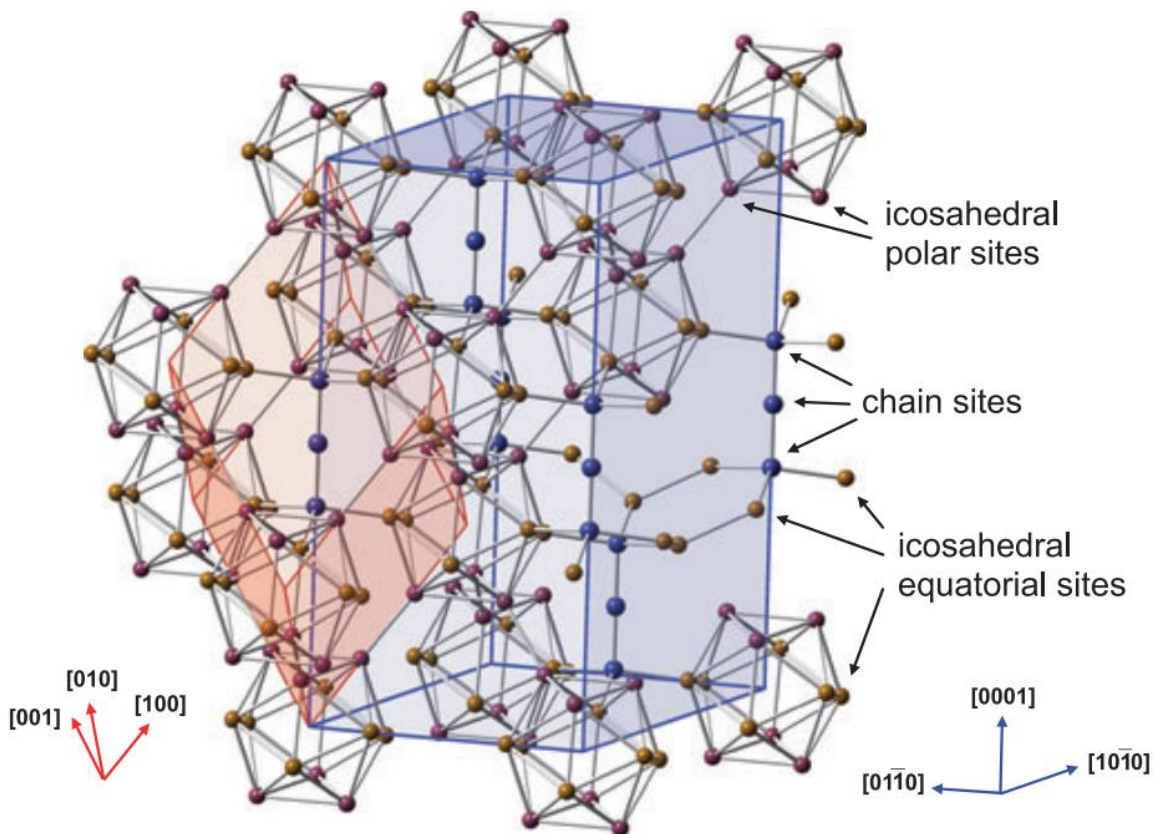


**Figure 1.5** Hexagonal (blue) and rhombohedral (red) unit cell of boron carbide. Copyright by John Wiley and Sons [62]

The origin of the compositional dependence of the electrical properties has been explained within the framework of the different models used to describe the conduction mechanisms: (bi)polaron hopping between

B<sub>11</sub>C icosahedra [14,64,65] and variable range hopping in combination with band conduction. [15] A more detailed discussion can be found in Chapter 4.

The thermoelectric properties of boron carbide have been reported for materials prepared by several different synthesis methods. This includes arc melting [66], hot-pressing and spark plasma sintering [9], thin film growth [67] and single crystal growth [63]. There is little information available on the doping of boron carbide as described by H. Werheit [15]. There are however several reports of compositing of boron carbide with secondary phases with metallic character in an effort to improve the thermoelectric properties, e.g. TiB<sub>2</sub> [68–70], Si/SiB<sub>n</sub> (n = 4, 6, 14) [71,72], TiC [73], W<sub>2</sub>B<sub>5</sub> [74], SiC [75] and HfB<sub>2</sub> [42].

Good thermoelectric performance has been reported for B<sub>4</sub>C-TiB<sub>2</sub> composites prepared by arc melting through the simultaneous reduction in electrical resistivity and thermal conductivity while increasing the Seebeck coefficient  $ZT = 0.55$  at 1100 K reported for a sample with 6 at.% TiB<sub>2</sub>. [68] Similarly, a figure of merit  $ZT = 0.4$  [71] and  $ZT = 0.29$  [72] at 1100 K was reported for B<sub>4</sub>C-SiB<sub>n</sub>-Si (n= 4, 6 and 14) composite materials prepared by arc melting through an increase of the Seebeck coefficient and a reduction in the thermal conductivity and electrical resistivity. Boron carbide + HfB<sub>2</sub> composites showed only small changes with the addition of up to 20 wt.% HfB<sub>2</sub>. Small reductions in the electrical resistivity, Seebeck coefficient and thermal conductivity with HfB<sub>2</sub> addition were observed resulting in a  $ZT \approx 0.2$  at 1000 K for both composites and the reference B<sub>13</sub>C<sub>2</sub> samples.

### 1.2.2 Full Heusler Fe<sub>2</sub>VAI

Full Heusler alloys have been first described by Friedrich Heusler in 1903. [76] The compounds follow the general formula X<sub>2</sub>YZ with X and Y being transition metals and Z being a III – V main group element. [77]

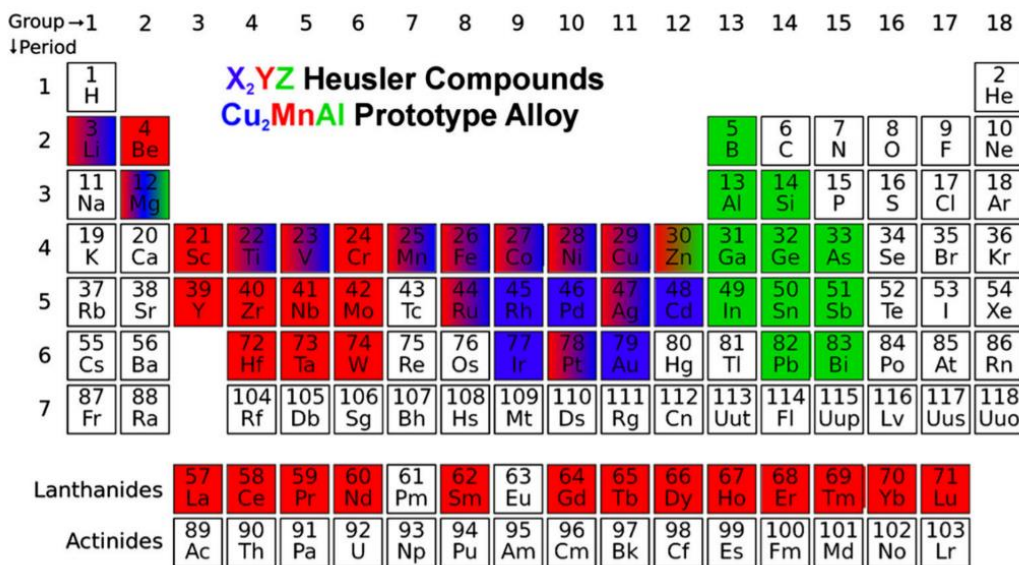


Figure 1.6 Elements forming X<sub>2</sub>YZ Heusler alloys

(Available under CC-BY-SA license: <http://creativecommons.org/licenses/by-sa/3.0/deed.en>)[77]

The crystal structure of Heusler alloys was described for the first time for  $\text{Cu}_2\text{MnAl}$ . [78] It is a fully ordered variant of the W-type structure in which all constituent elements are randomly distributed over all crystallographic sites. In the fully ordered  $\text{Cu}_2\text{MnAl}$ -type structure there are 3 distinct crystallographic sites.

**Table 1.1** Standardized crystallographic data for  $\text{Cu}_2\text{MnAl}$  structure type. [77,78]

Atomic Site	Wyckoff symbol	x	y	z	Occupancy
Cu	8c	1/4	1/4	1/4	1
Al	4b	0	0	0	1
Mn	4a	1/2	1/2	1/2	1

Order-disorder transitions are an important feature in Heusler alloys. Reversible transitions between the fully ordered  $\text{Cu}_2\text{MnAl}$ -type (space group  $225 Fm-3m$ , Strukturbericht notation  $L2_1$ ) to the partially ordered CsCl-type (space group  $221 Pm-3m$ , Strukturbericht notation B2) and the disordered W-type (space group  $Im-3m$ , Strukturbericht notation A2) occur at  $1080^\circ\text{C}$  and  $1190^\circ\text{C}$  respectively in the Heusler alloy  $\text{Fe}_2\text{VAl}$ . [79] This order-disorder transition affects the electronic structure of the compound. The fully ordered  $L2_1$   $\text{Fe}_2\text{VAl}$  is a semimetal while the A2  $\text{Fe}_2\text{VAl}$  is a metal. The B2 and  $L2_1$  structures have similar electronic properties. [79]

The Heusler alloy  $\text{Fe}_2\text{VAl}$  has been intensively studied for the development of low temperature thermoelectric modules. Modules made of n-type  $\text{Fe}_2\text{VAl}_{0.9}\text{Si}_{0.1}$  and p-type  $\text{Fe}_2\text{V}_{0.9}\text{Ti}_{0.1}\text{Al}$  have been manufactured.[80] 36 modules (18 pairs of p- and n-legs) attached to a motorcycle exhaust pipe had an estimated maximum power output of 10 W for a temperature difference of 200 K. [80] Similarly, a module made from W-doped  $\text{Fe}_2\text{VAl}$  reached a power density of  $0.7 \text{ W cm}^{-2}$  (hot side: 673 K, cold side: 293 K). [10]

Stoichiometric  $\text{Fe}_2\text{VAl}$  is a p-type semimetal with a moderate Seebeck coefficient of  $20 - 30 \mu\text{V K}^{-1}$  at room temperature.[81–83] It has an indirect band gap of roughly 0.2 eV. [84] The electronic band structure and DOS can be seen in Figure 1.7.

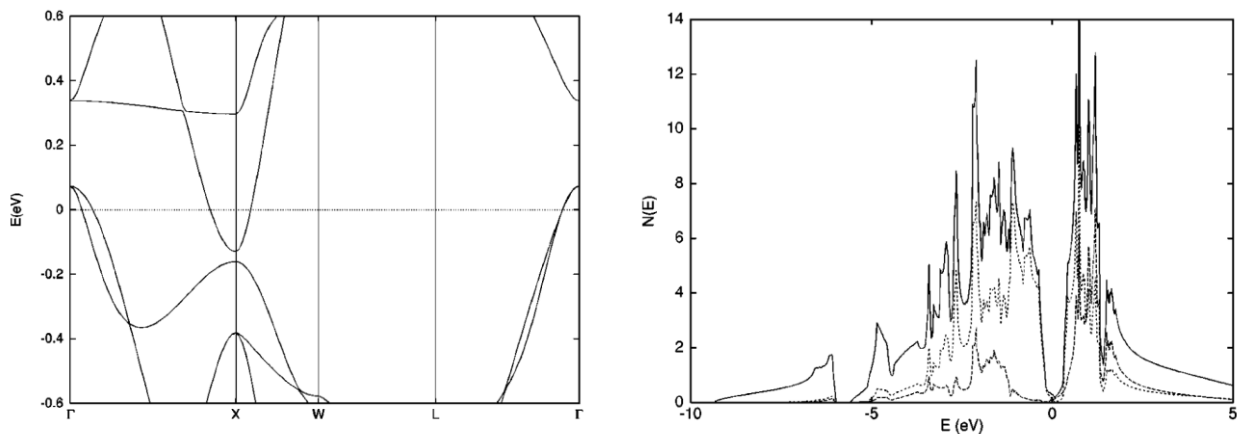


**Figure 1.7**  $\text{Fe}_2\text{VAl}$  band structure near  $E_F$  (left) and electronic density of states  $N(E)$  (right). Contributions from Fe d (dotted) and V d (dashed) electronic states. Copyright by American Physical Society [85]

The material is generally synthesized by arc-melting [82] or mechanical alloying [80].

High power factor  $pf = \alpha^2 \rho^{-1}$  have been reported close to 300 K for this material. Depending on the dopant,  $\text{Fe}_2\text{VAl}$  can be pushed in both p- and n-type direction thanks to steep features in the edges of its pseudo gap at higher and lower energies of the Fermi level.[85] Substituting elements which introduce more electrons can shift the Fermi level towards higher energies and cause n-type behavior in  $\text{Fe}_2\text{VAl}$ . Notable examples with high power factor are  $5.4 \text{ mW m}^{-1} \text{ K}^{-2}$  for  $\text{Fe}_2\text{VAl}_{0.9}\text{Si}_{0.1}$ [81],  $4 \text{ mW m}^{-1} \text{ K}^{-2}$  for  $\text{Fe}_2\text{V}_{0.9}\text{Mo}_{0.1}\text{Al}$  [86],  $4 \text{ mW m}^{-1} \text{ K}^{-2}$  for  $\text{Fe}_2\text{VAl}_{0.9}\text{Sn}_{0.1}$  [87] and  $6.5 \text{ mW m}^{-1} \text{ K}^{-2}$  for  $\text{Fe}_2\text{VAl}_{0.95}\text{Ta}_{0.05}$ [88]. Substituting elements with fewer electrons shifts the Fermi level to lower energies resulting in p-type conduction, examples are  $\text{Fe}_2\text{V}_{0.9}\text{Ti}_{0.1}\text{Al}$  [86] with  $pf = 2.6 \text{ mW m}^{-1} \text{ K}^{-2}$  and  $\text{Fe}_2\text{V}_{0.9}\text{Ti}_{0.05}\text{Ta}_{0.05}\text{Al}$  [89] with  $pf = 3 \text{ mW m}^{-1} \text{ K}^{-2}$ .

Off-stoichiometry is an important factor that has significant influence on the thermoelectric properties of  $\text{Fe}_2\text{VAl}$  due to the narrow band gap and low DOS at the Fermi level as shown in Figure 1.7. [85] Off-stoichiometry in the Al-content leads to a shift of the Fermi energy to higher levels in case of Al-poor and lower levels in the case of Al-rich compositions with the assumption of a rigid-band model in  $(\text{Fe}_{2/3}\text{V}_{1/3})_{100-y}\text{Al}_y$  ( $y=25.0$  is stoichiometric  $\text{Fe}_2\text{VAl}$ ,  $y<25.0$  is Al-poor,  $y>25.0$  is Al-rich) [82] and  $\text{Fe}_2\text{V}_{1-x}\text{Al}_{1+x}$  [90]. In the latter case, substitution of V with Al or Al with V can be seen as hole or electron doping respectively. This leads to a Seebeck coefficient ranging from  $90 \mu\text{V K}^{-1}$  for Al-rich to  $-140 \mu\text{V K}^{-1}$  with only small changes in the composition. Power factors of  $2.8 \text{ mW m}^{-1} \text{ K}^{-2}$  for p-type  $\text{Fe}_2\text{V}_{0.94}\text{Al}_{1.06}$  and  $5.0 \text{ mW m}^{-1} \text{ K}^{-2}$  for n-type  $\text{Fe}_2\text{V}_{1.06}\text{Al}_{0.94}$  were reported. [90]

Despite the high power factors of  $\text{Fe}_2\text{VAl}$  comparable to high-performance thermoelectric materials the figure of merit at 300 K is limited to low values of roughly 0.1. [90] This is due to the high thermal conductivity of  $\text{Fe}_2\text{VAl}$ . The reported values vary depending on the stoichiometry and microstructure, examples are  $\kappa = 20 - 25 \text{ W m}^{-1} \text{ K}^{-1}$  [83] and  $\kappa = 28 \text{ W m}^{-1} \text{ K}^{-1}$  [91].

Efforts to reduce the lattice contribution to the thermal conductivity includes doping with heavy elements which increases phonon scattering due to the mass difference to the lighter Fe, V and Al elements. Good results have been achieved for example for  $\text{Fe}_2\text{VTa}_{0.05}\text{Al}_{0.95}$  which, in combination with high-pressure torsion (HPT) nano-structuring and annealing, managed to reduce the thermal conductivity to  $5 \text{ W m}^{-1} \text{ K}^{-1}$  at 300 K and reach  $ZT = 0.3$  at 500 K.[92] Similarly, the thermal conductivity of  $\text{Fe}_2\text{V}_{0.9}\text{W}_{0.1}\text{Al}$  could be reduced to  $5 \text{ W m}^{-1} \text{ K}^{-1}$  at 300 K and the  $ZT = 0.2$  at 400 K was reported. The reduction was due to the substitution of V with heavier and larger W atoms and the submicron grainsize due to the synthesis by mechanical alloying and densification by pulse-current sintering. [93] The stoichiometric  $\text{Fe}_2\text{VAl}$  sample in this sample had a thermal conductivity  $\kappa = 16 \text{ W m}^{-1} \text{ K}^{-1}$  showing the influence of the sample preparation method.

### 1.3 Experimental Techniques

In this section the main experimental techniques for the preparation of the materials as well as the measurement of their physical properties which were used in the course of this thesis will be described. Additional details regarding the experimental procedures are provided in the respective chapters.

#### 1.3.1 Sample Preparation

##### 1.3.1.1 Optical Floating Zone

Floating zone crystal growth is a well-established technique for the preparation of single crystals of varying materials with diameters of  $> 1$  cm and lengths of several cm. The method's experimental setup is shown schematically in Figure 1.8.

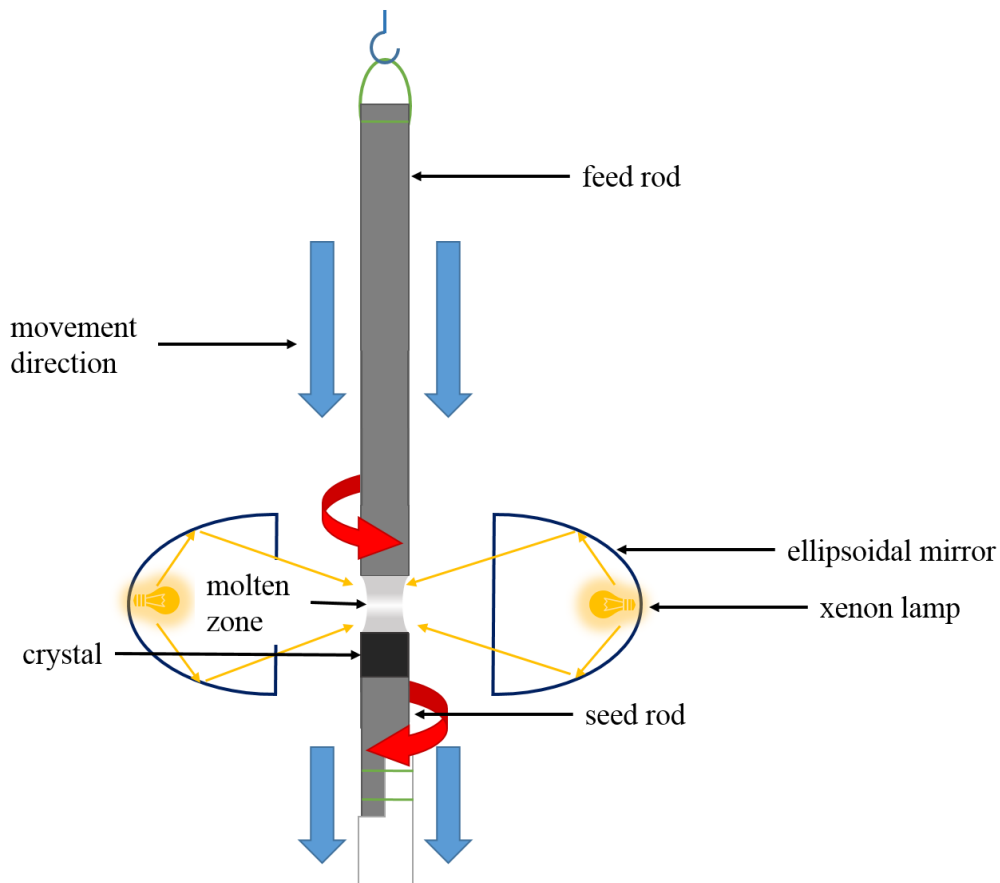


**Figure 1.8** Optical floating zone single crystal growth experimental setup.

The floating zone single crystal growth involves many parameters which have to be adjusted. The most important among these are [94]

- feed rod characteristics (shape, dimensions, composition, density, homogeneity)
- crystallization rate
- growth atmosphere and gas pressure
- temperature gradient and molten zone temperature
- rotation rate

The technique requires 2 rods which typically consist of the material of the crystal being grown. The feed rod is suspended from the top while the seed rod is positioned at the bottom fixed to a (alumina) sample holder.

The preparation of a feed rod of high quality is one of the most crucial steps for the success of the crystal growth process. The feed rod needs to be dense (relative density  $\geq 60\%$ ), straight and of homogeneous diameter, density and composition. [94] Experimental preparation of such feed rods can be carried out by inserting the powder mixture into a rubber tube sealed on one end. The powder is packed densely and residual air is removed with a vacuum pump. The evacuated tube is then sealed on the other end and the powder is densified in a CIP at pressures of several hundred MPa. The compacted rod is then sintered in a furnace. Multiple sintering steps can be employed for higher density of the feed rod.[95,96] There exist advanced procedures which have been employed for example for the growth of monochromator-grade crystals of  $YB_{66}$  by Tanaka et al., namely the “zone pass technique” and the “multi-zone pass technique”. [97,98] For the “zone pass technique” the sintered feed rod is passed at a high rate [ up to  $400\text{-}500 \text{ mm hr}^{-1}$ ] through the hot zone which causes partial melting and increased densification. Similarly, the “multi-zone pass technique” uses the crystal grown in the first optical floating zone crystal growth procedure as a highly dense and homogeneous feed rod for a subsequent growth step.

Both feed and seed rod are being held in place by wires of metals made from high melting metals, e.g. tungsten. Both rods are brought into close proximity and rotated around a central axis in opposing directions. The area in between the ends of both rods is then heated, the heat source depends on the material of the crystal being grown. For the growth of crystals of electrically conductive materials, HF induction heating coils can be used. For the growth of crystals of materials with low electrical conductivity, the optical floating zone technique has been developed. The optical floating zone single crystal growth uses e.g. Xe lamps whose light is focused by large ellipsoidal mirrors reaching temperatures exceeding  $2000^{\circ}\text{C}$ . [99] The melted zone between feed and seed rod is stabilized by the surface tension of the liquid. The feed and seed rods are being lowered slowly through the heated area. In this process, the feed rod is consumed and the crystal grows on top of the seed rod. Both polycrystalline and single crystalline seed rods may be used. Using a polycrystalline seed rod requires the growth of a crystal of several centimeters. In the growth process using a polycrystalline seed rod, many smaller grains crystallize simultaneously.[99] With the ongoing crystal growth, fewer and fewer grains remain until ultimately only a single crystal remains. This is shown schematically in Figure 1.9. The atmosphere depends

on the material. Generally crystal growth can be carried out under Ar flow. Materials with high vapor pressure may also require growth under overpressure.

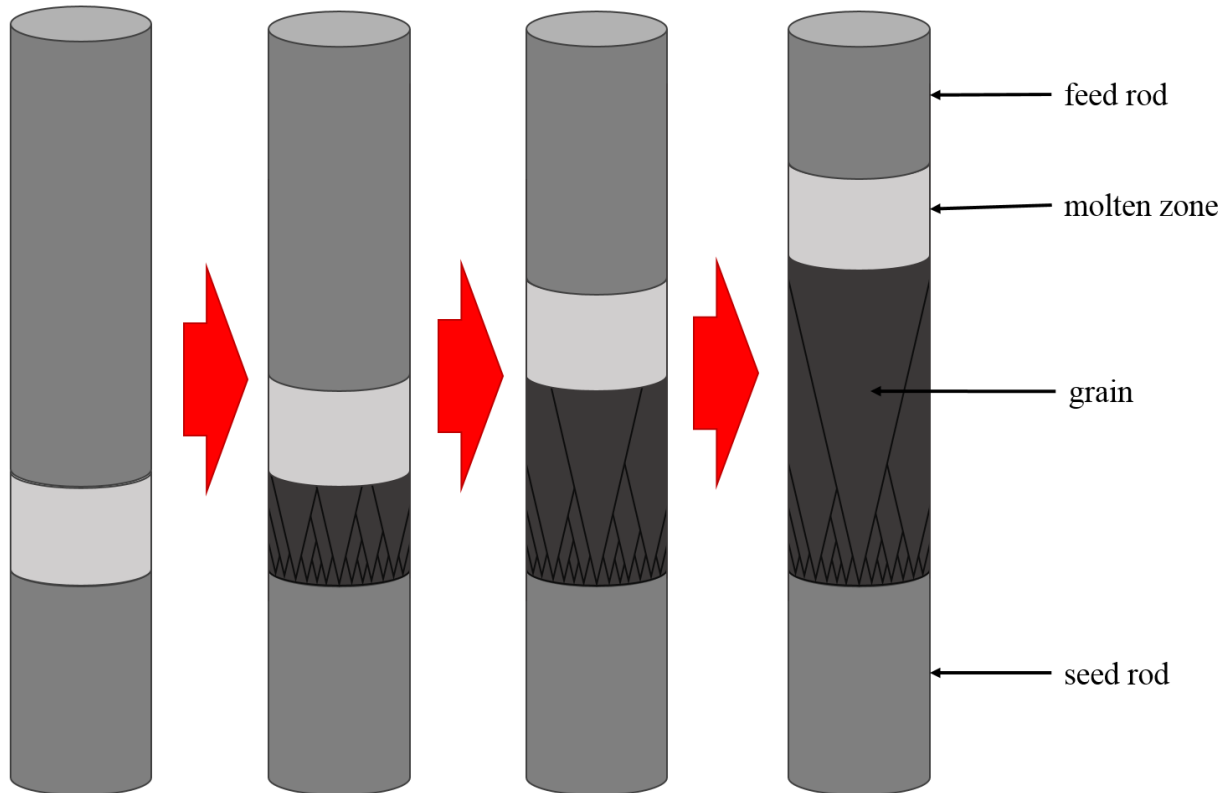


**Figure 1.9** Floating zone single crystal growth from polycrystalline seed rod (schematic).  
(After [99] and [100])

### 1.3.1.2 Spark Plasma Sintering

Spark plasma sintering is a technology which allows the consolidation of powders into dense pellets through the application of pressure and heating within a short time. It is therefore commonly used in thermoelectric research for the preparation of samples as the fast sintering can help retaining nanostructuring and metastable modifications of the materials being processed. The experimental setup is shown schematically in Figure 1.10.

The setup consists of two electrodes at the top and bottom through which uniaxial hydraulic pressure is applied. A series of graphite spacers with decreasing diameter is placed above and below the die for more even distribution of the applied pressure. Two punches are inserted into the die from top and bottom, the sample powder is located between the punches. The heating is facilitated through the application of a pulsed DC current. The pathway of the electrical current depends strongly on the electrical resistivity of the sample powder. In thermoelectric materials, which are usually semiconductors, the current passes mainly through the graphite die which then heats the sample powder externally through resistive Joule heating. Additionally, the current may pass through the sample powder leading to localized heating between the powder particles through electric discharge.[101] Spark plasma sintering provides high heating rates ( $>100^{\circ}\text{C min}^{-1}$ ) and temperatures

(>2000°C) making it possible to reach full densification with holding times of 5 – 30 min. The shorter sintering times limit grain growth during the sintering process. [101]

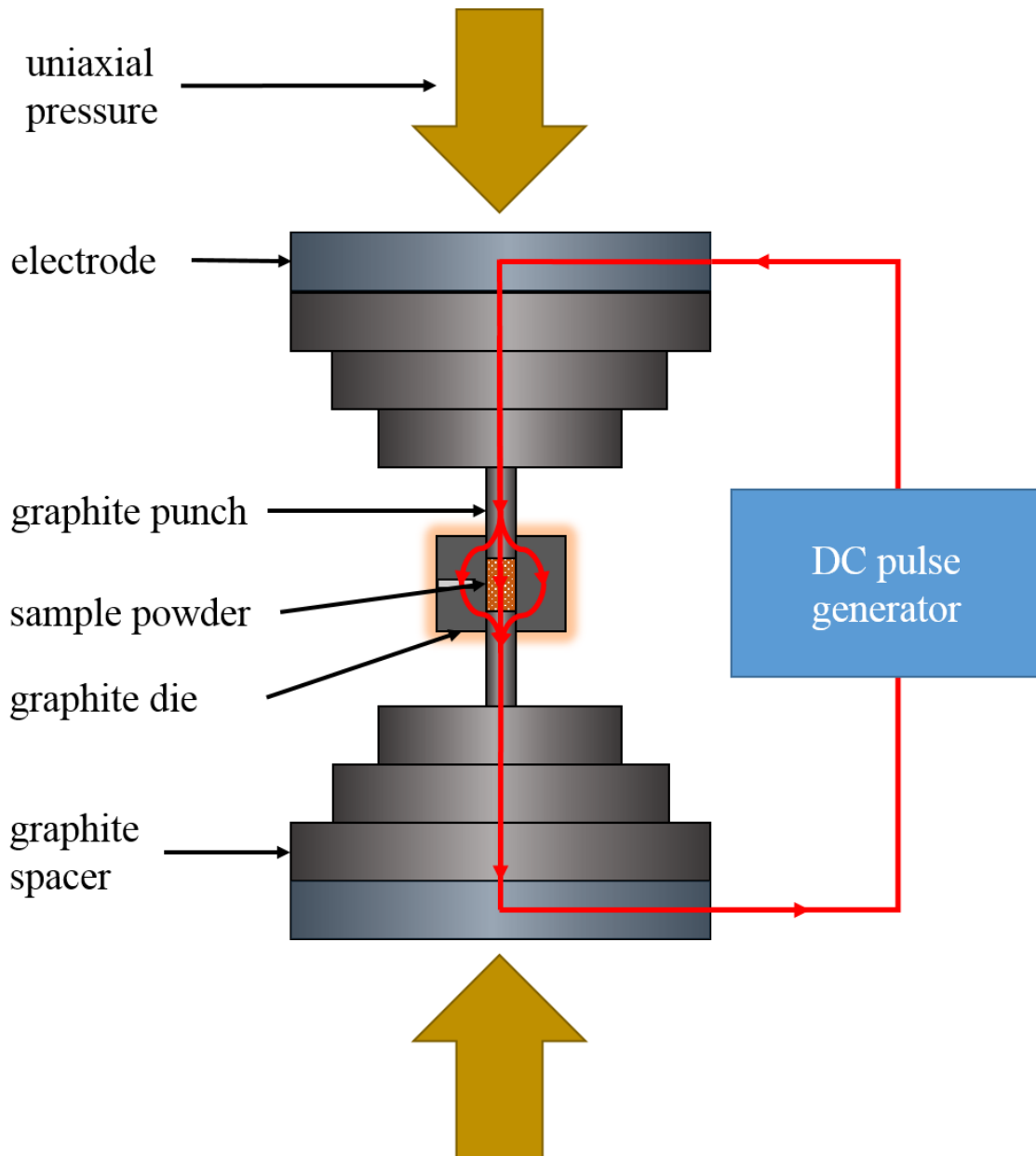


**Figure 1.10** Spark plasma sintering system (schematic).

The main adjustable parameters for the optimization of the sintering process include the sintering temperature, applied pressure and particle size. [102] An increase in applied pressure and reduction in particle size both lead to a significant reduction in the required sintering temperature, the temperature difference being in the range of several hundred °C. [102] The heating rate on the other hand appears to have little influence the final sample density. [102] The sintering can be carried out in different atmospheric conditions, including inert gas atmosphere (e.g. Ar, N<sub>2</sub>) or (dynamic) vacuum which can influence the sintering behavior and need to be selected depending on the sample material.

In this work, one-step sintering schedules were used, details can be found in the experimental sections of the respective chapters.

### 1.3.2 Physical Properties Measurements

This section contains descriptions of the measurement principles and setups of the main methods for the determination of the physical properties used in this work. Comparing measurement results requires the knowledge of the measurement uncertainties for accurate interpretation. A round-robin study involving several laboratories performing measurements of the thermoelectric properties on standard samples found that the standard uncertainties of the determination of the thermoelectric properties (68% confidence level) is estimated to be in the order of 6%, 8%, 11% and 19% for the Seebeck coefficient, electrical resistivity, thermal conductivity and figure of merit respectively.[103]

#### 1.3.2.1 Seebeck Coefficient and Electrical Resistivity Measurement

The measurement of the electrical properties (electrical resistivity and Seebeck coefficient) of thermoelectric materials at temperatures exceeding 300 K is frequently carried out with instruments such as the ULVAC-Riko ZEM-2. The measurement setup is shown schematically in Figure 1.11.

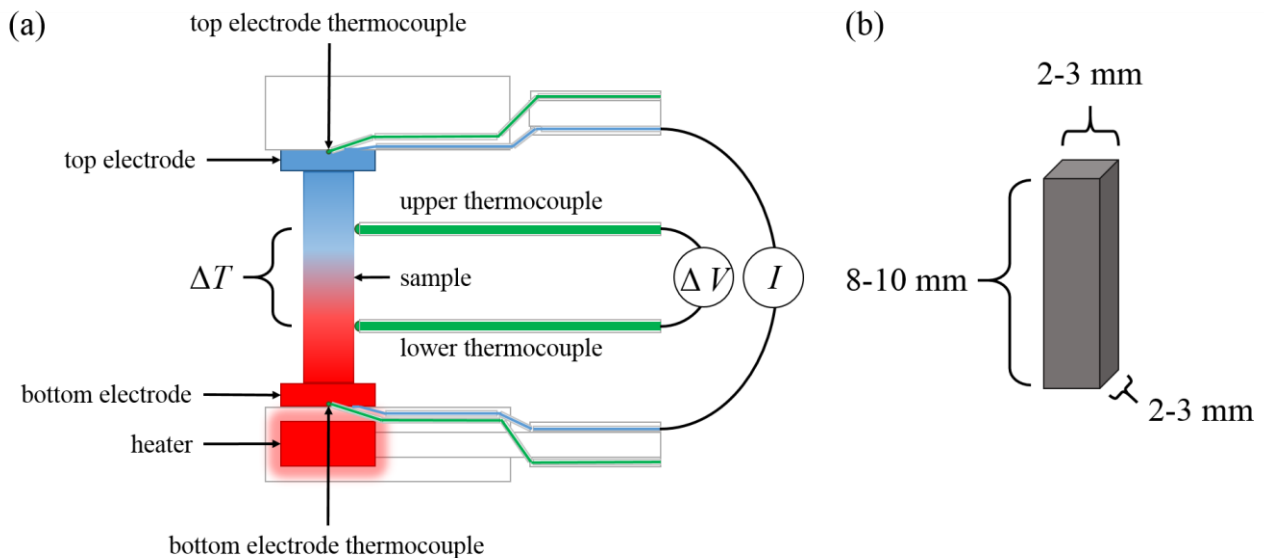


**Figure 1.11** Seebeck coefficient and electrical resistivity (a) measurement setup (schematic) (b) sample shape and dimensions.

The measurement of Seebeck coefficient and electrical resistivity is carried out in the 4-probe/4-point geometry as shown in Figure 1.11. Alternatively, 2-point and uniaxial 4-point geometries can be used, each with advantages and disadvantages. [104]

In the 4-point geometry a bar shaped sample of generally 8-10 x 2-3 x 2-3 mm<sup>3</sup> (Figure 1.11 (b)) is placed in between 2 electrodes. Small sheets of graphite paper are placed in between the top and bottom ends of the sample bar and the electrodes for better electrical and thermal contacts as well as to prevent interaction between

sample and electrodes at elevated temperatures. Two thermocouples (K-type thermocouples in case of the ZEM-2 instrument) are brought into contact with the sample bar. To ensure good electrical contact between the sample and the thermocouples, I-V (current-voltage) curves are measured by varying the applied electrical current  $I$  and measuring the voltage  $\Delta V$  between the thermocouples. For low contact resistance the slope of the I-V curve, i.e. the resistance, should be independent of the applied current in the measurement range.

The temperature is controlled by several thermocouples in the instrument. The system's temperature is changed through resistive heaters surrounding the whole setup shown in Figure 1.11. The thermocouple measuring the system temperature is placed on the outside of the metal heat shield in between the heating coils and the sample setup. Two thermocouples (top and bottom electrode thermocouples) measure the temperature difference which is set by the user. The actual temperature difference between upper and lower thermocouple depends strongly on the sample properties. This temperature difference between top and bottom electrodes is created by a heater situated below the bottom electrode.

The measurements are typically performed in inert gas (e.g. He) atmosphere.

The Seebeck coefficient  $\alpha$ , which is given by

$$\alpha = \frac{\Delta V}{\Delta T} \quad (1.9)$$

is measured by the so-called slope method. [104] Several different values for the temperature difference  $\Delta T$  between top and bottom thermocouple in the range of 1 – 10 K are being applied at a constant overall temperature  $T$  and the voltage  $\Delta V$  is measured. The Seebeck coefficient  $\alpha$  can then be determined from the slope of the  $\Delta V$ - $\Delta T$  plot. [104] Measurements of  $\Delta V$  for 3-5 different  $\Delta T$  values are required for reliable results.

The electrical resistivity  $\rho$  is determined in the same measurement setup (Figure 1.11) from

$$\rho = R \frac{A}{l} = \frac{\Delta V}{I} \frac{A}{l} \quad (1.10)$$

with  $R$ ,  $\Delta V$ ,  $I$ ,  $A$  and  $l$  being the electrical resistance, the measured voltage, the applied electrical current, the sample cross-sectional area and the distance between the electrical contacts. The relatively larger error in the measurement of the electrical resistivity compared to the Seebeck coefficient as mentioned in Section 1.3.3 is largely due to errors in the determination of the geometrical factor  $A/l$ . [104] The distance between the electrical contacts is in the range of 3 – 5.6 mm.

### 1.3.2.2 Thermal Conductivity Measurement

The thermal conductivity  $\kappa$  is given by

$$\kappa = D_t C_p \rho_m \quad (1.11)$$

with  $D_t$ ,  $C_p$  and  $\rho_m$  being the thermal diffusivity, specific heat and sample density respectively.

The thermal diffusivity  $D_t$  can be determined by the laser flash method. The experimental setup is shown schematically in Figure 1.12.

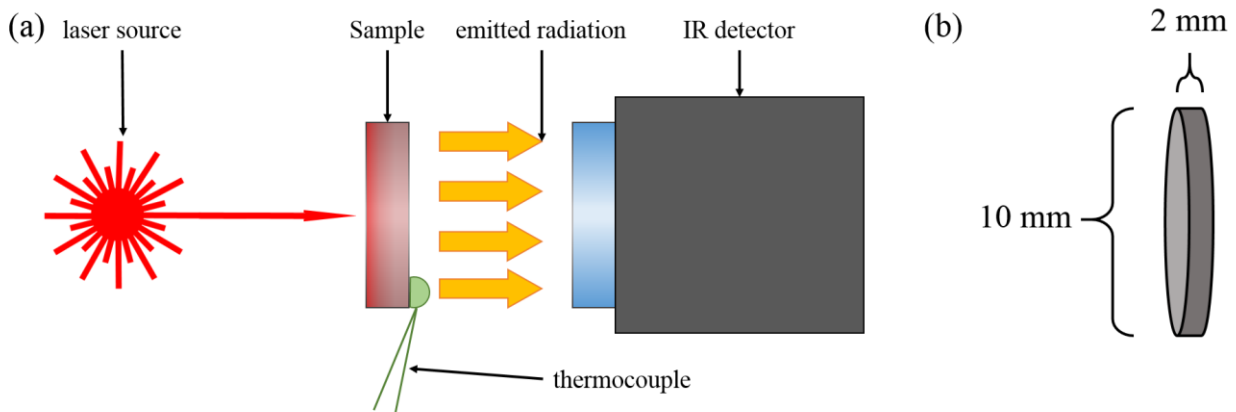


**Figure 1.12** Laser flash analysis (a) measurement setup (schematic) (b) sample shape and dimensions.

The laser flash analysis measurement involves a short laser pulse, which hits the front surface of the sample. The temperature change on the back side of the sample induced by the heat energy transferred from the laser pulse is measured through the emitted radiation which is detected by an IR detector cooled by liquid nitrogen. The temperature eventually reaches a maximum value. The thermal diffusivity can be evaluated from the time between the laser pulse and the time  $T_{1/2}$  to reach 1/2 of the maximum temperature according to

$$D_t = 1.38 \frac{d^2}{\pi T_{1/2}} \quad (1.12)$$

with  $d$  being the sample thickness. [105] Corrections for heat loss are employed in modern LFA instruments to achieve more accurate results. [104] Cylindrical samples with a diameter  $\phi = 10$  mm and a thickness of approximately  $d = 2$  mm were used for LFA measurements in this work.

The specific heat of a material can be determined by LFA using a comparative measurement of the sample and a reference material whose specific heat is known. The temperature change  $\Delta T$  induced by the laser pulse is measured for both the sample and the reference material and the sample's specific heat can be calculated from

$$C_p^{sample} = \frac{\Delta T^{reference}}{\Delta T^{sample}} \frac{\rho_m^{reference}}{\rho_m^{sample}} \frac{d^{reference}}{d^{sample}} C_p^{reference} \quad (1.13)$$

with  $C_p$ ,  $\Delta T$ ,  $\rho_m$  and  $d$  being the specific heat, temperature change, density and thickness of sample and reference material respectively.[106]

Alternatively, relative specific heat values can be determined by LFA according to

$$C_{p,T_2} = C_{p,T_1} \frac{\theta_m^{T_2}}{\theta_m^{T_1}} \quad (1.14)$$

with  $\theta_m$  derived from the intercept of the tangent of the temperature decrease plotted against the time following the maximum in temperature after a laser pulse at the temperatures  $T_1$  and  $T_2$  respectively. [107] The temperature change is measured by attaching a thermocouple to the back of the sample as shown in Figure 1.12.[108] The absolute specific heat of the sample has to be known at least one temperature for the extrapolation using this method.

DSC measurements are used to determine the specific heat values with higher accuracy. [104] The measurement requires a setup with two identical crucibles, i.e. a sample and a reference (e.g. empty crucible). The crucibles are subjected to a temperature program and the temperature difference between the crucibles is compensated by supplying heat energy. Three measurements are required in total, (1) empty crucible (sample position) against empty crucible (reference position) to determine the baseline, (2) standard material (sample position) against empty crucible (reference position) and (3) sample (sample position) against empty crucible (reference position). The specific heat of the standard material, e.g. sapphire, has to be known. The specific heat of the sample can then be calculated from

$$C_p^{sample} = C_p^{standard} \frac{m^{standard}}{m^{sample}} \frac{y^{sample}}{y^{standard}} \quad (1.15)$$

with  $C_p$ ,  $m$  and  $y$  being the specific heat, the mass and the baseline deviation of the sample and standard material respectively. [109]

Finally, the density of samples without open porosity can be determined using the Archimedes method based on buoyant force acting on a body submerged in a fluid. [110] After weighing the sample in air and submerged in a fluid (e.g. distilled water), the density can be calculated from

$$\rho_m^{sample} = \frac{m_{air}}{m_{air} - m_{fluid}} \rho_m^{fluid}(T) \quad (1.16)$$

with  $\rho_m^{sample}$ ,  $m_{air}$ ,  $m_{fluid}$  and  $\rho_m^{fluid}(T)$  being the sample density, measured sample mass in air, measured sample mass submerged in fluid and the fluid density at the measured temperature  $T$ . Samples with open pores require alternative methods to determine the density (e.g. calculation from sample mass and dimensions) because fluid entering the pores leads to an underestimation of the sample's porosity and overestimation of the density.

### 1.3.2.3 Magnetic Properties Measurement

The measurement of the magnetization  $M$  / magnetic moment  $\mu$  of a sample can be performed using an MPMS instrument consisting of a superconducting magnet (able to produce magnetic fields of several Tesla), a superconducting detection coil and a SQUID (Superconducting Quantum Inference Device) magnetometer surrounded by superconducting magnetic shielding.[111] When the sample is moved through superconducting detection coils it induces an electrical current in them. [111] The detection coils are connected to the SQUID magnetometer, which incorporates so called Josephson junctions [112] which act as a current-to-voltage convertor. This voltage is scanned as a function of the sample position and the signal is fitted to determine the magnetic moment of the sample.

The MPMS instrument includes superconducting components and therefore cooling with liquid He is required allowing measurements in the range of 2 – 400 K. Samples (pieces of regular shape or powders with masses in the range typically 10-50 mg) are mounted in gelatin capsules placed inside of plastic straws which have relatively low diamagnetic susceptibility and therefore a low background signal.

The sequence for the measurement of the temperature dependence of the magnetization  $M(T)$  consists of a zero-field cooled step (ZFC) in which the sample is cooled down to the lowest measurement temperature without any applied magnetic field. A constant magnetic field is applied and the magnetization is measured while heating. This is followed by a field-cooling step (FC). The magnetization is measured while cooling with an applied magnetic field. The magnetic-field dependence of the magnetization  $M(H)$  is measured at constant temperature while varying the applied magnetic field.

## **Chapter 2: Physical Properties (RE = Yb) and Crystal Structure (RE = Sm, Yb) of Higher Boride REB<sub>66</sub> Single Crystals**

### **2.1 Introduction**

This chapter deals with the investigation of single crystals of the higher boride REB<sub>66</sub> compound grown by the optical floating zone method. More specifically, it deals with the physical properties (thermoelectric, magnetic and mechanical) of YbB<sub>66</sub> and also with the refinement of the crystal structure of YbB<sub>66</sub> and SmB<sub>66</sub>.

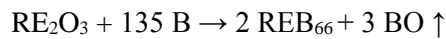
Throughout the years several higher boride materials have been investigated for the purpose as high temperature thermoelectric materials. [4,5] Among these materials  $\beta$ -boron [113–115], REB<sub>22</sub>C<sub>2</sub>N [116–118], REB<sub>44</sub>Si<sub>2</sub> [43,119], YAIB<sub>14</sub> [30,120], B<sub>6</sub>O [41,121], MB<sub>6</sub> [122,123], REB<sub>66</sub> [7,8,37,54,56] and especially boron carbide [9,15,62,64] have been investigated in detail.

Recently, good thermoelectric properties have been reported for REB<sub>66</sub> materials, more specifically SmB<sub>66</sub> [7] and YB<sub>48</sub> [8], with  $ZT$  values around 0.1 close to 1000 K. It was suggested that both the nature of the rare earth element as well as the composition could be the origin of the improved performance compared to previous reports of REB<sub>66</sub>. [37,54,56] In the case of SmB<sub>66</sub> the effective magnetic moment derived from the measurement of the temperature dependent magnetic susceptibility suggested a mixed valence state of Sm as Sm(+2)/Sm(+3). On the other hand, the higher metal content of YB<sub>48</sub> seemed to positively affect the electrical properties of the material.

YbB<sub>66</sub> was chosen as the compound to investigate the possible influence of mixed valence on the thermoelectric performance of REB<sub>66</sub> since mixed valence had been reported for YbB<sub>12</sub> before. [12,124] For this purpose, a high quality single crystal of YbB<sub>66</sub> synthesized using the optical floating zone single crystal growth was investigated. The magnetic susceptibility was measured to determine the valence state of Yb in YbB<sub>66</sub>. The material was also characterized in terms of its composition (ICP-AES), mechanical properties (hardness) and crystal structure (single crystal XRD structure refinement). Finally, the thermoelectric properties of YbB<sub>66</sub> were measured in the temperature range of 373 – 973 K. Additionally the crystal structure of SmB<sub>66</sub> was investigated through single crystal structure refinement to determine possible differences between REB<sub>66</sub> crystals with different rare earth elements.

## 2.2 Experimental

For the preparation of the SmB<sub>66</sub> single crystals by optical floating zone single crystal growth stoichiometric amounts of amorphous boron powder (New Metals and Chemicals Corporation, Ltd.; 99%) and the Sm<sub>2</sub>O<sub>3</sub> (Wako Chem.; 99.9%), are mixed in an agate mortar under ethanol for at least 30 minutes. To remove the ethanol, the mixtures are placed under a halogen lamp overnight. The dried powder mixtures are filled into a rubber tube (diameter  $\phi \sim 10$  mm) and compacted into rods in a CIP at a pressure approximately 250 MPa. The rods are placed in a BN crucible surrounded by a graphite susceptor and heated in a high-frequency induction furnace for the borothermal reduction to form REB<sub>66</sub>. The general reaction is



The sintering of the feed and seed rods is performed in two steps to achieve higher density of the rods. In the first step the rod is sintered for 10 h at 1600°C to avoid the formation of large grains at higher temperatures. The rod is then crushed in an agate mortar and compacted into a rod again as mentioned before. The second sintering step is carried out at higher temperatures of 1700°C. The single crystal growth is then performed with feed and seed rods in an optical floating zone furnace as seen in Fig. 2.1. The feed and seed rod are rotated in opposing directions (feed rod: 15 rpm, seed rod: 10 rpm) while the seed rod is lowered at 8 mm hr<sup>-1</sup>. The lowering speed of the feed rod is adjusted during the growth to keep a stable molten zone.

The high quality YbB<sub>66</sub> single crystal used in this study was provided by Prof. Takao Mori and prepared as reported previously. [97]

Single crystals XRD measurements were performed on single crystals of YbB<sub>66</sub> and SmB<sub>66</sub>. Diffractometers (Bruker APEX2 CCD and Rigaku AFC11 Saturn 724+ for YbB<sub>66</sub> and SmB<sub>66</sub> respectively) were used for the measurements of the X-ray diffraction intensities. The structure refinements were performed using the JANA2006 software package.[125] XRD measurements were also performed on the surface of the YbB<sub>66</sub> crystal cleaved along its growth axis.

The density of the samples was measured using Archimedes' method. The chemical composition of YbB<sub>66</sub> was measured using ICP-AES. For this purpose, the material was dissolved in a mixture of HCl and HNO<sub>3</sub> under heating.

The electrical properties (Seebeck coefficient, electrical resistivity) of YbB<sub>66</sub> were measured using an ULVAC-Riko ZEM-2 instrument. The measurements were performed in a 4-probe measurement setup under He atmosphere in a temperature range of 373 – 973 K. The thermal properties (thermal diffusivity, relative specific heat) of YbB<sub>66</sub> were determined by the laser flash method utilizing the ULVAC-Riko TC-7000 apparatus from RT – 973 K. The specific heat of YbB<sub>66</sub> was measured using a PPMS instrument by Quantum Design in the temperature range of 2 – 300 K under high vacuum. The specific heat determined by DSC was extrapolated to 973 K using the relative specific heat measured by LFA.

Magnetic susceptibility measurements of  $\text{YbB}_{66}$  were performed using a MPMS instrument by Quantum Design in the temperature range of 2 – 300 K with an applied magnetic field of 1000 Oe.

Vickers hardness tests of  $\text{YbB}_{66}$  were performed using a Mitutoyo Hardness Testing Machine HM-200.

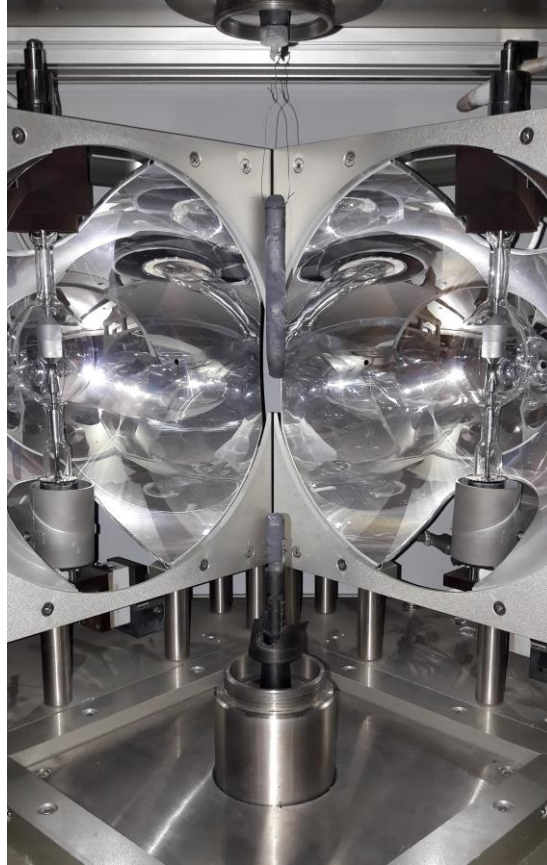


**Figure 2.1** Optical floating zone single crystal growth setup (here  $\text{SmB}_{66}$ ). The seed rod is placed at the bottom in an alumina sample holder. The feed rod is suspended from the top by tungsten wires. The light of four xenon lamps is focused in the center by mirrors.

## 2.3 Results and Discussion

### 2.3.1 Density, Chemical Composition and Surface XRD

The chemical analysis by ICP-AES of  $\text{YbB}_{66}$  crystal resulted in a Yb to B ratio of 1:58.7. This is a higher metal content than the nominal composition of  $\text{YB}_{62}$  which was used for the preparation of the feed rod for the single crystal growth. It has been reported before that  $\text{REB}_{66}$  can exist in a fairly wide range of compositions, most prominently in the case of  $\text{YB}_{66}$  which was reported to exist from roughly  $\text{YB}_{66}$  to  $\text{YB}_{48}$ . [8,47,48,56] As will be discussed later, the single crystal structure refinement of  $\text{YbB}_{66}$  gave a Yb to B ratio of 1:58.4, which is very close to the value determined by the ICP-AES chemical analysis. A previous publication on the boron-rich phases [126] found a Yb to B ratio of 1:56.7 for  $\text{YbB}_{66}$ . In this work this composition was determined by single crystal structure refinement on a crystal isolated from a sample of the initial composition  $\text{YbB}_{70}$  which

was annealed at 1825°C. It appears that YbB<sub>66</sub> generally exists at Yb-rich compositions than the nominal YbB<sub>66</sub>.

The theoretical density  $\rho_{m,XRD}$  of YbB<sub>66</sub> was calculated from the chemical composition and the lattice parameter determined from the single crystal XRD measurement. The formula for the calculation of the theoretical density is

$$\rho_{m,XRD} = \frac{m_B N_B + m_{RE} N_{RE}}{a^3 N_A} \quad (2.1)$$

which gives a value of  $\rho_{m,XRD} = 2.89 \text{ g cm}^{-3}$  with  $N_B = 1623.6$  and  $N_{Yb} = 27.79$ . [47] The experimentally determined density by the Archimedes' method is  $\rho_{m,exp} = 2.91 \text{ g cm}^{-3}$  and exceeds 100% rel. density slightly. This can be attributed to the complexity of the crystal structure as well as experimental uncertainty for the measurement.

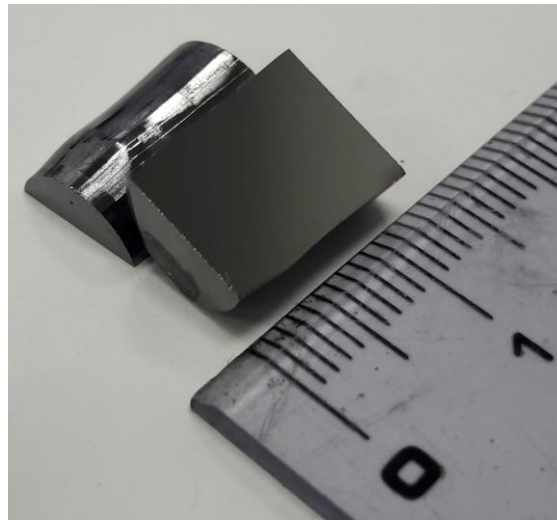


**Figure 2.2** The YbB<sub>66</sub> crystal was cleaved along its growth direction. [127]

An XRD measurement was performed on the cleaved surface of the crystal along the growth direction. The XRD pattern can be seen in Figure 2.3 and is compared to the simulated powder XRD pattern for this compound. The measured pattern shows only a small fraction of the possible reflections which is indicative of the orientation in a certain direction. Only reflections with Miller indices  $(h\ 0\ 0)$  show up in the measured diffraction pattern, so the crystal should be orientated along this axis.

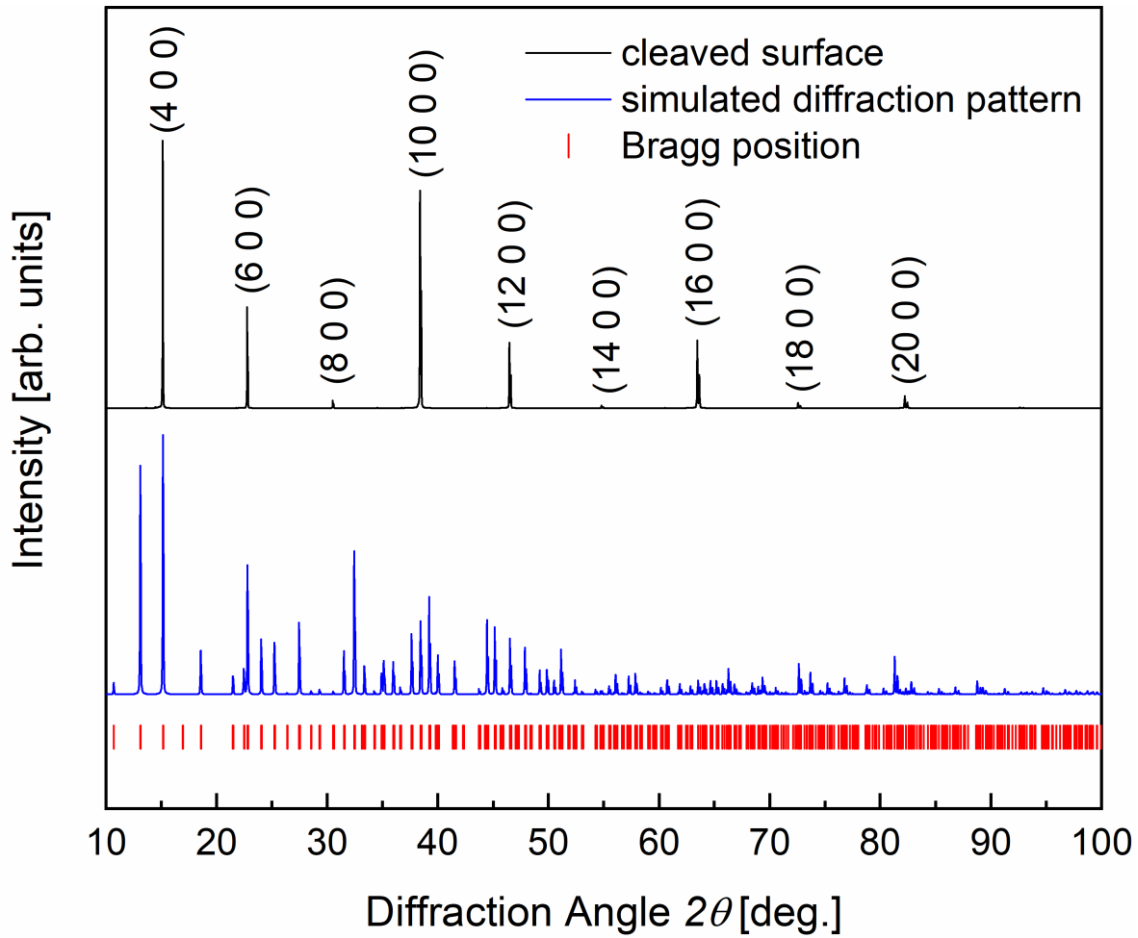


**Figure 2.3** YbB<sub>66</sub> XRD patterns for the cleaved surface and the simulated powder pattern according to the single crystal structural solution. Cu-K $\alpha_{1,2}$ -radiation was used for the measurement of the cleaved surface. The presence of exclusively (*h* 0 0) reflections suggest crystal growth orientation along the *a*-axis. [127]

Vickers hardness measurements were performed on the YbB<sub>66</sub> crystal for further characterization of the material. The results showed average values of  $1099 \pm 92$  HV ( $10.8 \pm 0.90$  GPa) which is significantly lower than previously reported values for this compound. Microhardness measurements of YbB<sub>66</sub> reported by Schwetz et al. [50] and Spear and Solovyev [128] gave hardness values of  $(2410 \pm 50 \text{ kp mm}^{-2})$  (23.6 GPa) and  $3960 \pm 200 \text{ kp mm}^{-2}$  (38.8 GPa) respectively on samples prepared by arc melting. There are several factors which can lead to this large difference, among which are grain size/grain boundary effects, influences from secondary phases ( $\beta$ -rhombohedral boron and YbB<sub>12</sub>) and differences due to the crystallographic orientation of the grains.

### 2.3.2 Single Crystal XRD

YbB<sub>66</sub> and SmB<sub>66</sub> belong to the YB<sub>66</sub> structure-type, which was originally described by Richards and Kaspar in 1969 [46] for the first time. In the original structure model there is a single atomic site 48f RE (*x*, 1/4, 1/4) for the rare earth atom and a total of 13 boron positions, B1 – B13. The B<sub>12</sub> icosahedra are built from the boron

atoms in the positions B1-B9 which are fully occupied and form  $B_{12}(B_{12})_{12}$  super-icosahedra. These super-icosahedra make up the boron framework of the crystal structure. Additionally, there are so called  $B_{80}$  clusters which are formed by the boron atoms in the partially occupied sites B10 – B13. This structure model was used as a basis for the refinement of the crystal structure of  $YbB_{66}$  and the same model was then applied to  $SmB_{66}$ . Compared to Richards' and Kaspar's original model an additional site for the rare earth element RE2 was introduced in the close proximity of the original site. In a previous crystal structure refinement on  $YbB_{66}$  such a split site was introduced by Tanaka et al. [49] with the same symmetry as the original position, i.e. Y1 in (0.0546 1/4 1/4) and Y2 in (0.0736 1/4 1/4) and the same model was later used by Sologub et al. for the single crystal structure refinement of the  $YbB_{66}$ . [126] Using this model it was however found that the atomic displacement parameters of Yb2 in the 48f position were very large compared to Yb1. Changing Yb2 to the general 192j position improved both the atomic displacement parameters for Yb2 ( $U_{22}/U_{33} = 0.0868$  for 48f and  $U_{22} = 0.0081 / U_{33} = 0.019$  for 192j respectively) as well as the overall reliability factors ( $R_{1_{obs}}=0.0742$ ,  $wR_{2_{all}}=0.2527$  to  $R_{1_{obs}}=0.0493$ ,  $wR_{2_{all}}=0.1834$  respectively). The joint-probability density function can be seen in Figure 2.4. Additional boron sites were introduced as indicated by the difference Fourier maps and supported by MEM electron densities. The “ $B_{80}$  clusters” are formed by B10-B19 in the final model and B20-B22 atoms were added in the vicinity of the  $B_{12}(B_{12})_{12}$  super-icosahedra. The final reliability factors for  $YbB_{66}$  are  $R_{1_{obs}}=4.93$  and  $wR_{2_{all}}=18.34$  (%) and residual electron densities of 1.15, -2.39  $e \text{ \AA}^{-1}$ .

This structural model was then used for the structure refinement of the  $SmB_{66}$  single crystal XRD measurement. In comparison to the previously described structure of  $YbB_{66}$ , which was found to be more metal-rich, we see that the occupancy in the 48f Sm1/Yb1 site (x,1/4,1/4) is almost identical between  $SmB_{66}$  and  $YbB_{66}$ , while the 192j Sm2 site's (x,y,z) occupancy is significantly lower than the equivalent Yb2 site.

Overall the structure refinement resulted in good reliability factors for  $SmB_{66}$  of  $R_{1_{obs}}=3.51$  and  $wR_{2_{all}}=8.65$  (%) and relatively low residual electron densities 1.17 / -0.6  $e \text{ \AA}^{-1}$ .

The structural parameters for  $YbB_{66}$  and  $SmB_{66}$  are summarized in Table 2.1.

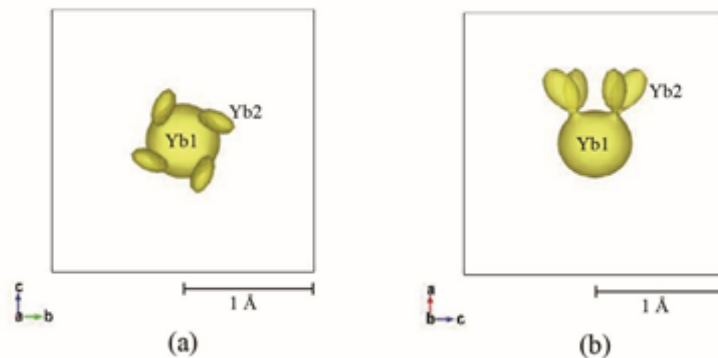


**Figure 2.4** Isosurface plot of the probability densities of Yb1 and Yb2 atoms. Isosurface level is 1 ( $\text{atom}/\text{\AA}^3$ ). [127]

**Table 2.1** Crystal data and details for data collection and refinement. [127]

<b>Crystal data</b>		
Chemical formula	Yb <sub>1.162</sub> B <sub>67.617</sub>	Sm <sub>1.029</sub> B <sub>68.232</sub>
Formula weight	932	892.3
$F(000)$	10066	9719
Crystal system	Cubic	Cubic
Space group	$Fm\bar{3}c$	$Fm\bar{3}c$
$a$ (Å)	23.4142(6)	23.4773(4)
$V$ (Å <sup>3</sup> )	12836.2(6)	12940.3(4)
$Z$	24	24
Calculated density (g/cm <sup>3</sup> )	2.894	2.7481
$\mu$ (mm <sup>-1</sup> )	5.10 (Mo $K\alpha$ )	2.832 (Mo $K\alpha$ )
Crystal size (mm)	0.1 × 0.08 × 0.023	0.188 × 0.126 × 0.023
<b>Data collection</b>		
No. of measured reflections	178926	84947
No. of independent reflections	2367	2516
$R_{\text{int}}$	0.027	0.040
$\theta_{\text{max}}$ (°)	45.3	46.3
Range of $h$	-46 → 46	-47 → 45
$k$	-46 → 46	-34 → 47
$l$	-46 → 46	-46 → 47
Absorption correction	Multi-scan	Multi-scan
$T_{\text{min}}, T_{\text{max}}$	0.608, 0.699	0.746, 0.848
<b>Refinement</b>		
No. of used reflections	2306	2516
No. of parameters	155	156
$R(F)$ [ $F^2 > 2\sigma(F^2)$ ]	0.049	0.0351
$wR(F^2)$	0.183	0.0865
$S$	4.88	2.67
Weighting scheme	$1/(\sigma^2(I) + 0.0009I^2)$	$1/(\sigma^2(I) + 0.0004I^2)$
$\Delta\rho_{\text{max}}, \Delta\rho_{\text{min}}$ (e Å <sup>-3</sup> )	1.15, -2.39	1.17, -0.6

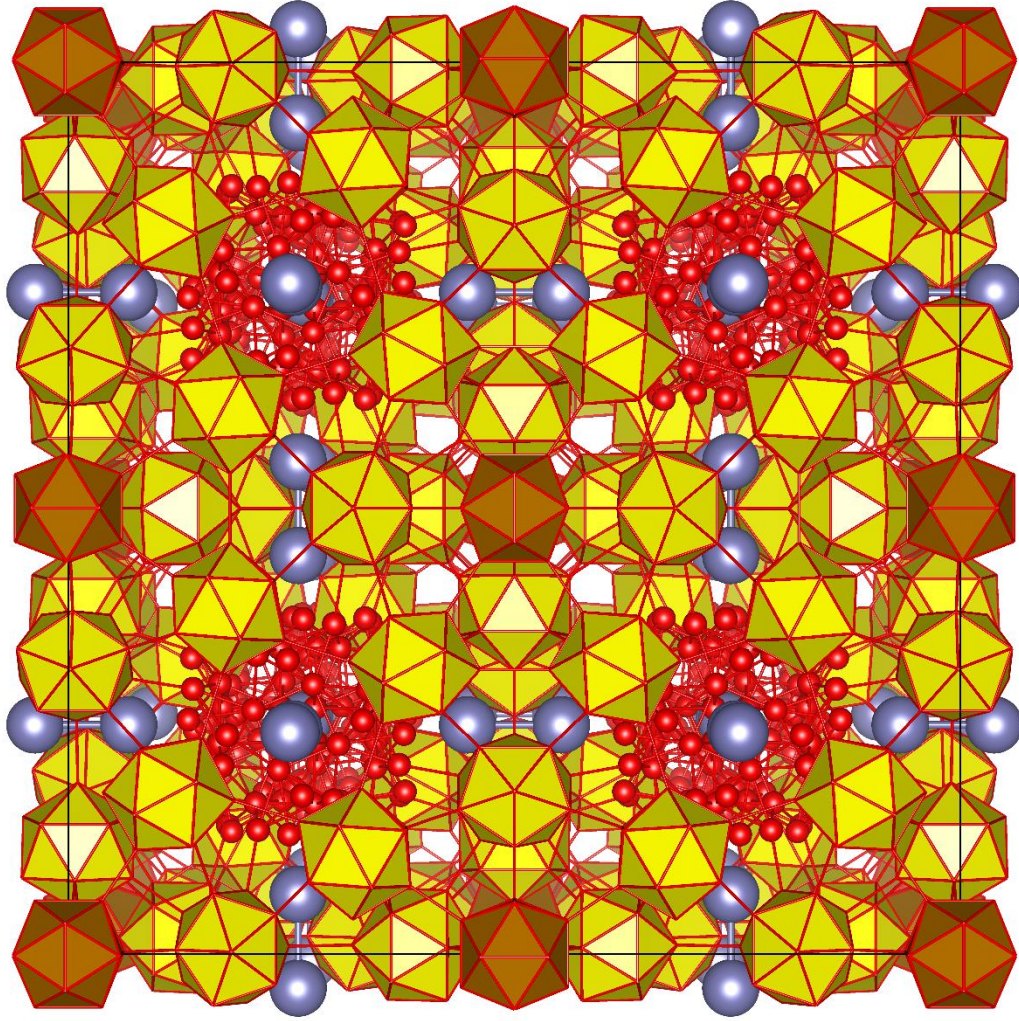


**Figure 2.5** Partial view of the unit cell of  $\text{YbB}_{66}$  and  $\text{SmB}_{66}$ . ( $0 \leq x \leq 0.5$  and  $0 \leq y \leq 0.5$ ).  $\text{B}_{12}(\text{B}_{12})_{12}$  super-icosahedra are drawn in yellow with a brown central  $\text{B}_{12}$  icosahedron. “ $\text{B}_{80}$  clusters” are formed by red boron atoms. RE-RE pairs are drawn in grey (partially occupied). The additionally introduced boron sites with low occupancy and the  $192j$   $\text{Yb}_2/\text{Sm}_2$  positions have been omitted in this figure for visual clarity. [127]

**Table 2.2** Atomic coordinates, atomic displacement parameters and occupancies of the refinement of the crystal structure of a YbB<sub>66</sub> single crystal. [127]

Atom	x	y	z	Uiso*/Ueq	Occupancy
Yb1	0.05418 (6)	0.25	0.25	0.01259 (13)	0.423 (5)
Yb2	0.0721 (2)	0.2436 (7)	0.2609 (6)	0.0164 (16)	0.0394 (11)
B1	0	0.03751 (9)	0.05950 (8)	0.0101 (4)	1
B2	0	0.07617 (8)	0.11703 (8)	0.0113 (4)	1
B3	0	0.03900 (8)	0.18103 (8)	0.0097 (4)	1
B4	0	0.14868 (8)	0.24192 (8)	0.0083 (3)	1
B5	0	0.18576 (8)	0.17182 (8)	0.0090 (4)	1
B6	0.03879 (7)	0.14001 (6)	0.12191 (6)	0.0119 (3)	1
B7	0.03954 (6)	0.08166 (6)	0.22921 (6)	0.0103 (3)	1
B8	0.06284 (6)	0.07740 (6)	0.15876 (7)	0.0113 (3)	1
B9	0.06350 (6)	0.14583 (6)	0.19493 (7)	0.0126 (3)	1
B10	0.1321 (3)	0.1671 (3)	0.2065 (4)	0.0126 (15)	0.29 (2)
B11	0.2303 (5)	0.1605 (4)	0.2986 (4)	0.0292 (19)	0.36 (3)
B12	0.1727 (2)	0.1267 (2)	0.2582 (3)	0.0107 (13)	0.258 (14)
B13	0.2303 (3)	0.2303 (3)	0.2303 (3)	0.023 (2)	0.25 (2)
B14	0.1493 (6)	0.2554 (7)	0.2301 (6)	0.015 (3)*	0.117 (11)
B15	0.1678 (9)	0.2396 (9)	0.1883 (14)	0.020 (5)*	0.14 (3)
B16	0.1606 (13)	0.3394 (13)	0.25	0.012 (10)*	0.055 (19)
B17	0.1361 (11)	0.1883 (12)	0.2598 (12)	0.016 (7)*	0.076 (16)
B18	0.1817 (5)	0.1269 (5)	0.3057 (4)	0.006 (2)*	0.21 (3)
B19	0.1415 (8)	0.1902 (7)	0.3246 (5)	0.014 (3)*	0.20 (3)
B20	0	0.0227 (13)	0.2539 (11)	0.013 (6)*	0.083 (19)
B21	0.0646 (8)	0.0646 (8)	0.0646 (8)	0.011 (8)*	0.09 (3)
B22	0.0210 (6)	0.0612 (6)	0.3030 (6)	0.015 (3)*	0.123 (11)

**Table 2.3** Atomic coordinates, atomic displacement parameters and occupancies of the refinement of the crystal structure of a SmB<sub>66</sub> single crystal.

Atom	<i>x</i>	<i>y</i>	<i>z</i>	<i>U</i> <sub>iso</sub> */ <i>U</i> <sub>eq</sub>	Occupancy
Sm1	0.05378(16)	0.25	0.25	0.0097(3)	0.414(19)
Sm2	0.0655(14)	0.2436(13)	0.2564(12)	0.012(2)	0.025(5)
B1	0	0.03722(4)	0.05913(4)	0.00787(19)	1
B2	0	0.07553(4)	0.11642(4)	0.00909(19)	1
B3	0	0.03892(4)	0.18038(4)	0.0097(2)	1
B4	0	0.14792(4)	0.24188(4)	0.0091(2)	1
B5	0	0.18525(4)	0.17093(4)	0.0092(2)	1
B6	0.03868(3)	0.13964(3)	0.12154(3)	0.01144(16)	1
B7	0.03929(3)	0.08141(3)	0.22891(3)	0.01038(15)	1
B8	0.06279(3)	0.07728(3)	0.15814(3)	0.01052(15)	1
B9	0.06323(3)	0.14524(3)	0.19438(3)	0.01269(16)	1
B10	0.1309(2)	0.1668(3)	0.2055(3)	0.0162(12)	0.287(14)
B11	0.2298(3)	0.1602(3)	0.2989(3)	0.0294(11)	0.365(18)
B12	0.17199(15)	0.12662(15)	0.25889(17)	0.0151(9)	0.258(7)
B13	0.22976(15)	0.22976(15)	0.22976(15)	0.0314(11)	0.286(9)
B14	0.1485(4)	0.2536(5)	0.2286(4)	0.018(2)*	0.095(5)
B15	0.1676(5)	0.2385(6)	0.1885(9)	0.015(3)*	0.118(18)
B16	0.1610(6)	0.3390(6)	0.25	0.026(5)*	0.099(12)
B17	0.1381(8)	0.1883(7)	0.2620(7)	0.030(4)*	0.105(10)
B18	0.1824(3)	0.1265(3)	0.3064(2)	0.0115(12)*	0.247(16)
B19	0.1415(5)	0.1896(3)	0.3260(3)	0.0182(15)*	0.229(16)
B20	0	0.0224(8)	0.2551(7)	0.012(4)*	0.064(8)
B21	0.0565(6)	0.0565(6)	0.0565(6)	0.018(5)*	0.084(14)
B22	0.0203(2)	0.0628(2)	0.3039(2)	0.0081(13)*	0.121(4)

### 2.3.3 Magnetic Properties

As mentioned previously in the introduction of this chapter, one of the main points of interest of the investigation of  $\text{YbB}_{66}$  is the determination of the possible influence of rare earth mixed valence on the thermoelectric performance of  $\text{REB}_{66}$  materials. For this purpose, the temperature dependence of the magnetic susceptibility  $\chi$  was measured in the temperature range 2 – 300 K. The valence state of Yb could then be determined from the effective magnetic moment obtained from the Curie-Weiss fitting of the high temperature part of the inverse magnetic susceptibility  $(\chi_m - \chi_0)^{-1}$ .

The measured molar magnetic susceptibility and inverse molar magnetic susceptibility are plotted against the temperature in Figure 2.6. The temperature-independent contribution  $\chi_0$  was determined from the Curie-Weiss fitting

$$\chi = \chi_0 + \frac{C}{T - \theta} \quad (2.2)$$

The temperature-independent term has been described previously in the investigation of other  $\text{REB}_{66}$  compounds [129], its origin has not been clarified yet though.

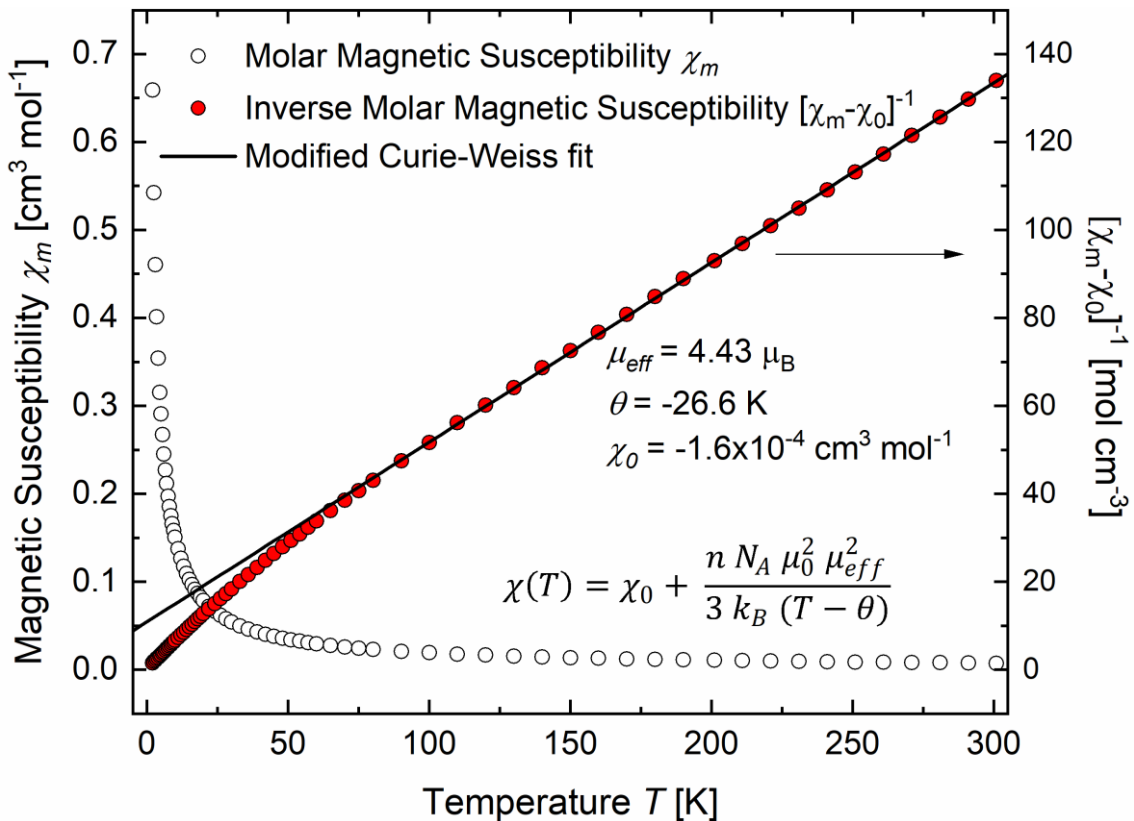


**Figure 2.6** Molar magnetic susceptibility  $\chi_m$  and inverse molar magnetic susceptibility  $(\chi_m - \chi_0)^{-1}$  of  $\text{YbB}_{66}$  plotted against the temperature  $T$  with modified Curie-Weiss fitting. [127]

Figure 2.6 shows that the magnetic susceptibility of  $\text{YbB}_{66}$  can be well described by the Curie-Weiss law in the high temperature region at  $T > 100$  K. The Curie-Weiss fitting in the high temperature region gives a Curie-Weiss temperature  $\theta = -26.6$  K and an effective magnetic moment  $\mu_{eff} = 4.43 \mu_B$  calculated from the Curie constant  $C$  according to [130]

$$\mu_{eff} = \sqrt{\frac{3k_B}{N_A\mu_B^2} C} \quad (2.3)$$

with  $k_B$ ,  $N_A$  and  $\mu_B$  being the Boltzmann constant, Avogadro constant and Bohr magneton respectively.

The value obtained for the effective magnetic moment  $\mu_{eff} = 4.43 \mu_B$  is close to the literature values for free  $\text{Yb}^{3+}$  ions,  $\mu_{eff}(\text{Yb}^{3+}) = 4.54 \mu_B$ . [131] This result suggests that, unlike Sm in  $\text{SmB}_{66}$  [7] before, Yb in  $\text{YbB}_{66}$  is present mainly or exclusively in a trivalent oxidation state.

The negative Curie-Weiss temperature  $\theta = -26.6$  K for  $\text{YbB}_{66}$  implies antiferromagnetic coupling of the magnetic moments. Etourneau [132] reported in a review article on rare earth borides a Curie-Weiss temperature  $\theta = -30$  K for  $\text{YbB}_{66}$  which is very close to the value found in our study. Negative Curie-Weiss temperatures which have been previously found for other  $\text{REB}_{66}$  compounds have been attributed either to antiferromagnetism or spin-glass behavior. [129,133] In these cases, maxima in the magnetic susceptibility have been reported for temperature  $T < 1$  K.

The absolute value of the Curie-Weiss temperature, which can be seen as a measure of the strength of the exchange interactions [4], is unexpectedly high for  $\text{YbB}_{66}$ . The magnetic properties of  $\text{REB}_{66}$  compounds will be further discussed in Chapter 3.

### 2.3.4 Thermoelectric Properties

The results of the measurement of the thermoelectric properties will be discussed in this section. The literature values of the previously reported measurements for the isostructural compounds  $\text{YB}_{66}$ , [134]  $\text{ErB}_{66}$ , [135]  $\text{YB}_{48}$  [8] and  $\text{SmB}_{66}$  [7] are being used as references.

The temperature dependence of the electrical resistivity of  $\text{YbB}_{66}$  can be seen in Figure 2.7. Surprisingly, the measured values for  $\text{YbB}_{66}$  are close to those of  $\text{SmB}_{66}$  and changes by roughly 4 orders of magnitude between 373 and 973 K. At low temperatures the electrical resistivity of  $\text{YB}_{48}$  is significantly lower than both  $\text{YbB}_{66}$  and  $\text{SmB}_{66}$ , but the difference becomes smaller with increasing temperature. At 973 K the resistivity of  $\text{YbB}_{66}$ ,  $\text{SmB}_{66}$  and  $\text{YB}_{48}$  are very similar. Compared to  $\text{YB}_{66}$  and  $\text{ErB}_{66}$  the electrical resistivity of  $\text{YbB}_{66}$  is lower by roughly 2 orders of magnitude, the difference changing little throughout the whole temperature range.

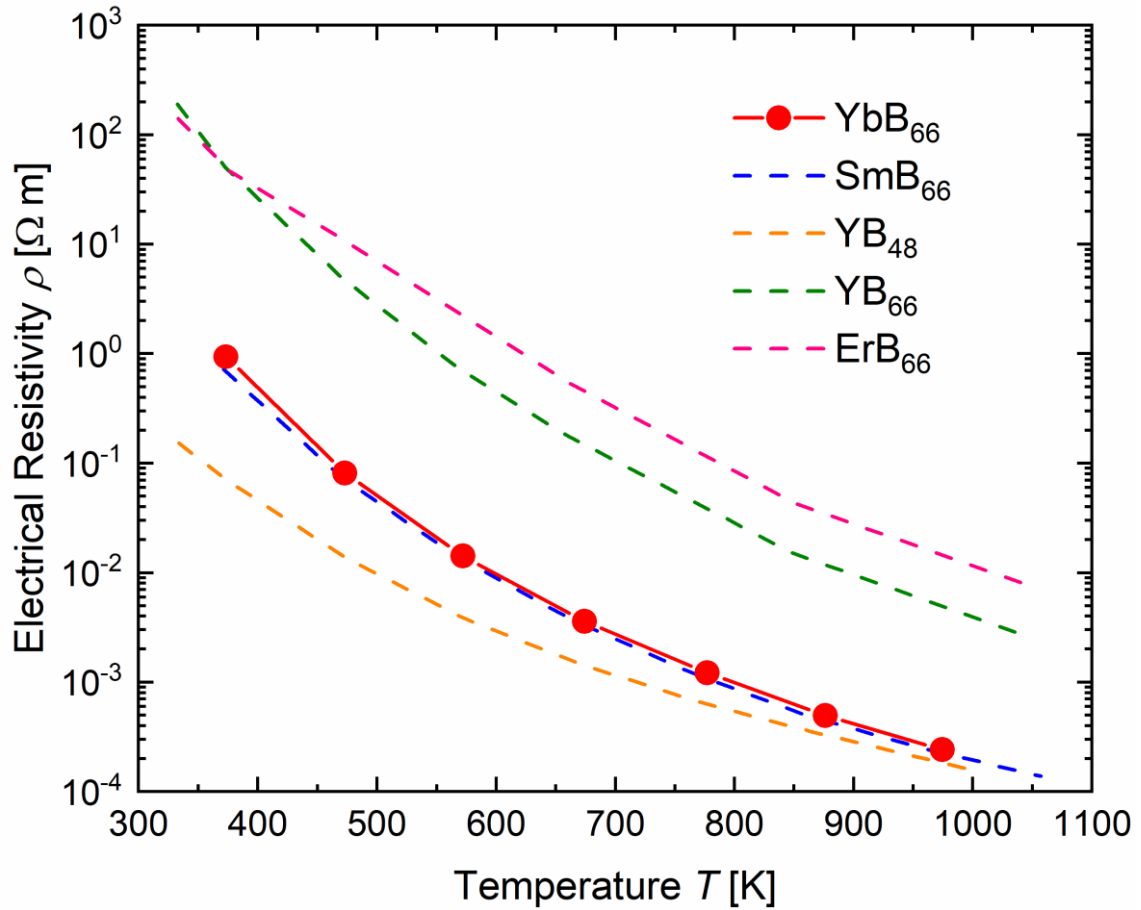


**Figure 2.7** Temperature dependence of the electrical resistivity  $\rho$  with  $\text{SmB}_{66}$  [7],  $\text{YB}_{66}$  [56],  $\text{YB}_{48}$  [8] and  $\text{ErB}_{66}$  [119] as reference values. [127]

The electrical conduction in disordered systems can often be described by Mott's variable range hopping mechanism. [136] The electrical resistivity in such systems follows a temperature dependence which, for hopping in 3 dimensions, follows

$$\rho = \rho_0 \exp\left(\frac{T_0}{T}\right)^{1/4} \quad (2.4)$$

with  $\rho_0$  and  $T_0$  being the characteristic resistivity and temperature respectively. From the fitting of the electrical resistivity in Fig. 2.8 the values  $\rho_0 = 1.32 \times 10^{-17} \Omega \text{ m}$  and  $T_0 = 8.33 \times 10^8 \text{ K}$  were obtained for  $\text{YbB}_{66}$ .

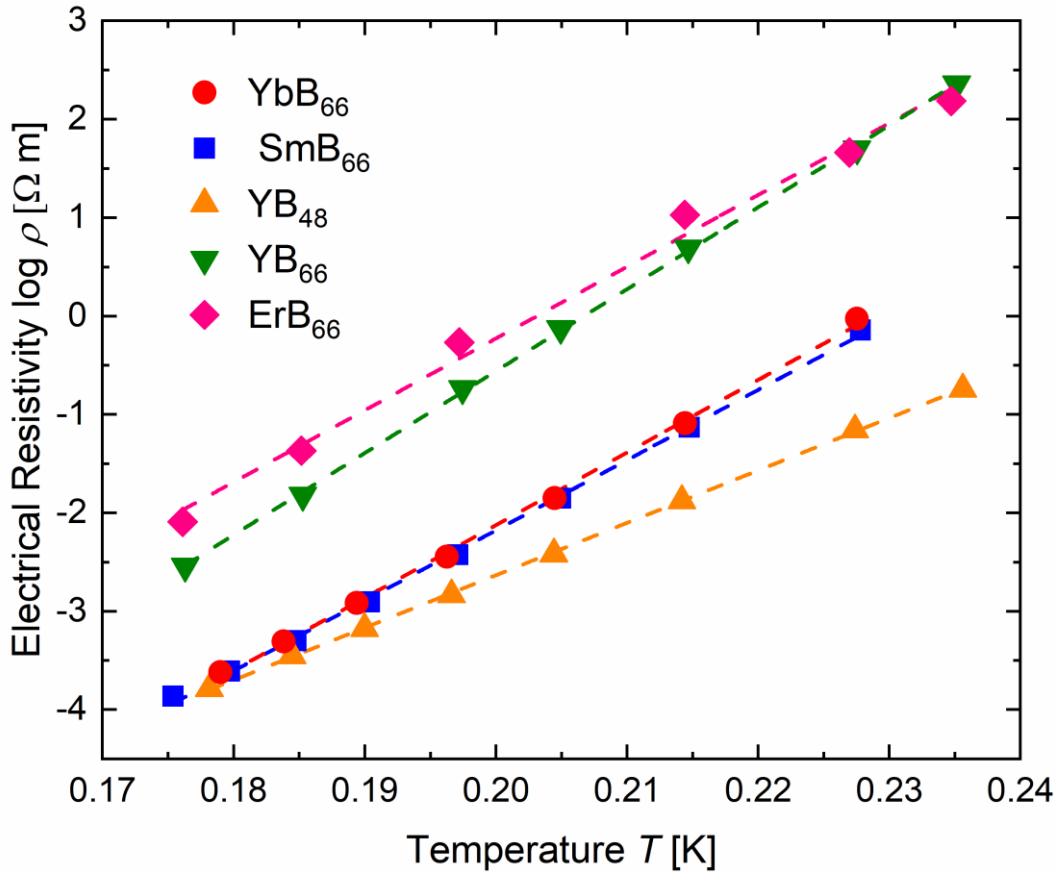


**Figure 2.8** Temperature dependence of  $\text{YbB}_{66} \log \rho$  against  $T^{-0.25}$  according to Mott's variable range hopping mechanism with  $\text{SmB}_{66}$  [7],  $\text{YB}_{66}$  [56],  $\text{YB}_{48}$  [8] and  $\text{ErB}_{66}$  [119] as reference values. [127]

For disordered semiconductors the localization length  $\zeta$  appears to be an important characterization parameter [137,138]. The localization length at the Fermi level can be calculated from the relationship

$$k_B T_0 = \frac{18.1}{N(E_F) \cdot \xi^3} \quad (2.5)$$

with  $k_B$  and  $N(E_F)$  being the Boltzmann constant and the density of states at the Fermi level respectively.

$N(E_F)$  can be derived from the low temperature measurement of the specific heat  $C_p$ , which can be described by

$$C_p = \gamma T + AT^3 \quad (2.6)$$

Using the Sommerfeld coefficient  $\gamma$  derived from fitting the specific heat  $C_p$  according to equation (2.6) it can be used in

$$\gamma = \frac{1}{3} \pi^2 k_B^2 D(E_F) \quad (2.7)$$

together with equation (2.5) calculate the localization length  $\zeta$ .

The determination of the Sommerfeld coefficient  $\gamma$  from the low temperature measurement of the specific heat was unfortunately not possible due to additional contributions which are most likely of magnetic origin. This is also evidenced in the magnetic susceptibility in Fig. 2.6 which deviates from ideal Curie-Weiss behavior towards lower temperatures.

The temperature dependence of the Seebeck coefficient  $\alpha$  of YbB<sub>66</sub> is shown in Figure 2.9. It takes very high, positive values throughout the whole temperature range and drops from almost 600  $\mu\text{V K}^{-1}$  at 373 K to roughly 240  $\mu\text{V K}^{-1}$  at 973 K. The values for YbB<sub>66</sub> are quite comparable to SmB<sub>66</sub> [7] as well as ErB<sub>66</sub> [135] and YB<sub>66</sub> [134] despite the large differences in electrical resistivity.

The thermoelectric properties of YbB<sub>66</sub> have been reported before by Golikova and Tadzhiev, however only room temperature measurements were performed.[54] The reported values are Seebeck coefficient  $\alpha = 270 \mu\text{V K}^{-1}$  and electrical resistivity  $\rho = 1.7 \Omega \text{ m}$  at 300 K. These values are significantly lower than those in this study (electrical resistivity  $\rho = 7.1 \Omega \text{ m}$  at 300K using the temperature dependence of Mott's VRH) indicates, as in the case of YB<sub>48</sub> [8], a more metal-rich composition in the YbB<sub>66</sub> sample of Golikova and Tadzhiev than the given nominal composition. The sample was prepared by arc-melting, so a loss of boron in the synthesis process is a likely explanation for this deviation.

The temperature dependence of the Seebeck coefficient in system following the VRH mechanism has been theoretically investigated. [139,140] Parfenov and Shklyaruk [140] have derived the expression

$$\alpha \approx -\frac{k}{e} \left( \frac{\pi - 2}{\pi} k\sqrt{TT_0} + \frac{2\pi}{3} kT \right) \left( \frac{d \ln N(E)}{dE} \right)_{E=E_F} \quad (2.8)$$

assuming a constant density of states at the Fermi Level. There are two contributions to the Seebeck coefficient. For materials with  $T_0 > 10^4$  the first term  $\alpha \propto T^{1/2}$  is dominant, which can for example be observed in REB<sub>44</sub>Si<sub>2</sub>. [141] In REB<sub>66</sub> the temperature dependence of the Seebeck coefficient is however different and decreases monotonically with increasing temperature. This could be caused by thermally activated charge carriers and will be discussed more in Chapter 3.

The temperature dependence of the power factor  $pf = \alpha^2 \rho^{-1}$  is shown in Figure 2.10. It increases rapidly with increasing temperature and reaches a value of 0.24  $\text{mW m}^{-1} \text{K}^{-2}$  at 973 K, which is very close to the values of YB<sub>48</sub> and SmB<sub>66</sub>.

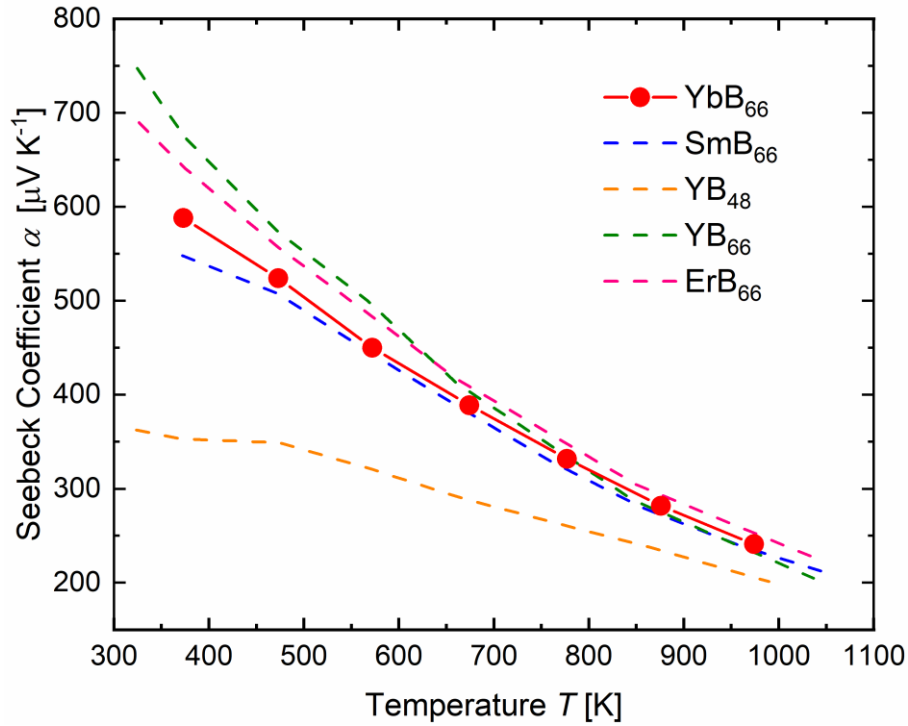


**Figure 2.9** Temperature dependence of the Seebeck coefficient of YbB<sub>66</sub> with SmB<sub>66</sub> [7], YB<sub>66</sub> [56], YB<sub>48</sub> [8] and ErB<sub>66</sub> [119] as reference values. [127]

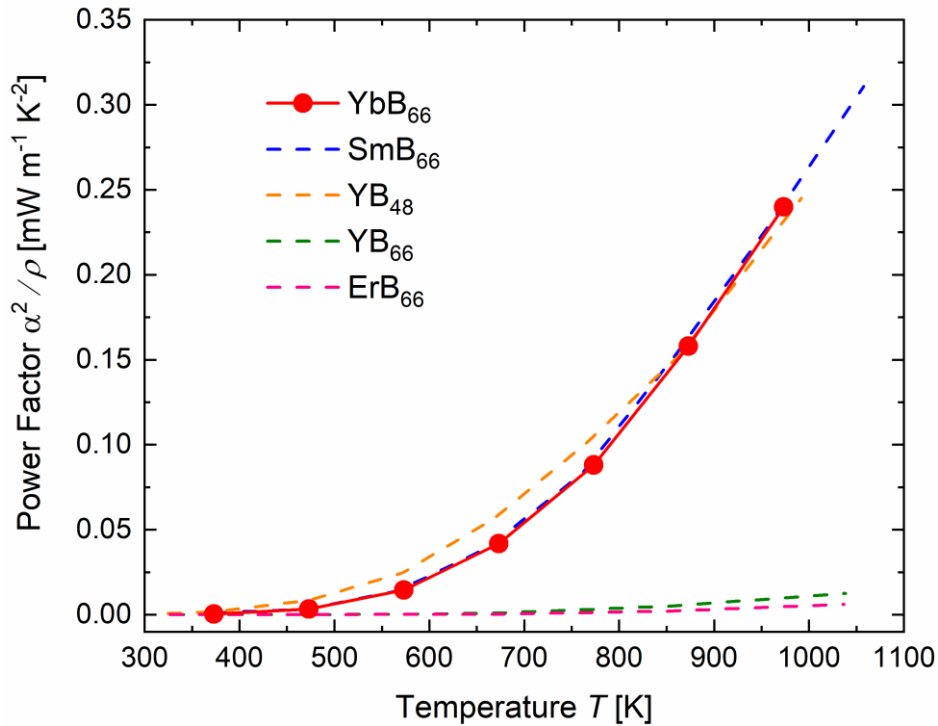


**Figure 2.10** Temperature dependence of the Power Factor of YbB<sub>66</sub> with SmB<sub>66</sub> [7], YB<sub>66</sub> [56], YB<sub>48</sub> [8] and ErB<sub>66</sub> [119] as reference values. [127]

The temperature dependencies of the thermal properties of YbB<sub>66</sub> are shown in the Figures 2.11 – 2.13. The thermal conductivity  $\kappa$  was calculated from  $\kappa = D_t \rho_m C_p$  with  $D_t$ ,  $\rho_m$  and  $C_p$  being the thermal diffusivity, density and specific heat respectively.

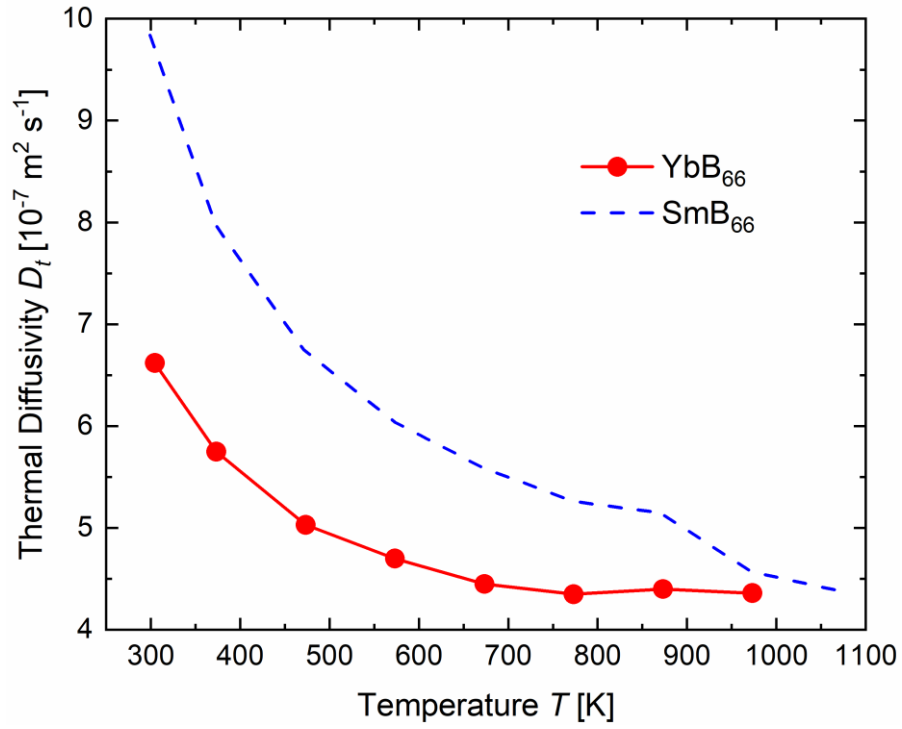


**Figure 2.11** Temperature dependence of the thermal diffusivity  $D_t$  of YbB<sub>66</sub> with SmB<sub>66</sub> [7] as reference.

[127]

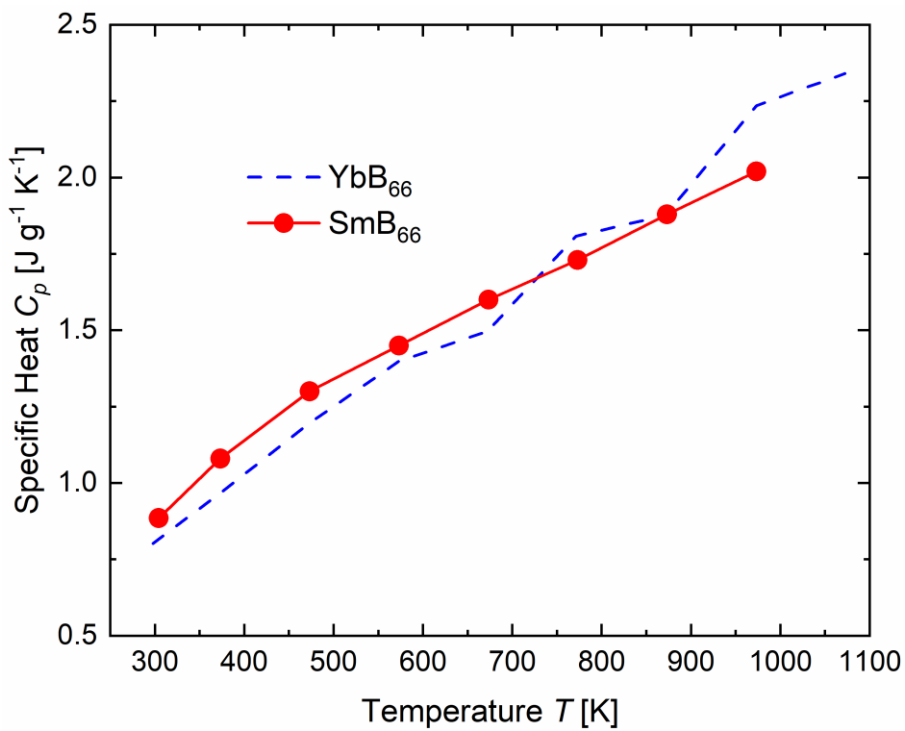


**Figure 2.12** Temperature dependence of the specific heat  $C_p$  of YbB<sub>66</sub> with SmB<sub>66</sub> [7] as reference. [127]

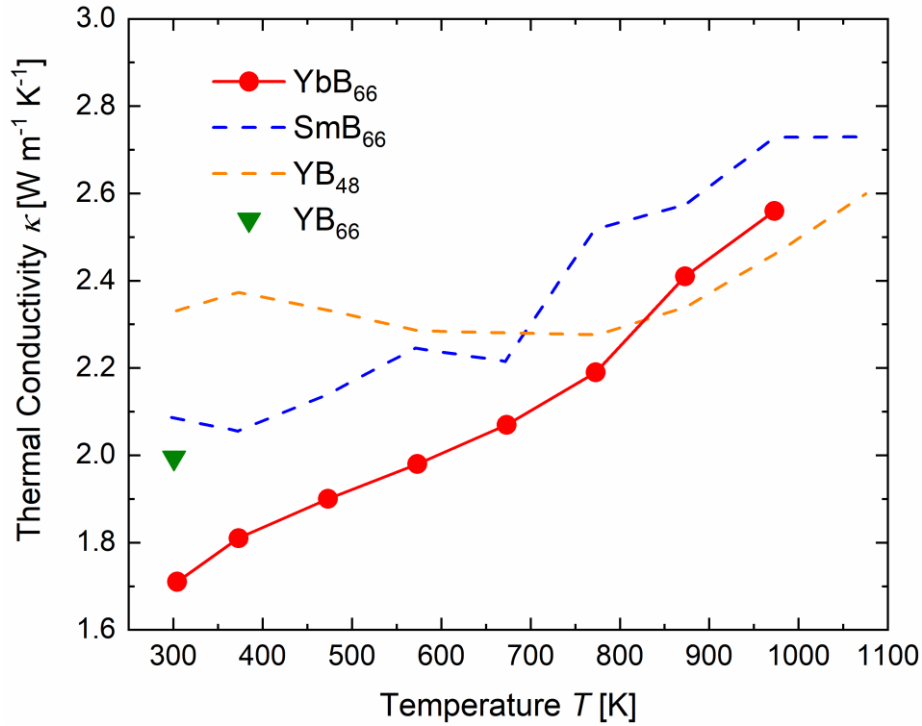


**Figure 2.13** Temperature dependence of the thermal conductivity  $\kappa$  of YbB<sub>66</sub> with SmB<sub>66</sub> [7], YB<sub>66</sub> [56] and YB<sub>48</sub> [8] as reference values. [127]

The thermal conductivity shown in Fig. 2.11 is overall low, especially for a single crystal, and is indicative of the high complexity of the crystal structure. The thermal conductivity shows a small positive temperature dependence ranging from 1.7 to 2.6 W m<sup>-1</sup> K<sup>-1</sup>. This behavior, i.e. increasing thermal conductivity with temperature, is generally observed for materials with complex crystal structures.[37]

The Figure of Merit ZT is shown in Figure 2.14. YbB<sub>66</sub> reaches  $ZT \approx 0.1$  at 973 K, similarly to SmB<sub>66</sub> [7] and YB<sub>48</sub> [8]. However, unlike SmB<sub>66</sub> before we did not observe mixed valence for Yb. Despite that, the thermoelectric properties of YbB<sub>66</sub> and SmB<sub>66</sub> are very similar. It was shown before in YB<sub>48</sub> that higher metal-content can have a beneficial effect on the thermoelectric properties of REB<sub>66</sub> compounds. This is indicated to be the case for YbB<sub>66</sub> whose composition determined from ICP-AES and from the single crystal structure refinement is close to a Yb:B ration of 1:59.

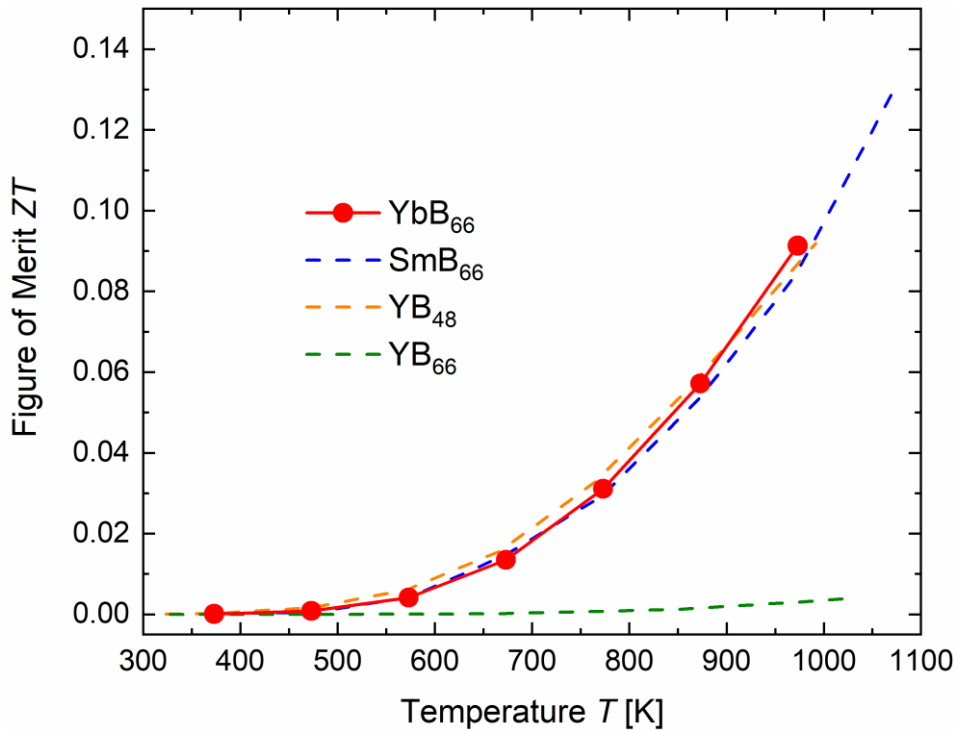


**Figure 2.14** Temperature dependence of the dimensionless Figure of Merit  $ZT$  of  $\text{YbB}_{66}$  with  $\text{SmB}_{66}$  [7],  $\text{YB}_{66}$  [56] and  $\text{YB}_{48}$  [8] as reference values. [127]

## 2.4 Conclusion

In this chapter the results of the measurements of the thermoelectric and magnetic properties of the higher boride compound  $\text{YbB}_{66}$  were discussed in detail. Additionally, the crystal structure of  $\text{YbB}_{66}$  and  $\text{SmB}_{66}$  was refined from single crystal XRD measurements and an updated structural model was proposed.

The effective magnetic moment of  $\text{YbB}_{66}$  suggests that Yb is in a trivalent oxidation state in this compound. Despite that, the thermoelectric properties of  $\text{YbB}_{66}$  and  $\text{SmB}_{66}$  are very similar. The Figure of Merit  $ZT$  reached a value of close to 973 K while still sharply rising. It can be expected to be significantly higher at the working temperatures of potential applications, for example thermal power plant topping cycles with 1500 K.

The composition appears to be an important factor for the thermoelectric performance of  $\text{REB}_{66}$  compounds. The influence of composition and different rare earth elements on the physical properties of  $\text{REB}_{66}$  compounds should be further investigated.

## 2.5 Acknowledgements

The contents of this chapter were published as “P. Sauerschnig, K. Tsuchiya, T. Tanaka, Y. Michiue, O. Sologub, S. Yin, A. Yoshikawa, T. Shishido, and T. Mori, On the thermoelectric and magnetic properties, hardness, and crystal structure of the higher boride  $\text{YbB}_{66}$ , *Journal of Alloys and Compounds* 813 (2020) 152182.” [127] and have been modified for the chapter of this thesis. The work is a continuation of the initial results on the thermoelectric properties of  $\text{YbB}_{66}$  crystals achieved by Kantaro Tsuchiya which can be found in his master thesis “ $\text{YbB}_{66}$  単結晶の熱電的性質“. I wish to thank Dr. Y. Michiue for his work on the single crystal structure refinement of  $\text{YbB}_{66}$  and  $\text{SmB}_{66}$  single crystals as well as Prof. Dr. S. Yin for the hardness measurements on  $\text{YbB}_{66}$ . I also wish to thank Dr. Iwanade Akio from the NIMS Sengen Materials Analysis Station for the ICP-AES determination of the chemical composition and Dr. Shiro Funahashi, Dr. Naoto Hirosaki and Dr. Yoshitaka Matsushita for the measurement of single-crystal X-ray diffraction.

## **Chapter 3: Thermoelectric and Magnetic Properties of Spark Plasma Sintered REB<sub>66</sub> (RE = Y, Sm, Ho, Tm, Yb)**

### 3.1 Introduction

In the previous chapter the thermoelectric properties of single crystalline YbB<sub>66</sub> were investigated in detail. It is possible to obtain large high quality samples of REB<sub>66</sub> from optical floating zone single crystal growth which has been shown on YB<sub>66</sub> in previous investigations. [97] This synthesis process is however technically very challenging and material and time intensive. For the investigation of the thermoelectric properties of REB<sub>66</sub> a simpler and faster synthesis process was required to be able to test several approaches with different elements and compositions.

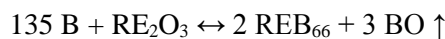
Up to this point, REB<sub>66</sub> had been synthesized from the melt directly either by arc melting, optical floating zone crystal growth or zone melting. [7,8,37,54,129,133] In our study we found however that arc melted samples contained cracks and pores from the cooling down of the melt. Additionally, REB<sub>66</sub> compounds have been reported to melt incongruently in some cases, for instance SmB<sub>66</sub>. [50,128,142] Due to these issues REB<sub>66</sub> samples obtained are not well suited to be used directly for the measurement of the thermoelectric properties.

The new synthesis procedure involving borothermal reduction, arc melting and spark plasma sintering will be discussed in this chapter. Spark plasma sintering is a widely used fabrication method for the densification of powders. Densifying materials with high boron content can however be a very challenging. [40,41,143]

In this study, REB<sub>66</sub> (RE = Y, Sm, Ho, Tm and Yb) were synthesized by the aforementioned new synthesis procedure. Their thermoelectric and magnetic properties were measured and interpreted in referencing previous reports of REB<sub>66</sub> crystals obtained from the optical floating zone method. SmB<sub>66</sub>, TmB<sub>66</sub> and YbB<sub>66</sub> were chosen because Sm, Tm and Yb are elements which form the REB<sub>66</sub> which can exist in a RE(+2)/RE(+3) mixed valence state. YB<sub>66</sub> and HoB<sub>66</sub> were investigated as references of rare earth elements which should only exhibit RE(+3) valence states.

### 3.2 Experimental

The initial step for the synthesis of REB<sub>66</sub> is the borothermal reduction of rare earth oxide with amorphous boron in the induction furnace according to the chemical equation



RE<sub>2</sub>O<sub>3</sub> powders (RE = Y, Sm, Ho, Tm and Yb, Wako Chem.; 99.9%) and amorphous boron powder (New Metals and Chemicals Corporation, Ltd.; 99%) were mixed under ethanol in an agate mortar for 30 – 60 min

and dried overnight under a halogen lamp. The powder mixtures were then transferred into rubber tubes and compacted into rods of roughly 10 mm diameter using a COP with applied pressures of roughly 300 MPa. The rods were then placed inside a h-BN crucible surrounded by a graphite susceptor. The crucible was then heated in a HF induction furnace to 1600°C for 10 h to carry out the borothermal reduction under dynamic vacuum. The formation of REB<sub>66</sub> requires temperatures exceeding 1700°C which is close to the maximum temperature of the induction furnace used. Considering additional temperature gradients within the crucible it was decided to use arc melting to complete the reaction to REB<sub>66</sub>. While arc melting makes it more difficult to control the final composition of the material, it allows the synthesis of higher quantities of the material which were required for carrying out several sintering experiments to achieve good densification in the following SPS step. Following the borothermal reduction in the induction furnace, the sintered rods were melted in an arc furnace with a tungsten electrode on a water-cooled copper plate under Ar atmosphere. A Ti-getter was melted before the melting of the sample to remove residual oxygen from the atmosphere. Each REB<sub>66</sub> was melted completely and flipped over to be completely re-melted at least 3 times for homogeneity.

The melted ingots were subsequently crushed into powder using a stainless steel mortar and sieved to a grain size below 75 µm. The powder was washed in diluted hydrochloric acid (~1 mol l<sup>-1</sup>) overnight to remove the contamination from the stainless steel mortar. The powder was then washed in water, ethanol and acetone in sequence and dried at 100°C.

The REB<sub>66</sub> powders were densified by SPS (Dr. Sinter SPS apparatus (FUJI ELECTRONIC INDUSTRIAL CO., LTD.) in  $\phi = 10$  mm diameter graphite dies lined with h-BN coated graphite paper. The h-BN coated graphite paper was used for easier removal of the sample from the die after sintering. The graphite die was covered by graphite wool to reduce heat losses through radiation at elevated temperatures. The sintering was carried out under dynamic vacuum (< 4 Pa) and applied uniaxial pressure of 50 MPa. The temperature was controlled using an optical pyrometer. The sintering program is shown in Figure 3.1.

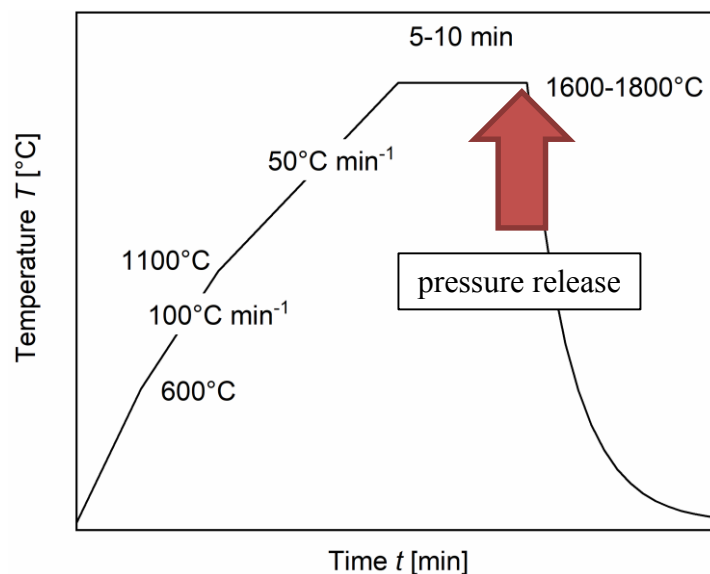


**Figure 3.1** Sintering schedule for REB<sub>66</sub>.

The first step is heating to 600°C over 5 min followed by a heating step at 100°C min<sup>-1</sup> to 1100°C. The heating rate was then changed to 50°C min<sup>-1</sup> up to the final sintering temperature of 1600 – 1800°C depending on the sample. The samples were kept at this temperature for 5 – 10 min. The pressure was released towards the end of the isothermal step to avoid fracturing of the sintered sample during the cooling process. The sintering conditions were determined for each individual REB<sub>66</sub> sample to ensure optimal densification and can be found in Table 3.1.

The density of the samples was measured using Archimedes' method. Powder XRD measurements were performed using a Rigaku Smartlab 3 diffractometer with Cu-K<sub>α</sub> radiation for phase identification. Lattice parameters were determined from the X-Ray diffraction patterns using Rietveld refinement in the Fullprof software. [144]

ICP-AES measurements were performed to determine the chemical composition and possible contamination with C, Si and Fe. For this purpose, the material was dissolved in a mixture of HCl and HNO<sub>3</sub> at elevated temperature.

The thermal diffusivity was measured by LFA in a TC-7000 instrument by ULVAC-Riko in the range of room temperature to 973 K. The specific heat was determined by DSC (NETZSCH STA 449 F3). A crystal of SmB<sub>66</sub> was measured in alumina-lined platinum crucibles against a sapphire reference. (ISO E1269 - 11(2018)). These values were then used to calculate the specific heat for all samples using the Dulong-Petit law and taking the differences in molar weight into account.

The electrical properties (Seebeck coefficient, electrical resistivity) were measured using an ULVAC-Riko ZEM-2 instrument. The measurements were performed in a 4-probe measurement setup under He atmosphere in a temperature range of 373 – 973 K.

The magnetic susceptibility measurements (ZFC – FC) were performed in a MPMS instrument (Quantum Design) which utilizes a SQUID magnetometer. The measurements were performed under an applied field of 1 kOe in a temperature range of 4 – 300 K.

### 3.3 Results and Discussion

#### 3.3.1 Characterization REB<sub>66</sub> Prepared by Spark Plasma Sintering

The early experiments to prepare polycrystalline REB<sub>66</sub> samples were carried out on SmB<sub>66</sub>. Reactive SPS of a mixture of amorphous boron and Sm<sub>2</sub>O<sub>3</sub> powders were unsuccessful. Pre-reacting the powder for the borothermal reduction at 1600°C for 10 h followed by SPS also did not result in high quantities of SmB<sub>66</sub>. In both cases the sintering temperatures were limited to roughly 1600°C. Above this temperature material was squeezed from the graphite dies. XRD analysis of the sintered specimens showed mixtures of mainly SmB<sub>6</sub> and most likely β-rhombohedral boron. The temperature during SPS at the time was insufficient for the formation of SmB<sub>66</sub> by reactive SPS.

Using the arc melting step as described in Section 3.2 helped in the preparation of the polycrystalline  $\text{REB}_{66}$  samples. The powder XRD patterns of the polycrystalline  $\text{REB}_{66}$  samples are shown in Figure 3.2.

**Table 3.1** Summarized sintering parameters and characterization results of  $\text{REB}_{66}$  (RE = Y, Sm, Ho, Tm, Yb) prepared by spark plasma sintering.

	$\text{YB}_{66}$	$\text{SmB}_{66}$	$\text{HoB}_{66}$	$\text{TmB}_{66}$	$\text{YbB}_{66}$
<b>SPS Temperature [°C]</b>	1600	1750	1650	1800	1750
<b>Density <math>\rho_{m,XRD}</math> [g cm<sup>-3</sup>]</b>	2.60	2.74	2.89	2.88	2.84
<b>Density <math>\rho_{m,meas.}</math> [g cm<sup>-3</sup>]</b>	2.52	2.75	2.84	2.88	2.84
<b>Density <math>\rho_{m,rel.}</math> [g cm<sup>-3</sup>]</b>	96.9	100.4	98.3	100.0	100
<b>Lattice parameter a [Å]</b>	23.443	23.483	23.420	23.399	23.395
<b>Chemical Formula (ICP-AES)</b>	$\text{Y}_{1.18}\text{B}_{66}$	$\text{Sm}_{1.01}\text{B}_{66}$	$\text{Ho}_{1.16}\text{B}_{66}$	$\text{Tm}_{1.10}\text{B}_{66}$	$\text{Yb}_{1.00}\text{B}_{66}$
<b>C (ICP-AES) [wt.%]</b>	0.52	0.26	0.69	0.66	1.11
<b>Si (ICP-AES) [wt.%]</b>	0.016	0.011	0.010	0.009	0.073
<b>Fe (ICP-AES) [wt.%]</b>	0.005	0.003	0.006	0.003	0.018

No impurity phases were detected in the powder XRD patterns.

The fracture surface SEM images are shown in Figure 3.3. The microstructures in the fracture surface images make it unfortunately difficult to clearly identify individual grains. Since the initial particle size was ( $\leq 75$  microns) quite large, it is surprising to see such good densification of the sintered samples. For instance, for  $\beta$ -rhombohedral boron, which is structurally quite similar to  $\text{REB}_{66}$ , hot-pressing resulted in relatively porous microstructures. [40] The EDX elemental mapping of boron and the respective RE element for the sintered samples showed homogeneous distribution of the elements in the samples. In the  $\text{SmB}_{66}$  sample small amounts of  $\text{SmB}_6$  are indicated from the elemental mapping and BSE/SE detector SEM images shown in Figure 3.3 and Figure 3.4. Due to the initial crystallization of  $\text{SmB}_6$  indicated from the phase diagrams of the Sm-B binary system and the very high stability of this phase it is likely very difficult to obtain purely single-phase  $\text{SmB}_{66}$  samples. [142,145]

Figure 3.4 also shows a layer of roughly 500  $\mu\text{m}$  from the edge of the sample with high amounts of impurity phases. This can be attributed to interaction with the graphite die and h-BN coated graphite paper due to the high temperatures which are necessary for densification, 1750°C in the case of  $\text{SmB}_{66}$ . The SEM image of  $\text{SmB}_{66}$  (Figure 3.4) also reveals only small amounts of impurity phases,  $\text{SmB}_6$  in this case, in the center of the sample.

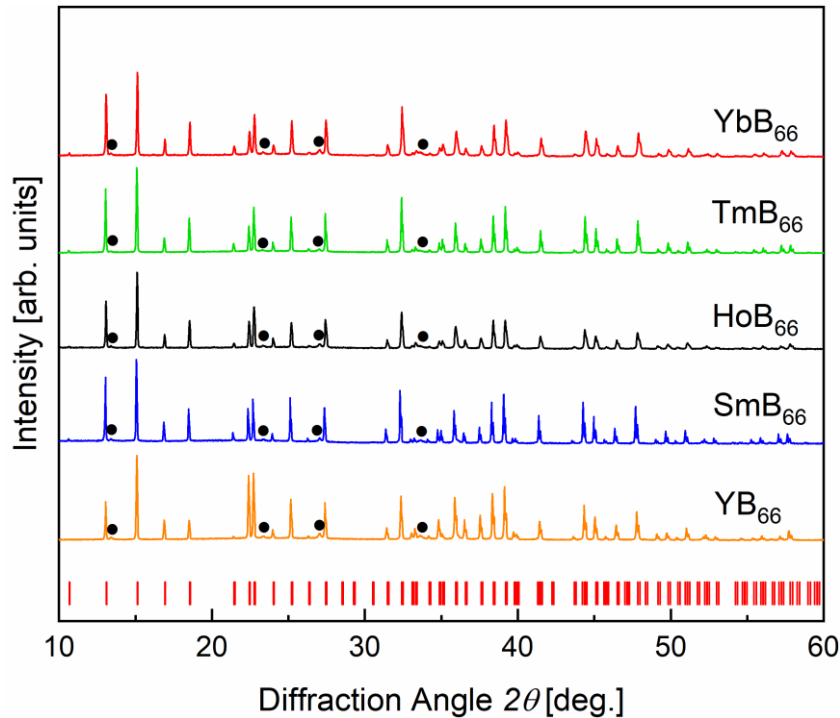


**Figure 3.2** XRD patterns of  $REB_{66}$  ( $RE = Y, Sm, Ho, Tm, Yb$ ) prepared by spark plasma sintering. Peaks of  $Si_3N_4$  (●) introduced from the mortar during pulverization for the powder XRD measurement. The Bragg-positions at the bottom refer to the  $YB_{66}$  structure- type.[46]

The elemental mapping for Yb and B of the  $YbB_{66}$  sample in Figure 3.3 reveals the presence of a secondary phase with higher B content and lower Yb content compared to the main  $YbB_{66}$  phase. It can be assumed from taking the phase equilibria of the binary Yb-B system into consideration that this phase is  $\beta$ -rhombohedral boron. [126,146] This phase could not be detected in the powder XRD patterns seen in Figure 3.2 because of the low atomic number of boron.

The  $YB_{66}$  sample's relative density was slightly lower than the other  $REB_{66}$  samples. The fracture surface image in Figure 3.3 shows small pores due to the incomplete densification. The sintering temperature of  $YB_{66}$  was the lowest at  $1600^\circ C$  used in this series.

The results of the chemical analysis by ICP-AES are summarized in Table 3.1. The samples were checked for their chemical composition as well as contamination with C, Fe and Si which could be present in the starting materials or introduced during the sample preparation. The chemical analysis gives the overall composition of the sample. Since the samples are close to single phase, with the exception of  $YbB_{66}$ , it can be assumed that the overall composition is representative of the phase composition. A small deviation in the composition was observed for the samples  $YB_{66}$ ,  $HoB_{66}$  and  $TmB_{66}$ . In the case of  $YB_{66}$  the nominal composition was  $YB_{62}$ , which had previously been determined as the composition of congruent melting for this phase. [134] In these cases, the measured composition was found to be more metal-rich than the nominal composition. This can most likely be explained by B losses in the synthesis process. Only small amounts of Fe ( $<0.02$  wt.%) and Si ( $<0.1$  wt%) were found. Carbon content ranged from 0.3 – 1.1 wt.% with  $YbB_{66}$  having the highest content.

The  $\text{YbB}_{66}$  sample contained  $\beta$ -rhombohedral boron as shown in Figure 3.3 which has many interstitial sites which can accommodate foreign atoms. [114,147]

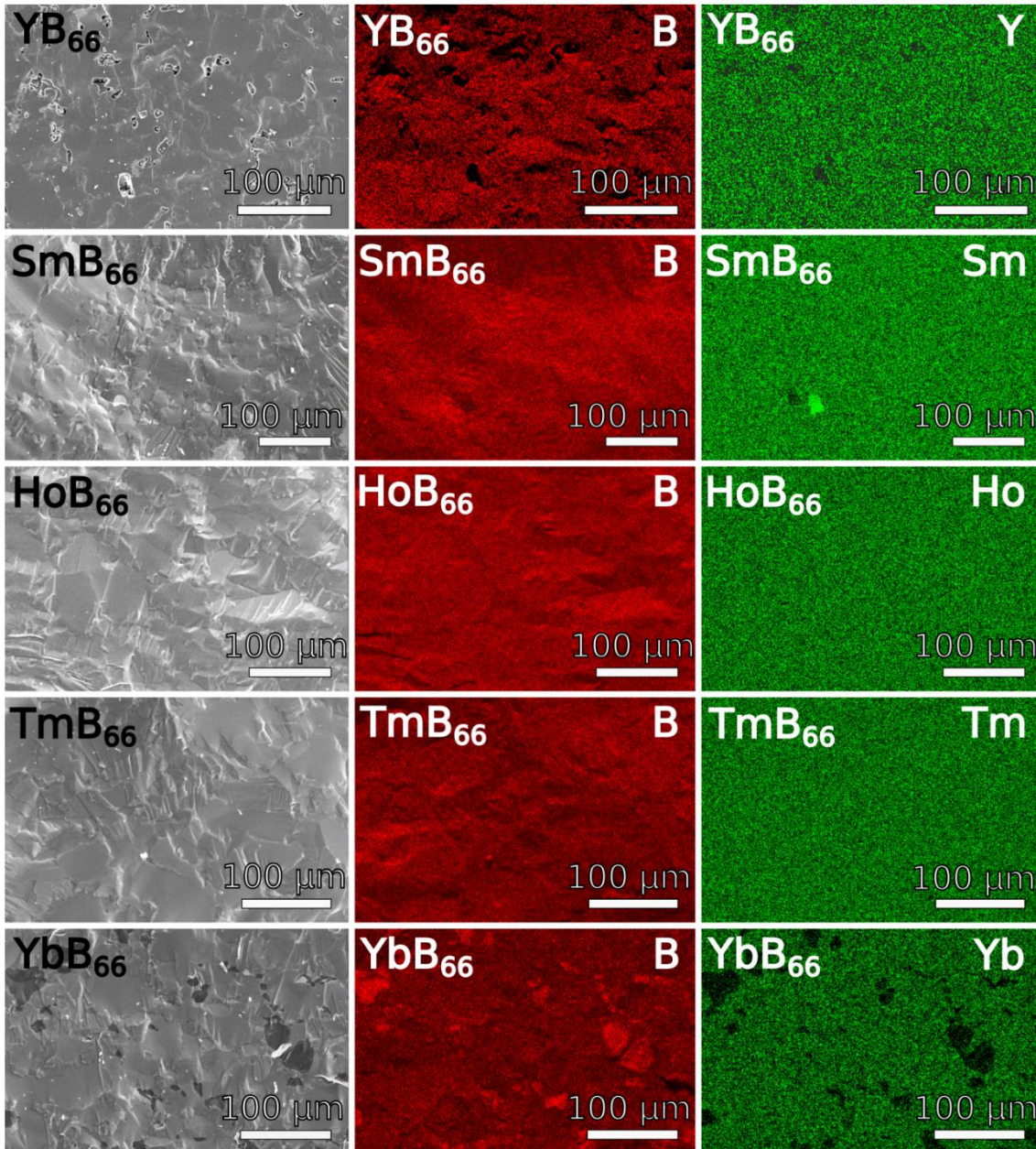


**Figure 3.3** SEM-EDX images of  $\text{REB}_{66}$  samples prepared by spark plasma sintering. The samples show density close to 100% of the theoretical values with the exception of  $\text{YB}_{66}$ . The elemental mapping of the samples shows that the prepared samples are homogenous and single phase, with the exception of  $\text{SmB}_{66}$  and  $\text{YbB}_{66}$ .  $\text{SmB}_{66}$  has small quantities of  $\text{SmB}_6$  (bright).  $\text{Yb}$ -mapping shows a  $\text{Yb}$ -deficient secondary phase, which is slightly  $\text{B}$ -richer, most likely  $\beta$ -rhombohedral boron (bright phase in  $\text{B}$  mapping, dark phase in  $\text{Yb}$  mapping).

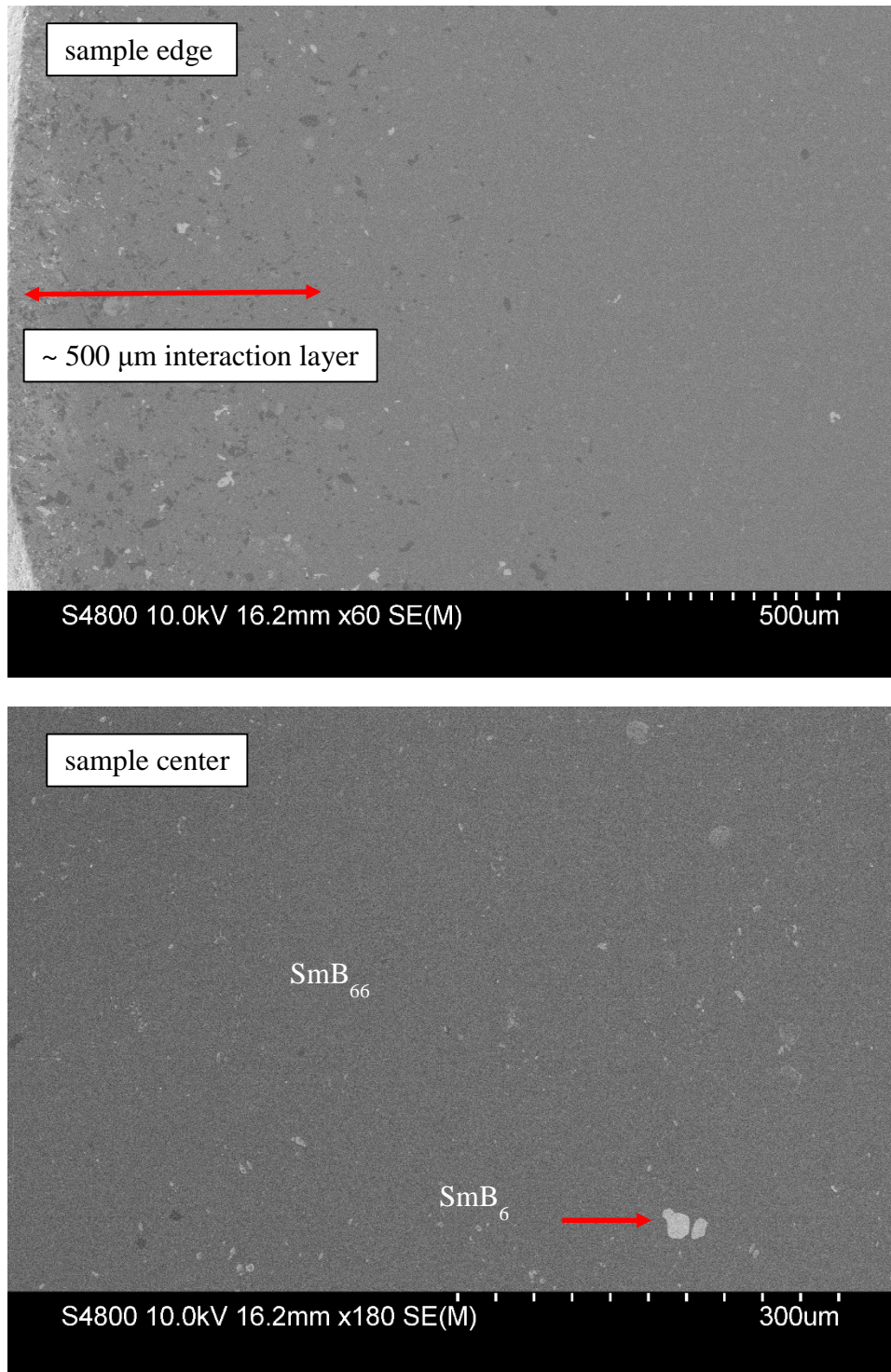


**Figure 3.4** SEM images (mixed BSE+SE detector) of  $\text{SmB}_{66}$  sintered at  $1750^\circ\text{C}$ . The sample contains areas with secondary phases,  $\text{SmB}_6$  (bright) and elemental boron (dark). Top: sample edge, Bottom: sample center.

### 3.3.2 Magnetic Properties

As discussed before in Chapter 2, the magnetic susceptibility of  $\text{REB}_{66}$  was measured to determine the valence state of the rare earth element in this compound. It has been suspected that the improved thermoelectric properties of  $\text{SmB}_{66}$  [7] compared to  $\text{Yb}_{66}$  [134] could be related to  $\text{Sm}(+2)/\text{Sm}(+3)$  mixed valence like it was previously found in  $\text{SmB}_6$ . [148,149] In Chapter 2 it was shown that Yb in  $\text{YbB}_{66}$  is trivalent. To confirm this result and for further characterization the magnetic susceptibility measurements in the temperature range of 4 – 300 K were performed. It is however difficult to determine the oxidation state of Sm from its effective magnetic moment because experimental values can deviate very strongly from the theoretical values of  $\mu_{\text{eff}}(\text{calc.}) = g[J(J+1)]^{1/2}$  with J being the total angular momentum quantum number of the magnetic ground state.[131] In this case using alternative methods, for instance XPS, is preferable. Trivalent Y is diamagnetic. Therefore, only the magnetic properties of  $\text{HoB}_{66}$ ,  $\text{TmB}_{66}$  and  $\text{YbB}_{66}$  will be discussed in this section.

The molar magnetic susceptibility  $\chi_m$  for both ZFC and FC and inverse magnetic susceptibility  $(\chi - \chi_0)^{-1}$  are shown in Figure 3.5 and the relevant parameters are summarized in Table 3.2.

**Table 3.2** Magnetic properties of  $\text{REB}_{66}$  (RE = Ho, Tm, Yb). Curie constant C, Curie-Weiss temperature  $\theta$  and effective magnetic moment  $\mu_{\text{eff}}$  derived from fitting the inverse magnetic susceptibility  $\chi^{-1}$ .

The theoretical effective magnetic moment  $\mu_{\text{eff}}(\text{RE}^{3+}) = g[J(J+1)]^{1/2}$  is taken from “Kittel – Introduction to Solid State Physics” [131].

	<b>HoB<sub>66</sub></b>	<b>TmB<sub>66</sub></b>	<b>YbB<sub>66</sub></b>
<b>Curie Constant C [cm<sup>3</sup> K mol<sup>-1</sup> Oe<sup>-1</sup>]</b>	14.00	7.34	2.59
<b>Curie-Weiss Temperature <math>\theta</math> [K]</b>	-6.7	-11.4	-27.4
<b>Effective Moment <math>\mu_{\text{eff}}</math> [<math>\mu_B</math>]</b>	10.58	7.66	4.55
<b>Effective Moment <math>\mu_{\text{eff}}(\text{RE}^{3+})</math> [<math>\mu_B</math>]</b>	10.60	7.57	4.54
<b>T-indep. Suscebililty <math>\chi_0</math> [cm<sup>3</sup> mol<sup>-1</sup> Oe<sup>-1</sup>]</b>	-0.0024	-0.0013	-0.00066

All investigated  $\text{REB}_{66}$  samples have negative Curie-Weiss temperatures  $\theta$  with increasing absolute values from  $\text{HoB}_{66}$  ( $\theta = -6.7$  K) to  $\text{TmB}_{66}$  ( $\theta = -11.4$  K) to  $\text{YbB}_{66}$  ( $\theta = -27.4$  K). Our results agree well with previous reports for  $\text{HoB}_{66}$  ( $\theta = -6.34$  K) and  $\text{YbB}_{66}$  ( $\theta = -26.6$  K and  $-30$  K respectively). [127,132] Two reports on the magnetic properties of  $\text{REB}_{66}$  (RE = Gd, Tb, Ho, Er and Lu) [133] and  $\text{TbB}_{66}$  [150], respectively, showed lower Curie-Weiss temperatures, with  $\theta$  being in the order of 1 K. Maxima in the temperature dependence of the

magnetic susceptibility have been reported for GdB<sub>66</sub>, TbB<sub>66</sub>, HoB<sub>66</sub> and ErB<sub>66</sub> at temperatures  $T \leq 1$  K [133,151] which have been interpreted as either antiferromagnetic or spin glass transitions.

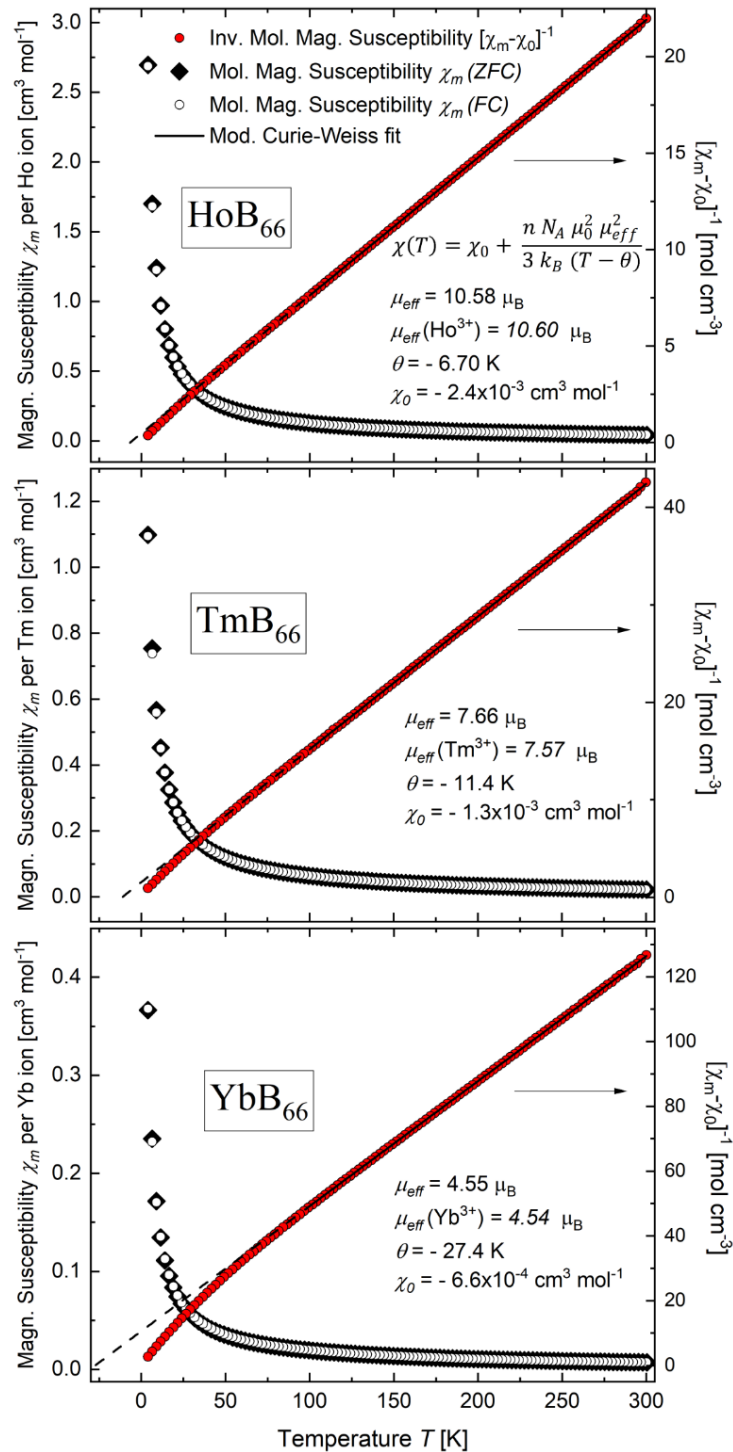


**Figure 3.5** Magnetic Susceptibility of REB<sub>66</sub> (RE = Ho, Tm, Yb) prepared by spark plasma sintering measured with an applied magnetic field of  $H = 1$  kOe. Theoretical values for  $\mu_{eff}(\text{RE}^{3+}) = g[J(J+1)]^{1/2}$  taken from “Kittel – Introduction to Solid State Physics”. [131] The curve fitting was performed for the temperature region 100 – 300 K in which all samples follow ideal Curie-Weiss behavior. The dashed line shows the continuation of the fitting curve up to the respective Curie-Weiss temperature.

The Curie-Weiss temperatures for  $\text{HoB}_{66}$ ,  $\text{TmB}_{66}$  and  $\text{YbB}_{66}$  are plotted in Figure 3.6. The Curie-Weiss temperature can be seen as a measure of the magnetic exchange interactions between the magnetic moments. The trend which was observed in this study on  $\text{REB}_{66}$  is opposite to what would be expected for the RKKY (coupling by conduction electrons) and dipole-dipole (direct coupling between magnetic moments) coupling mechanisms. This has been discussed before for the higher boride compound  $\text{REB}_{44}\text{Si}_2$  where deviations from these aforementioned coupling mechanisms were found. It has been argued that in the case of  $\text{REB}_{66}$  the RKKY and dipole-dipole exchange interactions are unlikely due to the lack of conduction electrons and relatively large distances between the rare earth ions. [4,5,133] Coupling through  $\text{B}_{12}$  icosahedra was proposed as an alternative coupling mechanism in these materials [4] which could explain the unusually large Curie-Weiss temperatures, e.g. in the case of  $\theta = -27.4$  K for  $\text{YbB}_{66}$ .

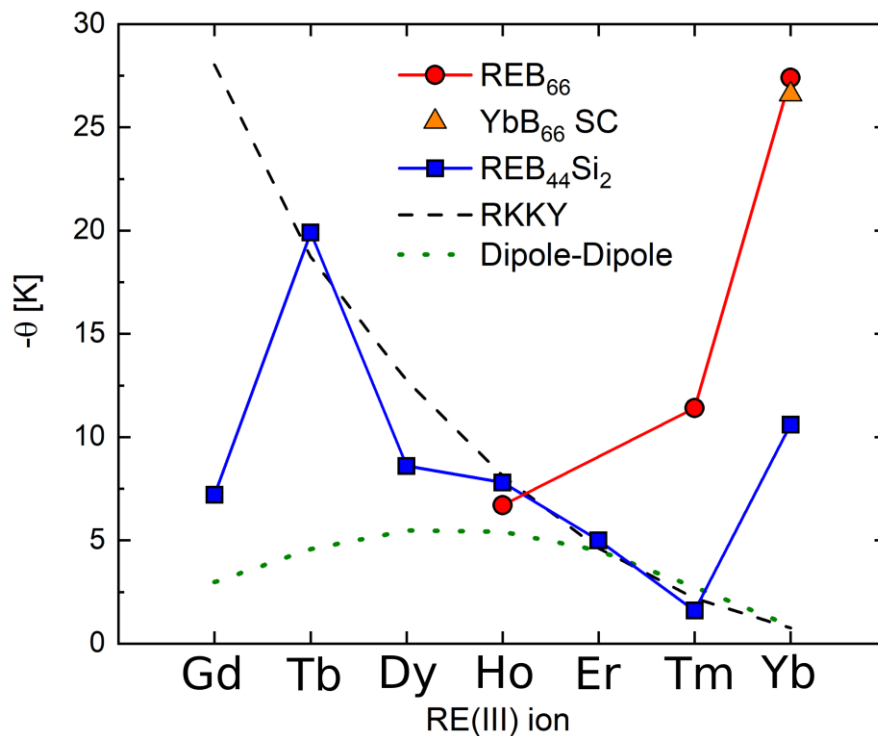


**Figure 3.6** Plot of the Curie-Weiss temperatures of  $\text{REB}_{66}$  for the trivalent rare earth ions adapted from T.

Mori.[4] Value for  $\text{YbB}_{66}$  single crystal from P. Sauerchnig et al.[127]

The values for the effective magnetic moment correspond very well to the theoretical values of the free trivalent rare earth ions [131] with  $10.58 \mu_B$  vs.  $10.60 \mu_B$ ,  $7.66 \mu_B$  vs.  $7.59 \mu_B$ , and  $4.55 \mu_B$  vs.  $4.54 \mu_B$  for  $\text{HoB}_{66}$ ,  $\text{TmB}_{66}$ , and  $\text{YbB}_{66}$  respectively.

### 3.3.3 Thermoelectric Properties

The electrical resistivity of the polycrystalline spark plasma sintered REB<sub>66</sub> samples are shown in Figure 3.7. The data for single crystals of SmB<sub>66</sub> and YbB<sub>66</sub> were plotted as reference values. [7,127]

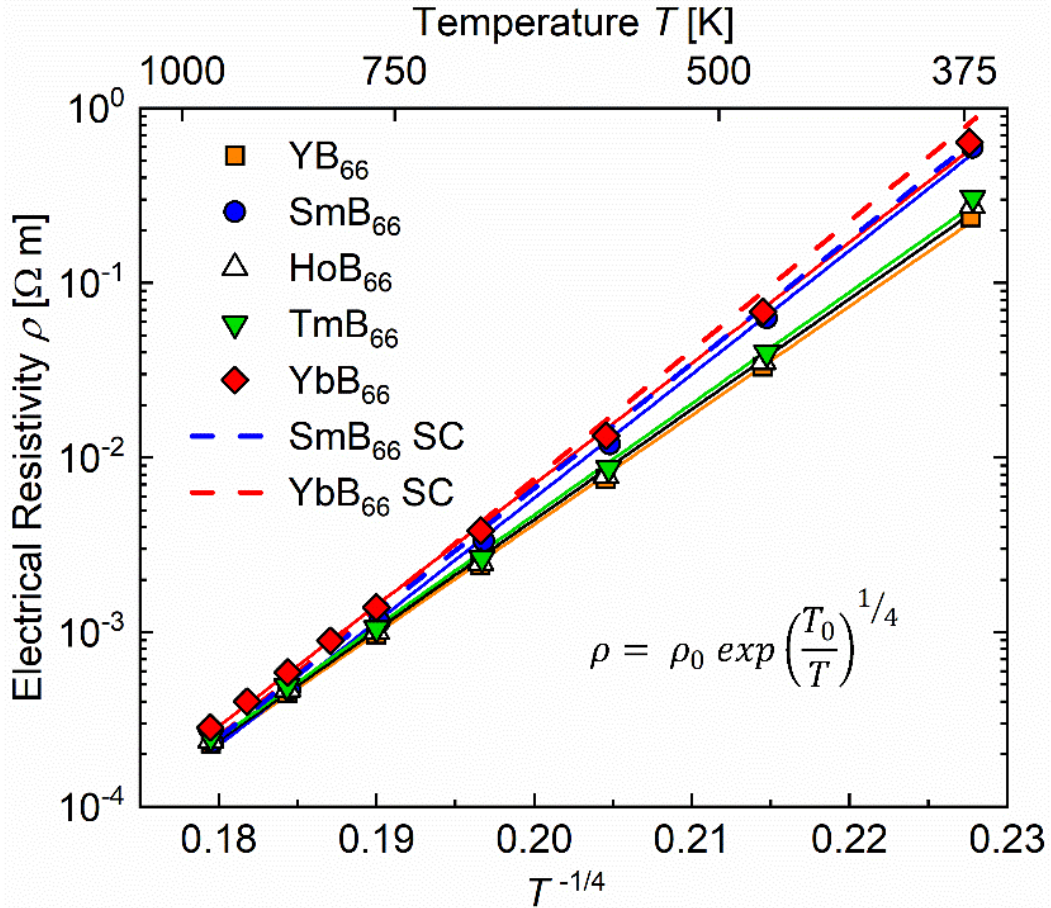


**Figure 3.7** Electrical resistivity  $\rho$  for REB<sub>66</sub> (RE = Y, Sm, Ho, Tm, Yb) according to Mott's variable range hopping mechanism prepared by spark plasma sintering. Data for the single crystal of SmB<sub>66</sub> and YbB<sub>66</sub> plotted as a reference. [7,127]

It can be seen that the electrical resistivity of all investigated REB<sub>66</sub> samples follows Mott's variable range hopping mechanism in 3 dimensions [54,137,152] given by

$$\rho = \rho_0 \exp\left(\frac{T_0}{T}\right)^{1/4} \quad (3.1)$$

with  $\rho_0$  and  $T_0$  being the characteristic resistivity and characteristic temperature respectively and have been summarized in Table 3.3. As discussed in Chapter 2, the electronic states of REB<sub>66</sub> are highly localized. The localization length  $\xi$  is a measure for the disorder in a system and inversely related to the characteristic temperature  $T_0$  through

$$\xi = \sqrt[3]{\frac{18.1}{N(E_F) k_B T_0}} \quad (3.2)$$

with  $N(E_F)$  is the density of states at the Fermi level. [137] A high characteristic temperature  $T_0$  indicates higher levels of disorder in the system. As an example  $\text{YB}_{66}$  ( $T_0=7.2 \times 10^8$  K and  $\zeta = 0.056$  nm) [153] is more disordered than  $\text{YB}_{44}\text{Si}_2$  ( $T_0=1.4 \times 10^8$  K and  $\zeta = 0.27$  nm) [154] which has also been indicated in the low temperature measurements of the thermal conductivity of both compounds. [154] Compared to the amorphous-like thermal conductivity of  $\text{YB}_{66}$  indicative of a disordered structure, the thermal conductivity of  $\text{YB}_{44}\text{Si}_2$  is more similar to crystalline solids.

**Table 3.3** Characteristic temperatures and resistivity of  $\text{REB}_{66}$  (RE=Y, Sm, Ho, Tm, Yb) according to Mott's variable-range hopping (VRH) mechanism.

	<b>YB<sub>66</sub></b>	<b>SmB<sub>66</sub></b>	<b>HoB<sub>66</sub></b>	<b>TmB<sub>66</sub></b>	<b>YbB<sub>66</sub></b>
<b>Characteristic resistivity <math>\rho_0</math> [<math>\Omega</math> m]</b>	$1.3 \times 10^{-15}$	$3.9 \times 10^{-17}$	$9.9 \times 10^{-16}$	$8.1 \times 10^{-16}$	$9.6 \times 10^{-17}$
<b>Characteristic temperature <math>T_0</math> [K]</b>	$4.3 \times 10^8$	$7.1 \times 10^8$	$4.5 \times 10^8$	$4.7 \times 10^8$	$6.5 \times 10^8$

The measured Seebeck coefficients of the polycrystalline spark plasma sintered  $\text{REB}_{66}$  samples are shown in Figure 3.8. The data for single crystals of  $\text{SmB}_{66}$  and  $\text{YbB}_{66}$  were plotted as reference values. Similar to the single crystalline  $\text{REB}_{66}$  investigated earlier, the Seebeck coefficient shows very high values at 373 K of 400 to 600  $\mu\text{V K}^{-1}$  which converge towards 250  $\mu\text{V K}^{-1}$  at 973 K for all  $\text{REB}_{66}$  samples.

As mentioned in Chapter 2, materials following Mott's variable range hopping conduction mechanism are expected to display a  $\alpha \propto T^{1/2}$  [139,140] as for example it has been shown experimentally for  $\text{REB}_{44}\text{Si}_2$ . [119] In the case of  $\text{REB}_{66}$  the Seebeck coefficient decreases monotonically with increasing temperature.

In disordered solids the Fermi level  $E_F$  is expected to lie within the band tails where electronic states are localized with low mobility due to the so-called mobility gap. [136] Electronic states in the center of the bands on the other hand are non-localized with high mobility. A mixture of localized and non-localized states (thermally excited) can be expected to contribute to both the electric resistivity and Seebeck coefficient and depending on the temperature either contribution can be dominant. Golikova and Tadzhev [54] found that the temperature dependence of the electrical resistivity and Seebeck coefficient changed to that of non-localized states above a certain transition temperature. This transition temperature can be different for the Seebeck coefficient and the electrical resistivity due to different contributions from localized and non-localized electronic states to both.

This could explain why a typical VRH temperature dependence of hopping between localized states was observed for the electrical resistivity (Figure 3.7) while non-localized states might contribute more towards the Seebeck coefficient (Figure 3.8).

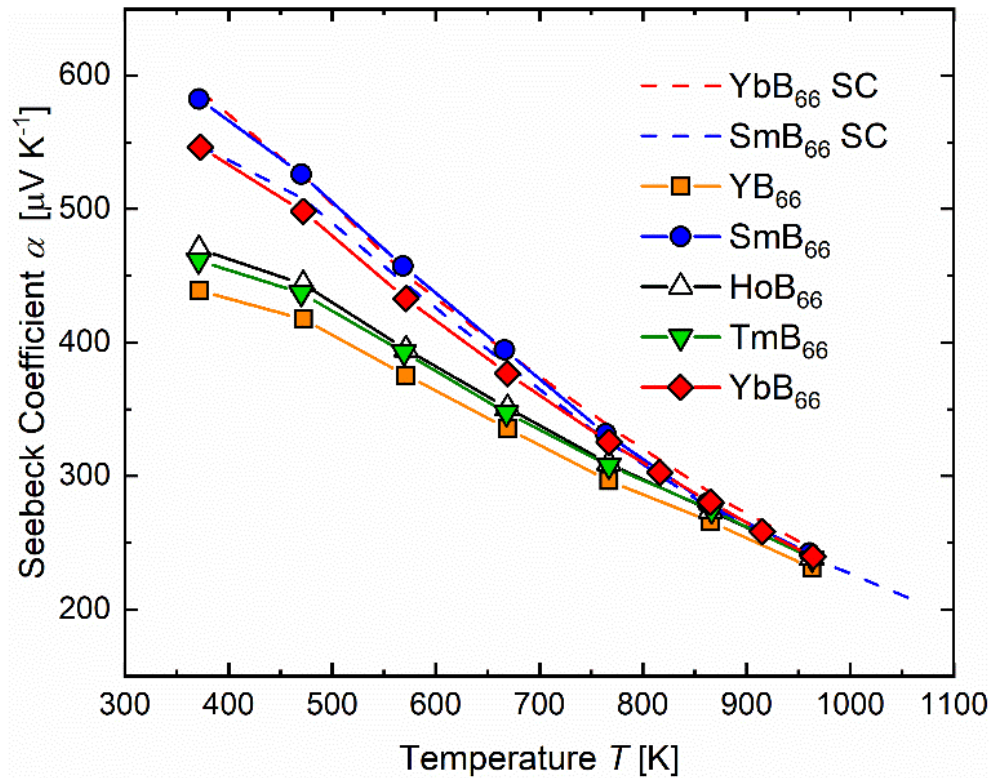


**Figure 3.8** Seebeck coefficient  $\alpha$  for  $\text{REB}_{66}$  (RE = Y, Sm, Ho, Tm, Yb) prepared by spark plasma sintering. Data for the single crystal of  $\text{SmB}_{66}$  and  $\text{YbB}_{66}$  plotted as a reference. [7,127]

Interestingly, there is little difference in the electrical properties between the polycrystalline spark plasma sintered  $\text{REB}_{66}$  samples and their single crystalline counterparts as can be seen in Figures 3.7 and 3.8. Generally, the electrical resistivity would be expected to be higher in polycrystalline materials due to scattering of charge carriers on grain boundaries reducing their mobility. This effect is more pronounced in cases where the grain size is similar to the mean free path of the charge carriers. These effects are most likely negligible in a highly disordered material like  $\text{REB}_{66}$  in which electronic transport occurs through Mott's VRH with high density ( $\sim 100\%$  relative density) and large grain size (initial grain size  $\leq 75 \mu\text{m}$ ).

The electrical resistivity and Seebeck coefficient show a dependence on the chemical composition. Increasing amounts of RE in the structure lead to a decrease in the Seebeck coefficient and electrical resistivity as can be seen when comparing Table 3.1 and Figures 3.7 and 3.8. This compositional dependence has previously been observed for  $\text{YB}_{48}$ . [8] In our samples we did however not observe differences in thermoelectric performance due to these changes in compositions. The differences are pronounced at lower temperatures. The electrical resistivity and Seebeck coefficients of all  $\text{REB}_{66}$  samples at higher temperatures converge towards very similar values.

The power factor  $pf = \alpha^2 \rho^{-1}$  of the polycrystalline spark plasma sintered  $\text{REB}_{66}$  samples are shown in Figure 3.9. The data for single crystals of  $\text{SmB}_{66}$  and  $\text{YbB}_{66}$  were plotted as reference values. [7,127] The power factors of all investigated samples show very similar values between each other and also compared to the values for the single crystals of  $\text{SmB}_{66}$  and  $\text{YbB}_{66}$ . The power factor rises very sharply with increasing

temperature due to the drastic decrease in electrical resistivity (Figure 3.7). Values of roughly  $0.25 \text{ mW m}^{-1} \text{ K}^{-2}$  at 973 K were determined for the polycrystalline  $\text{REB}_{66}$  samples. The power factor of spark plasma sintered  $\text{YbB}_{66}$  is slightly lower which can most likely be attributed to  $\beta$ -rhombohedral boron which is present as a secondary phase.

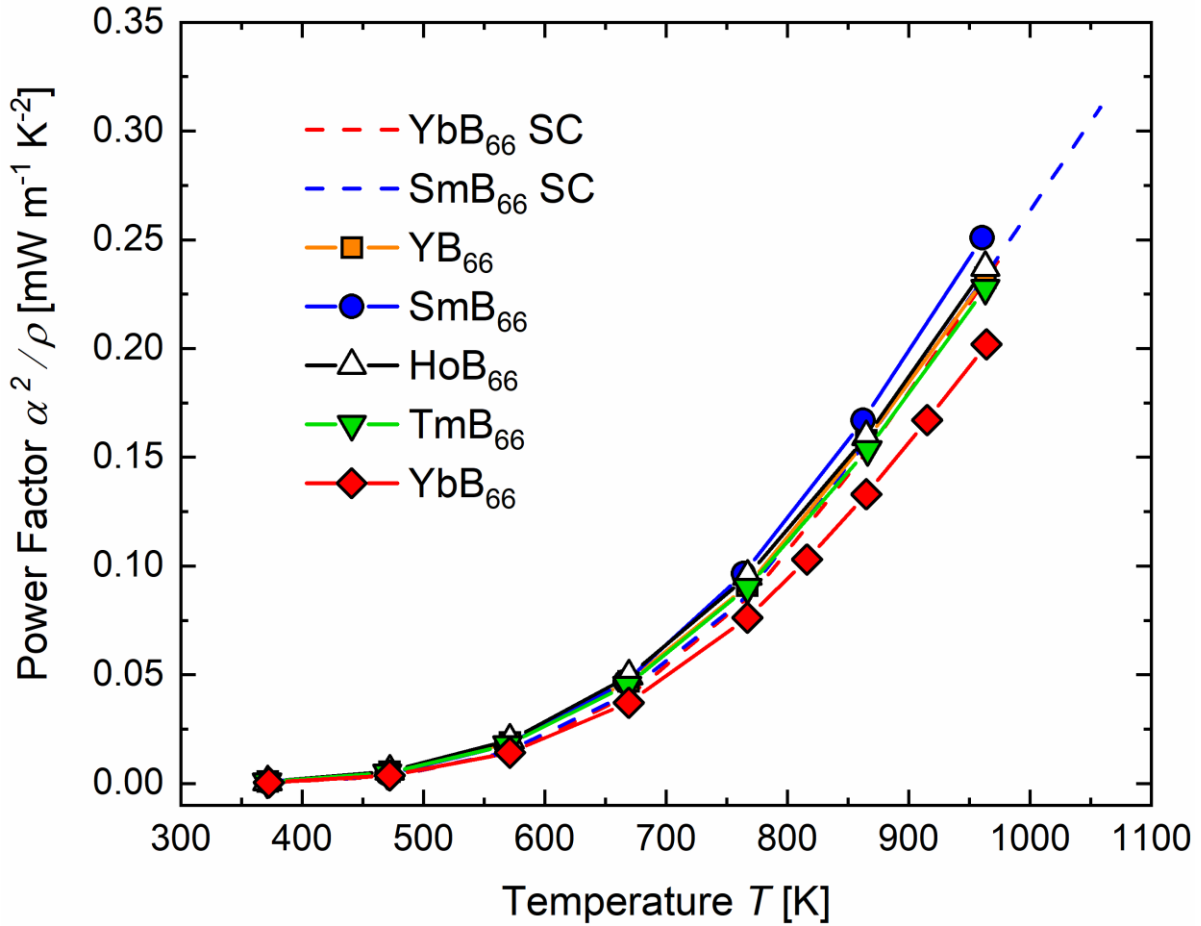


**Figure 3.9** Power Factor  $pf = \alpha^2/\rho$  for  $\text{REB}_{66}$  ( $\text{RE} = \text{Y}, \text{Sm}, \text{Ho}, \text{Tm}, \text{Yb}$ ) prepared by spark plasma sintering. Data for the single crystal of  $\text{SmB}_{66}$  and  $\text{YbB}_{66}$  plotted as a reference. [7,127]

The thermal conductivity of the polycrystalline spark plasma sintered  $\text{REB}_{66}$  samples are shown in Figure 3.10. The data for single crystals of  $\text{SmB}_{66}$  and  $\text{YbB}_{66}$  were plotted as reference values. It is calculated from  $\kappa = D_t \rho_m C_p$  with  $\kappa$ ,  $D_t$ ,  $\rho_m$ ,  $C_p$  being the thermal conductivity, thermal diffusivity, density and specific heat capacity respectively.

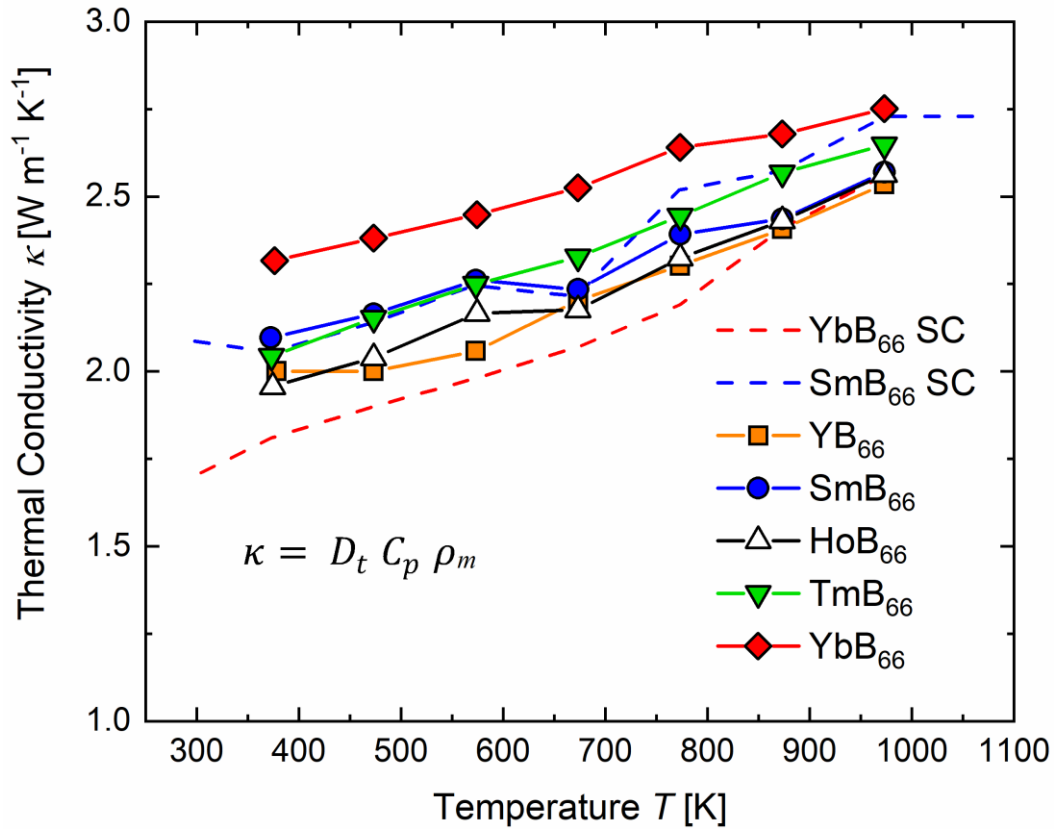


**Figure 3.10** Thermal conductivity  $\kappa$  of  $\text{REB}_{66}$  ( $\text{RE} = \text{Y}, \text{Sm}, \text{Ho}, \text{Tm}, \text{Yb}$ ) prepared by spark plasma sintering.  $D_t$ ,  $C_p$  and  $\rho_m$  are the thermal diffusivity, specific heat and density respectively. Data for the single crystal of  $\text{SmB}_{66}$  and  $\text{YbB}_{66}$  plotted as a reference. [7,127]

In all cases the thermal conductivity ranges from roughly  $2 - 2.5 \text{ W m}^{-1} \text{ K}^{-1}$  with a small, positive temperature dependence which can be observed in disordered materials. [37] The thermal conductivity can be assumed to be almost exclusively due to the lattice contribution.

The thermal conductivity showed little difference between the different  $\text{REB}_{66}$  investigated and between polycrystalline spark plasma sintered samples and single crystals of  $\text{REB}_{66}$  prepared by the optical floating zone method. The influence of the scattering of phonons on grain boundaries in polycrystalline  $\text{REB}_{66}$  appears to be small similar to the previous discussion of the electrical resistivity. The investigation of the low temperature thermal properties of  $\text{LuB}_{66}$  [155] found that the disorder in the RE atomic sublattice and anharmonic bonding to be the most likely cause of this glass-like thermal conductivity of  $\text{REB}_{66}$ .

The figure of merit  $ZT$  of the polycrystalline spark plasma sintered  $\text{REB}_{66}$  samples is shown in Figure 3.11. The data for single crystals of  $\text{SmB}_{66}$  and  $\text{YbB}_{66}$  were plotted as reference values. The maximum  $ZT$  found in this study is  $\sim 0.1$  at 973 K and similar for all  $\text{REB}_{66}$  samples. The figure of merit of the spark plasma sintered polycrystalline  $\text{YbB}_{66}$  is slightly lower than the other  $\text{REB}_{66}$  which could be attributed to the presence of  $\beta$ -rhombohedral boron as a secondary phase. The figure of merit has a strong positive temperature dependence and can be expected to increase significantly with increasing temperature. The overall thermoelectric

performance of the spark plasma sintered samples is equivalent to that of the single crystals of  $\text{SmB}_{66}$  [7],  $\text{YbB}_{66}$  [127] and  $\text{YB}_{48}$  [8] from previous reports.

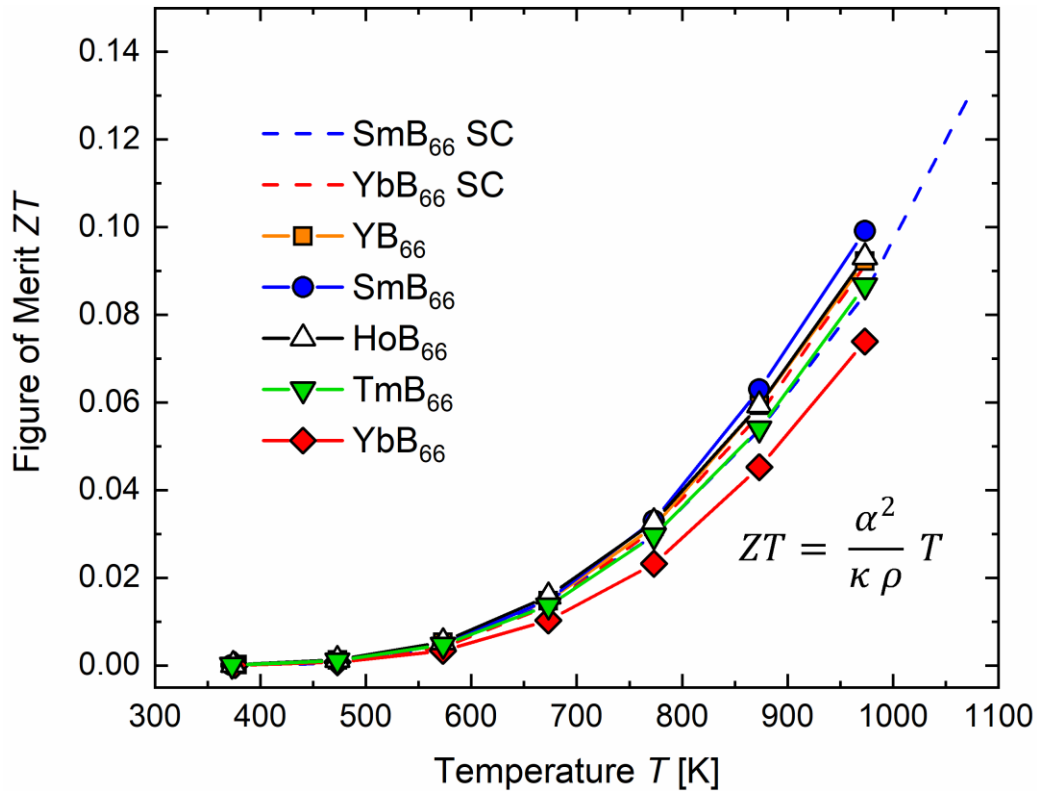


**Figure 3.11** Figure of merit  $ZT$  of  $\text{REB}_{66}$  ( $\text{RE} = \text{Y}, \text{Sm}, \text{Ho}, \text{Tm}, \text{Yb}$ ) prepared by spark plasma sintering.  $\alpha$ ,  $\kappa$  and  $\rho$  are the Seebeck coefficient, thermal conductivity and electrical resistivity respectively. The data of Seebeck coefficient and resistivity were interpolated to match the measurement temperature of the thermal conductivity. Data for the single crystal of  $\text{SmB}_{66}$  and  $\text{YbB}_{66}$  plotted as a reference. [7,127]

The thermoelectric properties of  $\text{REB}_{66}$  appear to not depend on the different rare earth element. In all investigated cases the rare earth element is found in its trivalent state in  $\text{REB}_{66}$ , and no mixed valence was indicated. The valence state of Sm in  $\text{SmB}_{66}$  should be determined again using an alternative method to the magnetic susceptibility measurement, e.g. XPS. Our results support previous reports on the electrical properties of  $\text{REB}_{66}$  ( $\text{RE} = \text{Sm}, \text{Gd}$  and  $\text{Yb}$ ) compounds. [54] In that investigation it was found that the Seebeck coefficients and electrical conductivities of all 3 investigated  $\text{REB}_{66}$  compounds could be plotted on common curves against the charge carrier concentration. The main factor influencing the electrical properties of  $\text{REB}_{66}$  appears to be the composition and the presence of secondary phases.

So far it is not entirely understood what the origin of the significantly higher electrical resistivity of the previously investigated  $\text{YB}_{66}$  [56] and  $\text{ErB}_{66}$  [119] single crystals is. The measurement of the Hall effect to gain insight on the charge carrier concentration and mobility could help clarify the issue, even if the interpretation of the Hall measurements can be difficult in the case of VRH conduction. Unfortunately, these measurements have not yet been successful due to the very low charge carrier mobility of these materials.

### 3.4 Conclusion

In this chapter an alternative synthesis method for the higher boride compound  $\text{REB}_{66}$  ( $\text{RE} = \text{Y}, \text{Sm}, \text{Ho}, \text{Tm}$  and  $\text{Yb}$ ) has been described in detail. The synthesis involves the borothermal reduction of amorphous boron and rare earth oxide powders, arc melting and densification by spark plasma sintering. Utilizing this new process, a series of  $\text{REB}_{66}$  samples were prepared with close to 100% relative density and little to no impurity phases.

The measurement of the thermoelectric and magnetic properties of the sintered polycrystalline  $\text{REB}_{66}$  revealed that the thermoelectric properties appear to be almost independent of the rare earth element. Mixed valence, as previously described for  $\text{SmB}_{66}$ , was not indicated in this study. Further studies on the compositional dependence of the thermoelectric properties are necessary to show this conclusively. Additionally, it was shown that there appears to be no difference in the thermoelectric performance between polycrystalline  $\text{REB}_{66}$  prepared by our synthesis process and single crystals of  $\text{REB}_{66}$  grown by the optical floating zone method. [7,8,127] This is attributed to the complex crystal structure of  $\text{REB}_{66}$  and the electrical transport by Mott's VRH and amorphous-like thermal conductivity.

The independence of the thermoelectric properties on the microstructure could be beneficial for industrial applications. The preparation of polycrystalline materials has additional advantages and allows for instance the in-situ preparation of composites. [44,70]

The synthesis process can be further optimized by finding a way to better control the composition, for example by direct synthesis of the  $\text{REB}_{66}$  phase in the induction furnace without the additional arc melting step and the use of ball milling to reduce the particle size and thus the necessary sintering temperature. [102]

### 3.5 Acknowledgement

The contents of this chapter have been submitted as a manuscript "P. Sauerchnig, J.B. Vaney, Y. Michiue, K. Yubuta, A. Yoshikawa, T. Shishido, and T. Mori "Thermoelectric and magnetic properties of spark plasma sintered  $\text{REB}_{66}$  ( $\text{RE} = \text{Y}, \text{Sm}, \text{Ho}, \text{Tm}, \text{Yb}$ )" and have been modified for this thesis.

I wish to thank Keiko Suzuta for the DSC measurement of the specific heat. I also wish to thank Dr. Iwanade Akio and Dr. Takenouchi Satoshi from the NIMS Materials Analysis Station for the ICP-AES measurements for the determination of the chemical composition.

## **Chapter 4: Thermoelectric Properties of Phase Pure Boron Carbide Prepared by a Solution-Based Method**

### **4.1 Introduction**

In this chapter, the investigation of phase pure boron carbide with a composition of  $B_{4.05}C$  and also commercially available boron carbide powders will be described in detail. Boron carbide is conventionally prepared by carbothermal reduction of boric acid or boron trioxide with carbon, magnesiothermic reduction of boron trioxide or direct reaction of the elements.[156] Depending on the synthesis method, boron carbide powders can contain up to 20 wt.% carbon.[157] Synthesis methods based on gels or solution-based methods are being developed to synthesize boron carbide powders without carbon impurities. In these solution and gel-based synthesis processes organic precursors like mannitol, polymers or citric acid are used to form homogeneous mixtures and the boron carbide is eventually formed after calcination at comparatively low temperatures. [158–160] Using these synthesis methods it is also possible to control the size and shape of the boron carbide particles by adjusting the synthesis conditions accordingly. [161]

Boron carbide has been studied extensively for the use as high temperature thermoelectric materials. Many different synthesis methods have been used for the synthesis including arc melting, sintering, single crystal growth and CVD for the preparation of thin films. [9,42,63,67,69,70,74,162,163] The thermoelectric properties of boron carbide can vary depending on the synthesis technique and composition.[9,63] Therefore, the aim of this study is the comparison of the thermoelectric properties of high purity boron carbide with low amounts of residual carbon with commercially available boron carbide powders. The thermoelectric transport properties of boron carbide are being discussed in detail in this chapter. The boron carbide powder prepared by the solution-based method will be referred to as “High Purity boron carbide” in this chapter.

### **4.2 Experimental**

#### **4.2.1 Synthesis**

The High Purity boron carbide powder was prepared by our collaborators from the Institute for Future Environments (IFE) at the Queensland University of Technology (QUT) by a solution-based method. A short summary of the synthesis process will be given here, the detailed description can be found in the publication by Watts et al.[161]. Sucrose and  $H_3BO_3$  were dissolved in deionized water and stirred at  $80^\circ C$  to form a viscous gel. The gel is then heated under vacuum to remove the residual water. The powder was heated to  $550^\circ C$  as pre-treatment and finally calcined at  $1400^\circ C$ , both under Ar flow.

The commercial boron carbide powders included in this study are Sigma (product number: 101637639), American Elements (product number: BO-C-02M-P.40UM) and Goodfellow (product number: B506010) and will be referred to as Boron Carbide 1, 2 and 3.

#### 4.2.2 Characterization

The raw boron carbide powders were characterized using powder XRD using a diffractometer (PANalytical X'Pert PRO, Bragg-Brentano geometry, Co  $K_{\alpha 1}$  radiation). The phase quantification was performed using FIPB (fixed incidence parallel beam) geometry. [13]

Powder XRD measurements after spark plasma sintering were performed using a diffractometer (Rigaku Smartlab 3, Cu  $K_{\alpha}$  radiation). The sintered samples were pulverized using a  $Si_3N_4$  mortar.

SEM images of the raw powders were taken using a JEOL JSM-7001 FE-SEM. The fracture surface images of the spark plasma sintered samples were taken using a Hitachi S-4800 FE-SEM.

The particle size of the raw boron carbide powders was determined by laser diffraction measurements using a Malvern Masterizer 3000.

#### 4.2.3 Sintering

The spark plasma sintering was performed using a Dr. Sinter SPS apparatus (FUJI ELECTRONIC INDUSTRIAL CO., LTD.). The sintering was carried out using graphite dies ( $\phi = 10$  mm) lined with graphite paper. The temperature during the sintering process was controlled using an optical pyrometer. The samples were heated to 600°C over 5 min by slowly increasing the power output of the SPS instrument and then from 600°C to the final sintering temperature ranging from 1800 – 2000°C at a constant heating rate of 100°C min<sup>-1</sup> under an applied uniaxial pressure of 50 MPa and dynamic vacuum conditions. The samples were kept at the final sintering temperature for 5 – 10 min and then cooled down to room temperature. The pressure was released towards the end of the isothermal step. The sintering conditions for the different samples are listed in Table 4.1 and were determined for each individual boron carbide powder. The large differences in particle size and phase composition caused relatively large differences in the temperatures which were required for optimal densification.

**Table 4.1** Sintering temperatures and holding times (at sintering temperature). [108]

<b>Sample</b>	<b>sintering temperature [°C]</b>	<b>holding time [min]</b>
High Purity	1900	10
Boron Carbide 1	1800	10
Boron Carbide 2	1950	10
Boron Carbide 3	2000	5

The density of the sintered samples was determined by Archimedes' method for samples with a relative density >95% or from the measurement of the sample mass and dimension in the other cases.

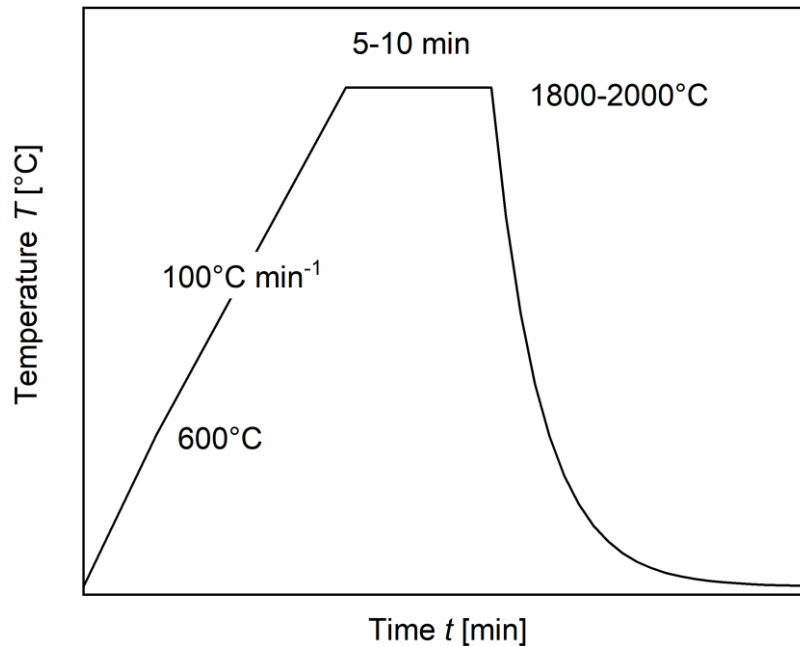


**Figure 4.1** Sintering schedule for boron carbide.

#### 4.2.4 Physical Properties Measurements

The electrical properties of the sintered boron carbide samples were measured quasi-simultaneously using the 4-probe measurement setup of the ZEM-2 (ULVAC-Riko) apparatus. Bar shaped samples of roughly 2 mm x 2 mm x 8 mm were used for these measurements which was performed perpendicular to the pressure-axis of the SPS process.

The specific heat up to 373 K was measured by DSC (Al crucibles on pieces of  $m \approx 30$  mg,  $\text{Al}_2\text{O}_3$  as reference, ISO E1269 - 11(2018)). The thermal diffusivity and relative specific heat were measured using the laser-flash method on a TC-7000 apparatus (ULVAC-Riko) on disk shaped samples ( $\phi \approx 10$  mm,  $h \approx 2$  mm). The specific heat was extrapolated from 373 K to 973 K using the values determined by DSC for 373 K and the relative specific heat measurements by LFA.

Low temperature measurements (10 – 373 K) of electrical resistivity, Seebeck coefficient and thermal conductivity were performed in a PPMS by Quantum Design. Bar shaped samples of roughly 2 mm x 2 mm x 8 mm were contacted with two component silver epoxy in the standard 4-probe configuration for the TTO (Thermal transport option) of the PPMS (Physical properties measurement system, Quantum Design) instrument. Continuous measurements were performed with a heating rate of 0.35 – 0.4 K min<sup>-1</sup>.

## 4.3 Results and Discussion

### 4.3.1 Powder Characterization

The powder XRD patterns for the raw boron carbide powders before SPS are shown in Figure 4.2. The commercial samples show a peak which can be attributed to free carbon (graphite and amorphous carbon) of varying intensity. This peak is absent in the High Purity sample indicating the absence of free carbon.

The relative phase content of the raw powders is summarized in Table 4.2. It was determined by Rietveld refinement of the powder XRD patterns.[13] The primary and secondary phases referred to in Table 4.2 correspond to the averaged peak positions of the phases which were used in the refinement to describe the diffraction pattern. The compositions of were then derived from the compositional dependence of the lattice parameters.[164] Residual refers to non-diffracting material and impurities which corresponds to the “free” carbon in the commercial samples. The relatively high residual value of the High Purity boron carbide has been attributed to the structural model which leads to an overestimation of certain peaks and underestimation of others.

The crystal structure of boron carbide has many defects which can influence its physical properties. [31,32,62,165]

Within the scope of this study only the morphology and composition of the boron carbide phases were considered.

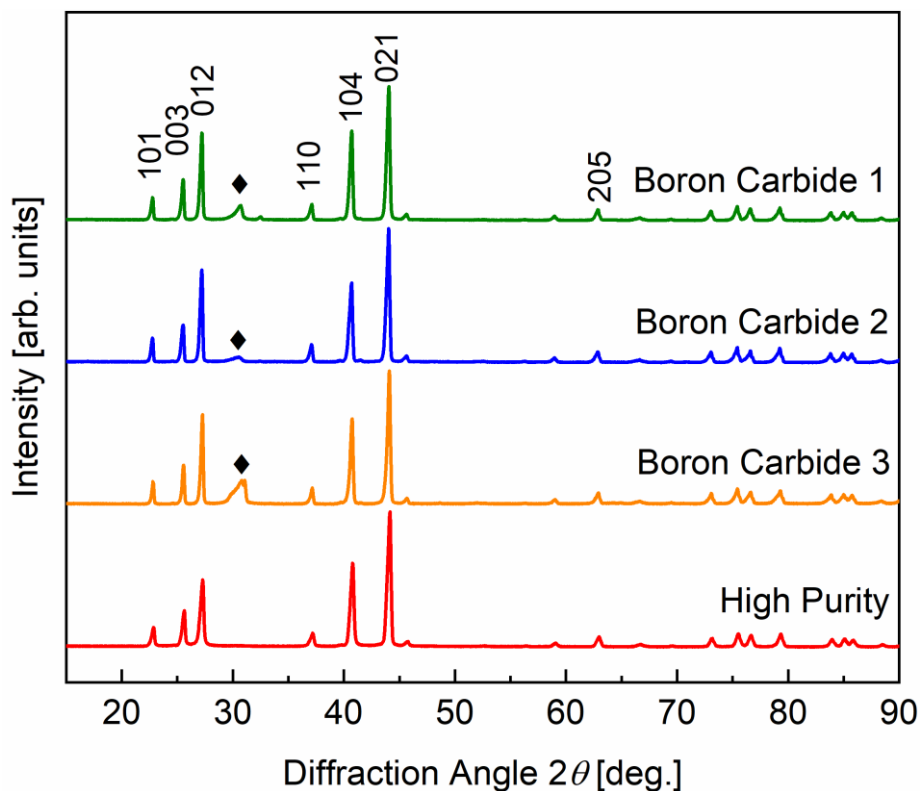


**Figure 4.2** Powder XRD patterns (Co  $K_{\alpha}$  radiation) of boron carbide samples. Key reflections for boron carbide are indexed; ◆ shows the position of free carbon. [108]

**Table 4.2** Phase weight content (wt.%) and corresponding carbon content (at.%) of phases and associated  $R_{wp}$  value for boron carbide samples reproduced from the work of *Watts et al.*[13] [108]

Sample	Primary Phase		Secondary Phase		Residual Phase [wt%]	$R_{wp}$
	Content [wt%]	Carbon	Content [wt%]	Carbon		
		[at%]		[at%]		
High Purity	94.3	19.8 (B <sub>4.05</sub> C)	not present	not present	5.7	8.8
Boron Carbide 1	77.7	19.0 (B <sub>4.26</sub> C)	19.6	14.4 (B <sub>5.95</sub> C)	2.7	5.6
Boron Carbide 2	70.1	19.1 (B <sub>4.23</sub> C)	25.7	13.8 (B <sub>6.25</sub> C)	4.2	6.6
Boron Carbide 3	78.1	19.0 (B <sub>4.26</sub> C)	15.5	14.6 (B <sub>5.85</sub> C)	6.4	6.4

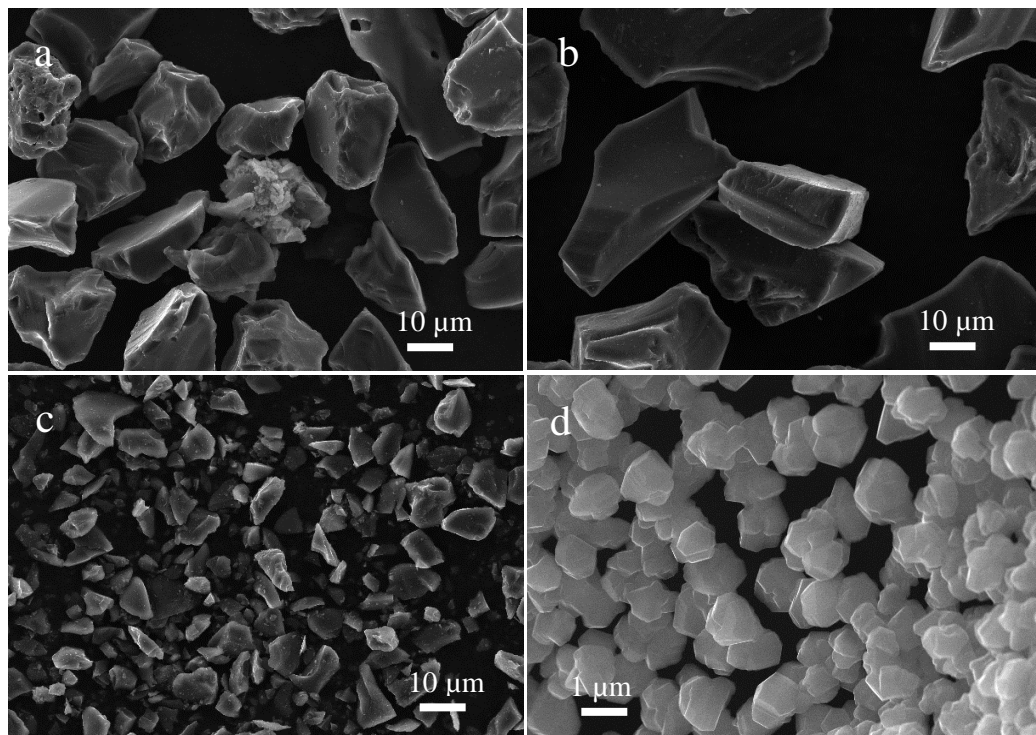


**Figure 4.3** SEM images of boron carbide samples showing significant differences in particle size and morphology. Samples are (a) Boron Carbide 3, (b) Boron Carbide 2, (c) Boron Carbide 1 and (d) High Purity. [108]

The average particle size determined by laser diffraction measurements is shown in Table 4.3. The High Purity boron carbide powder shows overall a smaller particle size than the commercially available powders with at least 10% of the particles with a diameter in the submicron range. The SEM images of the raw boron carbide powders are shown in Figure 4.3. The particle shape of the High Purity boron carbide more regular and closer to a spherical shape due to the solution-based synthesis process. The commercial powders in comparison have a less uniform particle shape and sharper edges which can most likely be attributed to the milling process which was most likely used for the preparation of the powders.

**Table 4.3** Average particle sizes for boron carbide samples. [108]

Sample	$d_{10}$ [ $\mu\text{m}$ ]	$d_{50}$ [ $\mu\text{m}$ ]	$d_{90}$ [ $\mu\text{m}$ ]
High Purity	0.64	4.40	11.1
Boron Carbide 1	2.98	6.52	12.3
Boron Carbide 2	24.80	36.80	54.30
Boron Carbide 3	15.20	23.30	35.30

#### 4.3.2 Characterization After Sintering

The theoretical density of carbon-rich boron carbide of the composition “ $\text{B}_4\text{C}$ ” has been determined as  $\rho = 2.52 \text{ g cm}^{-3}$  and was used for the calculation of the relative densities of the sintered boron carbide samples. [9] The densification behavior showed relatively large differences between the investigated powders. The temperature dependence of the densification of Boron Carbide 3 is shown in Figure 4.4 as an example.

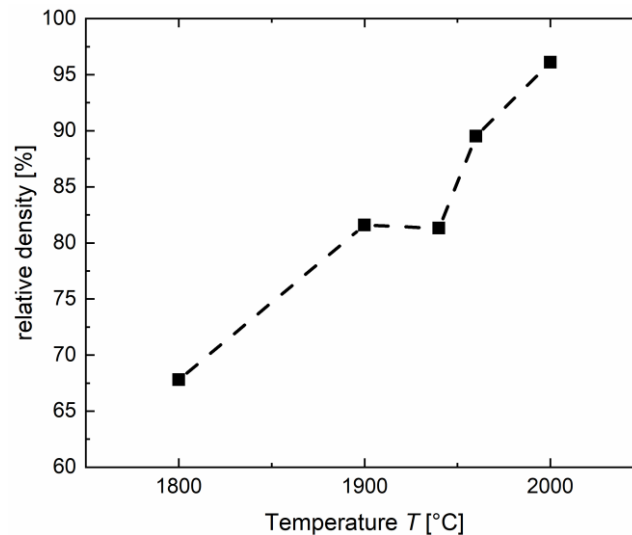


**Figure 4.4** Relative density of the Boron Carbide 3 sintered at different temperatures at 50 MPa applied pressure and holding time of 10 min.

The High Purity boron carbide and Boron Carbide 1 could be densified to close to 100% at comparatively lower temperatures (1900°C and 1800°C for High Purity and Boron Carbide 1 respectively) than Boron Carbide 2 and 3 (1950°C and 2000°C for Boron Carbide 2 and Boron Carbide 3 respectively) which reached relative densities of 88.5% and 96.4% respectively (Table 4.4). Increasing the temperature in the case of Boron Carbide 2 lead to inhomogeneous sintering (lower density at the center) or material being squeezed from the graphite die, likely due to partial melting. The particle size of the High Purity and Boron Carbide 1 samples are overall significantly smaller than Boron Carbide 2 and Boron Carbide 3 as can be seen in Table 4.3. A reduction in particle size generally leads to lower sintering temperatures required to achieve optimal densification. [102]

**Table 4.4** Densities of the sintered boron carbide powder. [108]

Sample	measured density [ $\text{g cm}^{-3}$ ]	relative density [%]
High Purity	2.51	99.6
Boron Carbide 1	2.51	99.6
Boron Carbide 2	2.23	88.5
Boron Carbide 3	2.43	96.4

The powder XRD patterns of the samples after SPS show overall a reduction in the intensity in the peak associated with free carbon compared to the raw boron carbide powders. The samples were crushed and pulverized in a  $\text{Si}_3\text{N}_4$  mortar for the powder XRD measurement and the peaks of  $\text{Si}_3\text{N}_4$  can be seen in the XRD profiles. The full powder XRD pattern is shown in Figure 4.5 and the region from  $2\theta = 20 - 30$  degrees close to the relevant peaks in Figure 4.6. The intensities of these peaks were greatly reduced in the case of the sample Boron Carbide 3 and not present in the sample Boron Carbide 1 after SPS. The sample Boron Carbide 2 shows a sharper carbon peak which could be related to higher crystallinity of the previously present amorphous carbon.

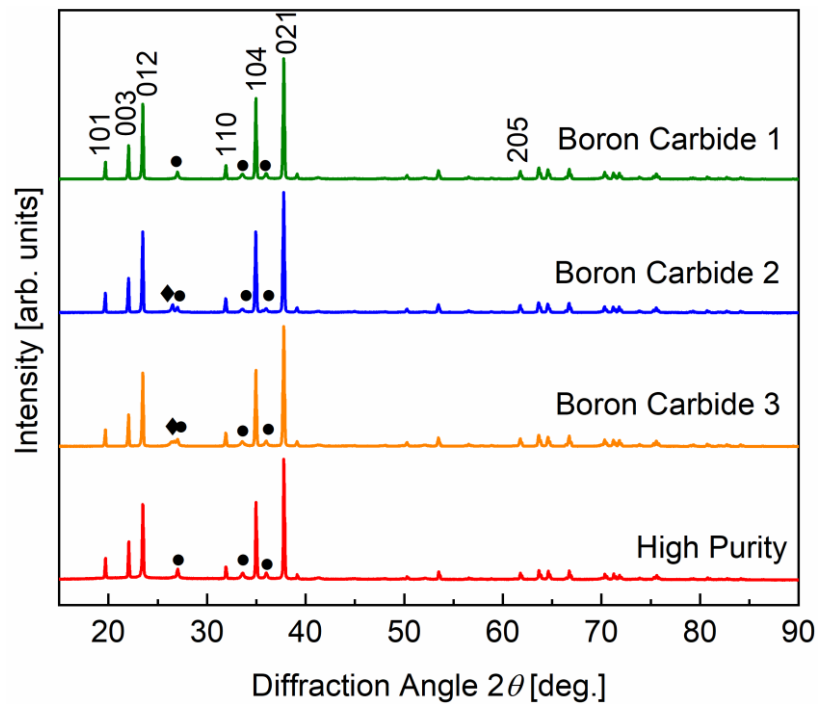


**Figure 4.5** X-Ray diffraction patterns of boron carbide samples after SPS sintering showing a free carbon peak at  $26.5^\circ$  (◆). Additional peaks due to contamination from  $\text{Si}_3\text{N}_4$  (●) mortar during pulverization in preparation for the XRD measurements. [108]

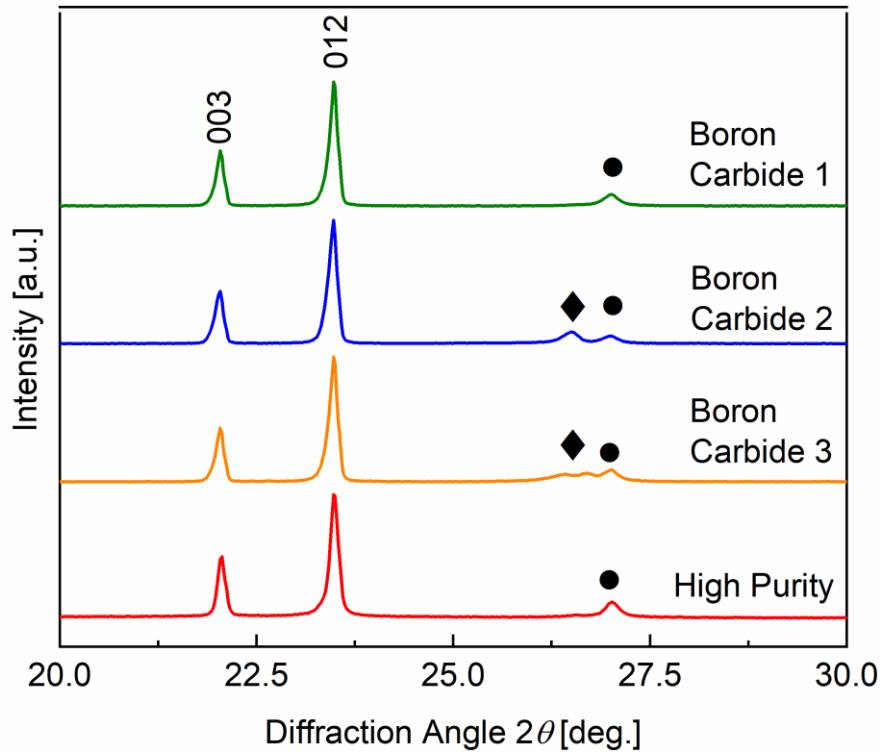


**Figure 4.6** X-Ray diffraction patterns of boron carbide samples after SPS sintering showing a free carbon (◆) peak at 26.5°. Additional peak at 27.0° due to contamination from  $\text{Si}_3\text{N}_4$  (●) mortar during pulverization in preparation for the XRD measurements. [108]

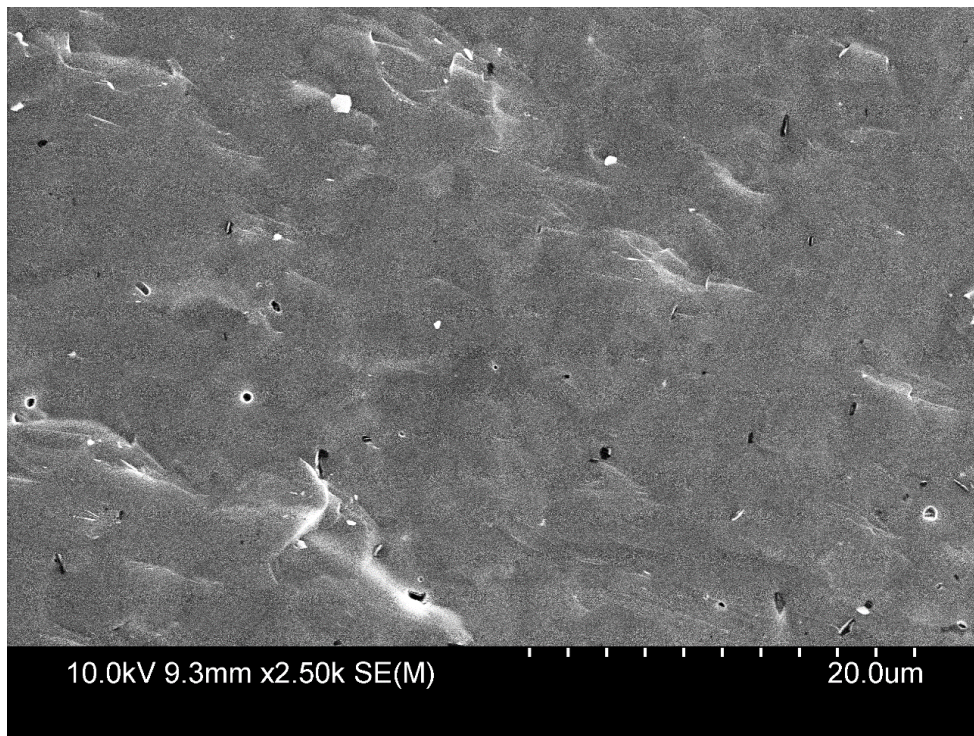


**Figure 4.7** Fracture surface image of the sintered High Purity boron carbide powder showing close to 100% densification. The surface was freshly fractured before the measurement. [108]

A fracture surface SEM image of the sintered High Purity boron carbide is shown in Figure 4.7. Estimating the grain size after SPS is difficult and etching (chemical or thermal) may be required to reveal the microstructure more clearly. The fracture surface image shows close to 100% densification which is consistent with the Archimedes' density measurement.

### 4.3.3 Electrical Properties

The temperature dependence of the electrical resistivity of the boron carbide samples is shown in Figure 4.8. The resistivity decreases with increasing temperatures by roughly 10 times in the temperature range of 373 K to 973 K. The electrical resistivity of the Boron Carbide 2 sample is lower than the other investigated boron carbides despite its overall lower density.

Different models have been used in the past to describe the electrical conduction in boron carbide. One model is based on bipolaron hopping between  $B_{11}C$  icosahedra.[14,64,65] The other model describes the electrical conduction with variable range hopping between localized states and thermally activated band conduction. [15] The electrical properties of the measured boron carbide samples will therefore be described using both of these mechanisms. We also consider the nearest-neighbor hopping mechanism [137] which has an identical temperature dependence for the electrical resistivity as the thermally activated band conduction.

Low temperature measurements ( $10 \leq T \leq 373$  K) of the High Purity boron carbide sample as well as the Boron Carbide 2 sample were performed to help better understand the conduction mechanism. Low temperature measurements of the Boron Carbide 1 and Boron Carbide 3 samples were not carried out due to the similarity of their physical properties to those of the High Purity boron carbide. Due to the increasingly high inner resistance of the samples at low temperature, making accurate determination of the electrical resistivity and Seebeck coefficient difficult, measured values for these physical properties are only available above 30 K and 60 K respectively. The high thermal conductivity also leads to uncertainties in the determination of the Seebeck coefficient and thermal conductivity with increasing temperature, leading to a relatively large scattering of the measurement data.

The temperature dependence of electrical resistivity in Mott's variable range hopping follows

$$\rho = \rho_0 \exp\left(\frac{T_0}{T}\right)^{1/4} \quad (4.1)$$

with  $\rho_0$  and  $T_0$  being the characteristic resistivity and temperatures.[136] It can be seen in Figure 4.9 that the samples follow the VRH temperature dependence well up to a temperature of  $T \approx 200$  K. Deviations of the High Purity sample are most likely due to the increasing contact resistance between the sample and the contacts. Electrical conduction following Mott's VRH at low temperatures has been recently reported for boron carbide nanowires. [166]

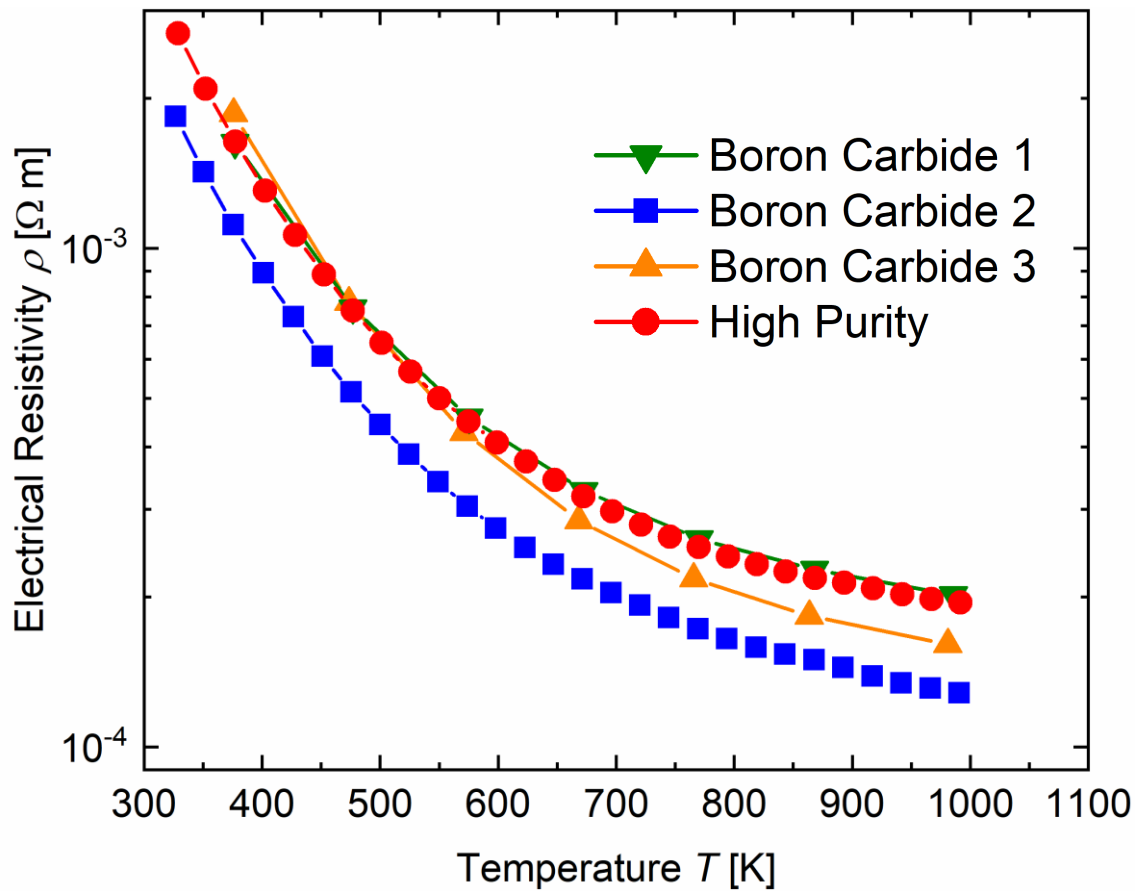


**Figure 4.8** Temperature dependence of the electrical resistivity  $\rho$  of boron carbide samples. [108]

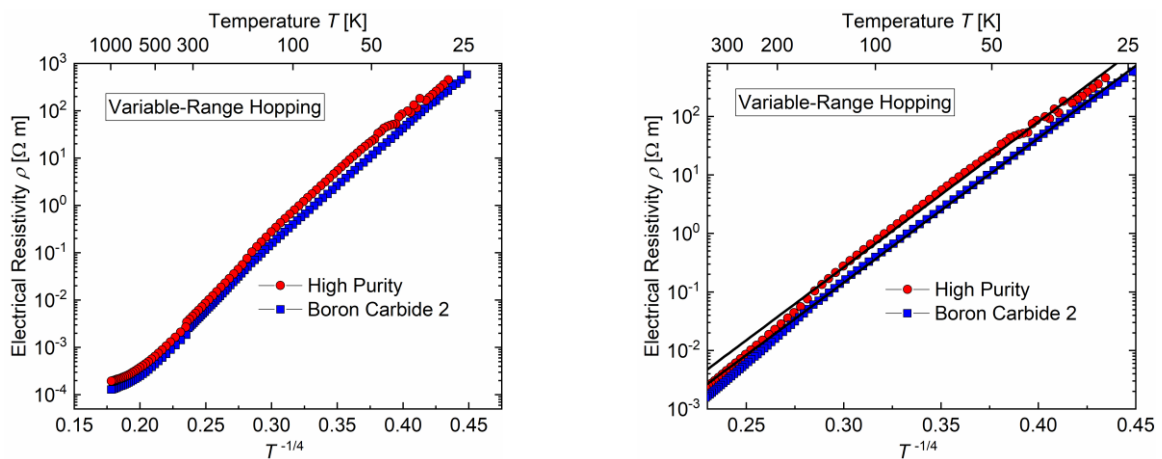


**Figure 4.9** Plot of the electrical resistivity  $\rho$  vs.  $T^{-1/4}$  according to Mott's variable range hopping conduction for the whole temperature range 25 – 973 K (left) and the low temperature range 25 – 300 K (right). The black line indicates the fitting of the resistivity following the VRH conduction mechanism for the samples High Purity and Boron Carbide 2.

The electrical resistivity for the temperature range 323 – 973 K for the High Purity and Boron Carbide 2 samples are shown in Figure 4.10 plotted according to the bipolaron hopping and the thermally activated band conduction / nearest neighbor hopping conduction mechanisms.

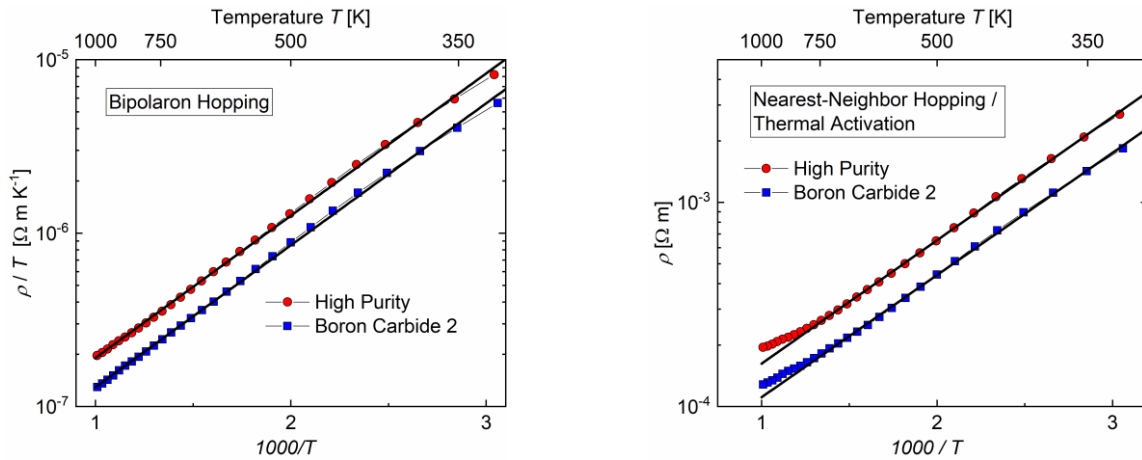


**Figure 4.10** Plot of the electrical resistivity  $\rho / T$  vs.  $1000 / T$  according to the small bipolaron hopping conduction mechanism and electrical resistivity  $\rho$  vs  $1000 / T$  according to Arrhenius-type conduction (thermally activated band conduction or Nearest-Neighbor Hopping conduction) for the samples High Purity and Boron Carbide 2. [108]

The temperature dependence of the electrical resistivity according to bipolaron hopping conduction is given by

$$\rho \propto T \exp\left(\frac{E_h}{kT}\right) \quad (4.2)$$

with  $E_H$  being the hopping activation energy.[14] The electrical resistivity of both High Purity and Boron Carbide 2 follow this temperature dependence well in this temperature range.

Electrical conduction by thermally activated band conduction / nearest neighbor hopping follows

$$\rho \propto \exp\left(\frac{E_A}{kT}\right) \quad (4.3)$$

with  $E_A$  being the activation energy. The agreement of the electrical conduction is similar to the bipolaron hopping mechanism, there is however deviation towards higher temperatures.

As mentioned earlier, the Boron Carbide 2 sample has lower resistivity than the other boron carbide samples investigated. The electrical resistivity of boron carbide depends on the chemical composition and varies with the carbon content of the phase. [9] A minimum in electrical resistivity is found for a carbon content of 13.3 at.% [64] to 13.5 at.% [15] which corresponds to a chemical composition of  $B_{6.5}C$ . [62] Following the bipolaron hopping model, the concentration of bipolaronic holes is at a maximum at this composition. In the TAC model concentration of  $B_{12}$ -icosahedra is at a maximum at the composition of  $B_{6.5}C$  and the concentration of  $B_{11}C$ -

icosahedra at a minimum. At higher carbon concentrations, the carbon acts as an electron donor and compensates the electron deficiency, leading to reduced electronic conduction.

The Boron Carbide 2 powder contained the highest amount of boron-rich boron carbide according to the results of the XRD phase analysis (Table 4.2). This could explain the lower resistivity of this sample despite its lower density compared to the other boron carbide samples.

The hopping/activation energies derived from the fitting of the electrical resistivity are listed in Table 4.5.

**Table 4.5** Activation/Hopping energies for the bipolaron hopping (BPH) and nearest neighbor hopping (NNH)/Thermally activated conduction (TAC). [108]

Sample	$E_H$ (BPH) [eV]	$E_A$ (NNH/TAC) [eV]
High Purity	0.163	0.120
Boron Carbide 2	0.162	0.119

The temperature dependence of the Seebeck coefficients of the boron carbide samples are shown in Figure 4.11. There is a monotonic increase of the Seebeck coefficient up to 300 – 400 K as indicated by the low temperature measurements on the High Purity and Boron Carbide 2 samples. In the temperature range 323 – 973 K the Seebeck coefficient of all samples shows only small changes with temperature and ranges from roughly 225 – 280  $\mu\text{V.K}^{-1}$ .

For compounds following variable-range hopping conduction mechanism, the temperature dependence of Seebeck coefficient can be described in the following way [140]:

$$\alpha \approx -\frac{k}{e} \left( \frac{\pi - 2}{\pi} k\sqrt{TT_0} + \frac{2\pi}{3} kT \right) \left( \frac{d \ln N(E)}{dE} \right)_{E=E_F} \quad (4.4)$$

for values of the characteristic temperature  $T_0 > 10^4$  K the  $T^{0.5}$  term is dominant ( $T_0 = 1.08 \times 10^7$  K and  $1.05 \times 10^7$  K for the High Purity and Boron Carbide 2 samples respectively) which is shown by fitting the temperature dependence of the Seebeck coefficient in the temperature range of 60 – 373 K in Figure 4.11 with  $\alpha \propto T^{0.5}$ . Despite the large scattering of the measured values the measurements agree overall with the temperature dependence of the VRH model.

The Seebeck coefficient for polaron hopping is expected to be independent of the temperature in the high temperature limit.[167] Small negative temperature dependencies have been observed for boron carbide in previous studies. This has been attributed to the presence of conductive carbon inclusions which can lead to a short-circuiting and reduce the Seebeck coefficient. [65] This agrees with the temperature dependence of the Seebeck coefficient in this study with the Seebeck coefficient of the sample Boron Carbide 2 decreasing with

increasing temperature. Boron Carbide 2 also had the highest intensity of peaks corresponding to free carbon in the powder XRD patterns after SPS among the investigated samples.

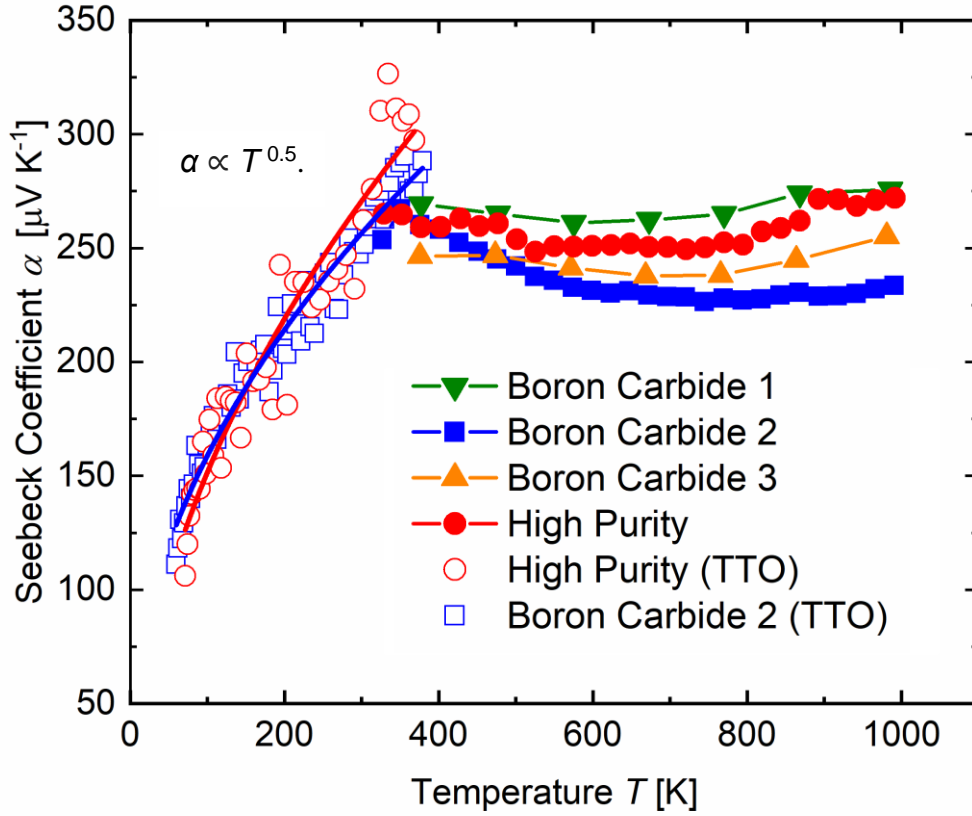


**Figure 4.11** Temperature dependence of the Seebeck coefficient  $\alpha$  of boron carbide samples. [108]

The temperature dependence of the Seebeck coefficient of the other samples, that is High Purity, Boron Carbide 1 and Boron Carbide 3 appear to show a very broad minimum in the measured temperature range of 323 – 973 K.

For nearest neighbor hopping the Seebeck coefficient is expected to follow [140]

$$\alpha \approx -\frac{k}{e} \left( \frac{\pi - 2 E_A^2}{\pi kT} + \frac{2\pi}{3} kT \right) \left( \frac{d \ln N(E)}{dE} \right)_{E=E_F} \quad (4.5)$$

using the value for  $E_A$  (or  $\varepsilon_3$  as used by Sir Nevill Mott and other authors[137,140]) from the fitting of the electrical resistivity (Figure 4.10 and Table 4.6) the minimum temperature

$$T_{min} = E_A \sqrt{\frac{3(\pi - 2)}{2\pi^2}} \quad (4.6)$$

$T_{min} = 579.7$  K and  $T_{min} = 574.5$  K for the High Purity and Boron Carbide 2 samples respectively can be calculated. This agrees fairly well with the measured Seebeck coefficient of the High Purity boron carbide. The Seebeck coefficient of the Boron Carbide 2 sample decreases slightly with increasing temperature. As previously mentioned, this could be attributed to the presence of conductive carbon inclusions in the sample.

The electronic properties of the boron carbide samples measured in this investigation can be described by the variable range hopping mechanism at temperatures  $T \leq 200$  K and by the nearest neighbor hopping mechanism for temperatures  $323$  K  $\leq T \leq 750$  K. This is a behavior that is also largely observed in disordered solids such as amorphous materials.[136] The electrical resistivity at higher temperatures is deviating from these conduction mechanisms, the origin of this deviation will require additional clarification. The bipolaron hopping model describes the electrical conduction at elevated temperatures well. However, the possibility of the existence of bipolarons in boron carbide has been questioned. This is based on low Raman intensities (lattice polarizability is responsible both for the formation of polarons as well as Raman scattering intensity), small electron-phonon coupling constants and effective mass for holes comparable to the band mass (polarons are expected to have high effective mass). [15]

The temperature dependence of the power factor  $pf = \alpha^2 \rho^{-1}$  is shown in Figure 4.12. The power factor increases steadily for all boron carbide samples and reaches values around  $0.4$  mW m<sup>-1</sup> K<sup>-2</sup> close to 1000 K.

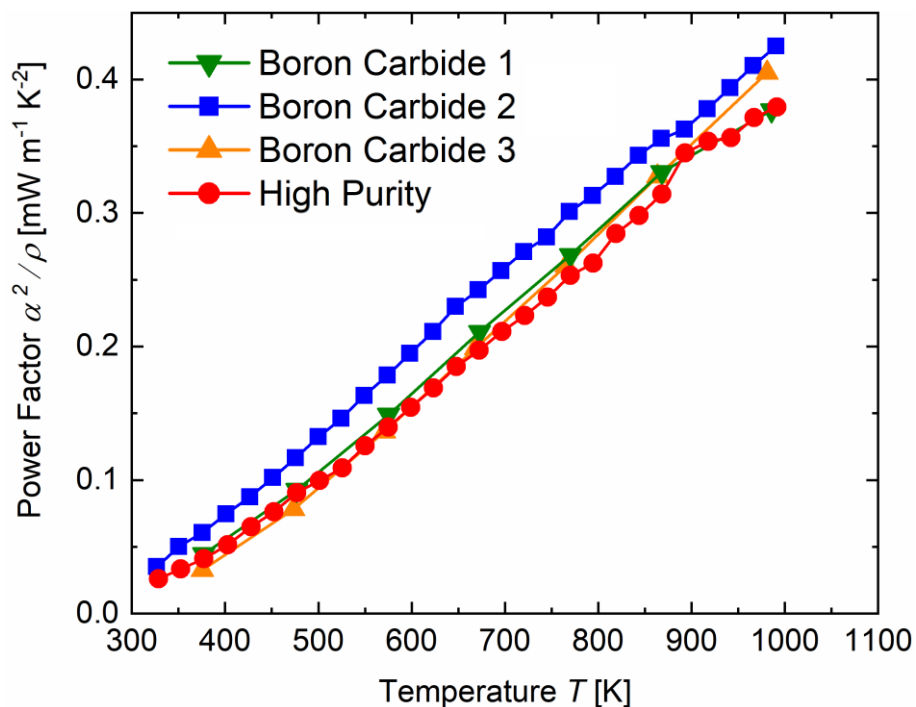


**Figure 4.12** Temperature dependence of the power factor  $pf = \alpha^2/\rho$  of boron carbide samples. [108]

#### 4.3.4 Thermal Properties

The thermal conductivity  $\kappa$  in the temperature range 373 – 973 K is calculated from  $\kappa = \rho D C_p$  is shown in Figure 4.13. The High Purity as well as the Boron Carbide 1 and Boron Carbide 3 samples have high thermal conductivity values of roughly 20 W m<sup>-1</sup> K<sup>-1</sup> at 373K which decrease with increasing temperatures to 12 – 15 W m<sup>-1</sup> K<sup>-1</sup> at 973 K. The Boron Carbide 2 sample on the other hand has a significantly reduced thermal conductivity, especially at lower temperatures around 373 K.

It has been shown that the composition has a large influence on the thermal conductivity of boron carbide. The thermal conductivity is the highest for carbon-rich boron carbides with a composition close to B<sub>4</sub>C and decreases with increasing boron content.[9,168] This has been explained through the higher prevalence of C-B-C chains linking B<sub>12</sub> icosahedra in the structure in carbon-rich boron carbide as mentioned previously in Chapter 1. This causes carbon-rich boron carbide to behave more like crystalline solid while boron-rich boron carbide is more disordered. [168]

Since the Boron Carbide 2 sample with the lower thermal conductivity also has a lower relative density than the other investigated samples it is necessary to estimate the influence of the porosity on the thermal conductivity. For low values of porosity (<15%) a simple model like the Maxwell-Eucken model [169] can be used

$$\frac{\kappa_{eff}}{\kappa_B} = \frac{\kappa_P + 2\kappa_B + 2 v_P(\kappa_P - \kappa_B)}{\kappa_P + 2\kappa_B - v_P(\kappa_P - \kappa_B)} \approx \frac{1 - v_P}{1 + \frac{1}{2} v_P} \quad (4.7)$$

with  $\kappa_{eff}$ ,  $\kappa_B$ ,  $\kappa_P$  and  $v_P$  being the effective thermal conductivity, the bulk thermal conductivity, the pore thermal conductivity and the pore volume fraction respectively. Since  $\kappa_B \gg \kappa_P$  the thermal conductivity of the pores can be neglected as an approximation. The simplified equation gives a reduction in thermal conductivity of less than 20% for a pore volume fraction  $v_p = 11.5$ .

The reduction in thermal conductivity is therefore expected to be not due to porosity alone but additional factors like the composition need to be considered as well. As mentioned in the discussion of the electrical properties, the results of the thermal conductivity measurement agree with the XRD phase analysis summarized in Table 4.2. The High Purity, Boron Carbide 1 and Boron Carbide 3 have thermal conductivities comparable to carbon-rich boron carbides reported in earlier investigations while the Boron Carbide 2 has a thermal conductivity closer to boron-rich boron carbide.

The low temperature TTO measurements of the thermal conductivity show typical behavior for disordered materials.[37] The measurements also agree fairly well with the high temperature LFA results.

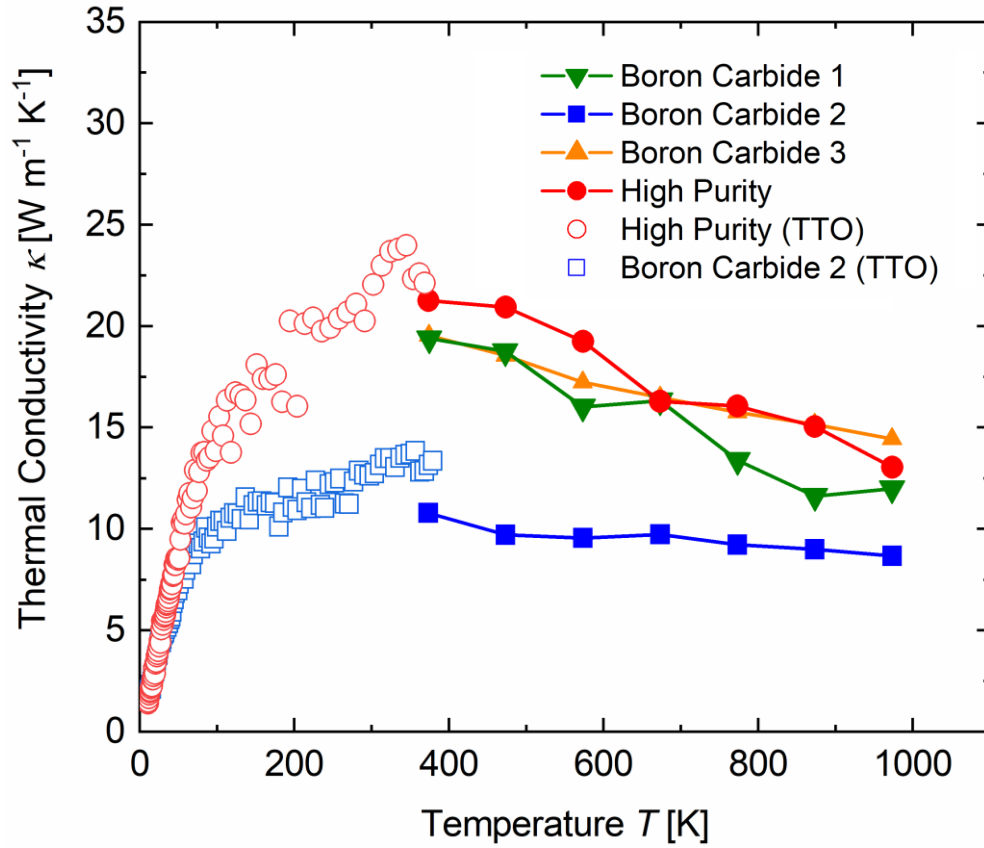


Figure 4.13 Temperature dependence of the thermal conductivity  $\kappa$  of boron carbide samples. [108]

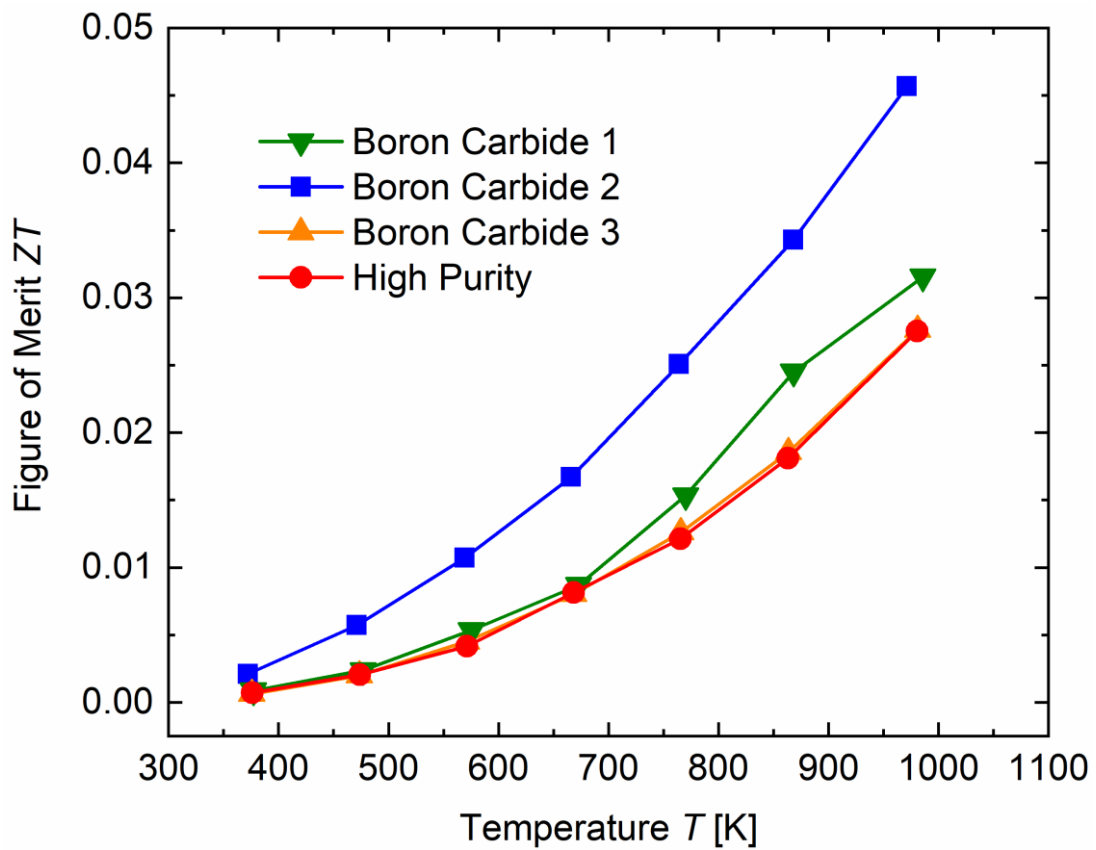


Figure 4.14 Temperature dependence of the figure of merit  $ZT$  of boron carbide samples. [108]

### 4.3.5 Figure of Merit

The temperature dependence of the figure of merit  $ZT$  can be seen in Figure 4.14 for 373 – 973 K.  $ZT$  increases monotonously with increasing temperature up to values of 0.027 – 0.046 at 973 K. The highest values were observed for the Boron Carbide 2 sample while the High Purity, Boron Carbide 1 and Boron Carbide 3 samples have lower and very similar values throughout the whole temperature range. This difference can be attributed to the higher content (25.7 wt.% for Boron Carbide 2 compared to 19.6 wt.% and 15.5 wt.% for Boron Carbide 1 and Boron Carbide 3 respectively) of boron-rich secondary phase ( $B_{6.25}C$  for Boron Carbide 2 compared to  $B_{5.95}C$  and  $B_{5.85}C$  for Boron Carbide 1 and Boron Carbide 3 respectively) of the Boron Carbide 2 powder compared to the other investigated samples. This agrees well with previous reports on the dependence of the thermoelectric performance on the chemical composition. [9]

### 4.4 Conclusion

In this chapter, the study of the thermoelectric properties of boron carbide has been described. For this purpose, a phase pure boron carbide sample synthesized by a solution-based method as well as commercially available boron carbide powders were analyzed and densified using spark plasma sintering. All samples showed similar thermoelectric properties with the exception of the Boron Carbide 2 sample. The interpretation of the thermoelectric properties showed in agreement with the XRD phase analysis that higher contents of boron-rich boron carbide phase is responsible for the overall higher thermoelectric performance of this sample.

In addition, the electrical transport in boron carbide was discussed by applying and comparing different transport mechanisms including bipolaron hopping, variable range hopping, nearest neighbor hopping and thermally activated band conduction. Our results show temperature dependences of the electrical resistivity and Seebeck coefficient at  $T \leq 200$  K corresponding to the variable-range hopping mechanism. The bipolaron hopping conduction agreed overall well with the temperature dependencies of the electrical resistivity and Seebeck coefficient at temperatures  $T \geq 323$  K. The nearest-neighbor hopping mechanism describes the temperature dependence of the electrical resistivity well with small deviations at high temperatures of  $T > 750$  K. Broad minima were observed in the temperature dependence of the Seebeck coefficient which matches the predictions of the nearest-neighbor hopping well. Nearest-neighbor hopping may therefore be a good model to describe the electrical conduction mechanism in boron carbide.

While the thermoelectric properties of the boron carbide prepared by a solution-based process were not an improvement over commercial boron carbide powders, it showed good sintering behavior thanks to the uniform particle shape and defined composition. This makes it an attractive material for further investigation. Using this synthesis method, boron carbide of the composition  $B_{6.5}C$  should be prepared to improve the thermoelectric performance.

#### 4.5 Acknowledgements

The contents of this chapter have been published as “P. Sauerschnig, J.L. Watts, J.B. Vaney, P.C. Talbot, J.A. Alarco, I.D.R. Mackinnon, and T. Mori, Thermoelectric properties of phase pure boron carbide prepared by a solution-based method, *Advances in Applied Ceramics* 119:2 (2020) 97-106” and have been modified for this thesis.

I wish to thank Dr. J. Watts for the synthesis of the High Purity boron carbide powder and characterization of the raw boron carbide powders by X-Ray diffraction, SEM and laser diffraction analysis.

## **Chapter 5: Study of Seebeck Enhancement by Spin Fluctuation in Ferromagnetic $\text{Fe}_2\text{V}_{1-x}\text{M}_x\text{Al}_{1-y}$ (M=Mn, Co) Full Heusler Alloys**

### **5.1 Introduction**

In this chapter the investigation of  $\text{Fe}_2\text{VAl}$  Full Heusler alloys as low temperature thermoelectric materials is described. The Heusler alloy  $\text{Fe}_2\text{VAl}$  is an attractive candidate for this temperature range due to its high power factor  $pf = \alpha^2 \rho^{-1}$  which can reach values exceeding  $5 \text{ mW m}^{-1} \text{ K}^{-2}$  which is comparable to bismuth telluride which is currently being used in commercial thermoelectric modules. [81,88]

Recently it has been shown by Tsujii et al. that the Seebeck coefficient in weakly ferromagnetic doped  $\text{Fe}_2\text{VAl}$  can be enhanced through the contribution of spin fluctuations.[16] Spin fluctuations occur in weak itinerant electron ferromagnets [170] and cause a drag of conduction electrons which is responsible for the enhanced Seebeck coefficient. [16,171] A power factor of  $1.2 \text{ mW m}^{-1} \text{ K}^{-2}$  was reported for  $\text{Fe}_{2.2}\text{V}_{0.8}\text{Al}_{0.6}\text{Si}_{0.4}$  at 300 K with a Curie-Weiss temperature of 292 K. [16] It was estimated that up to 50% enhancement of the Seebeck coefficient could be due to contributions from spin fluctuations.

Based on these results we try to develop  $\text{Fe}_2\text{VAl}$  Full Heusler alloys with good thermoelectric performance at room temperature. Stoichiometric  $\text{Fe}_2\text{VAl}$  is non-magnetic [172], so a series of  $\text{Fe}_2\text{V}_{(1-x)}\text{M}_x\text{Al}$  (M = Co, Mn;  $x = 0.1 - 0.3$ ) was prepared in order to obtain ferromagnetic materials with a Curie-Weiss temperature close to 300 K as it has been shown that the spin fluctuation enhancement of the Seebeck coefficient has a maximum at this temperature.[16]

### **5.2 Experimental**

Stoichiometric amounts ( $m \sim 5\text{g}$  for each sample) of Fe (99.9%), V (99.9%), Al (99.999%), Mn (99.9%) and Co (99.9%) for  $\text{Fe}_2\text{V}_{1-x}(\text{Co},\text{Mn})_x\text{Al}$  ( $x = 0.1, 0.2, 0.3$ ) were weighed and arc melted under Ti-gettered Ar atmosphere. An arc furnace with a water-cooled Cu plate and a W-electrode were used. The samples were flipped and re-melted 4-5 times to ensure homogeneity. The melted ingots were annealed in evacuated quartz tubes in Ta-foil capsules at 1173 K for 7 days and slow-cooled to room temperature.

The annealed samples were hand milled using a tungsten carbide mortar and subsequently ball milled in a planetary ball mill (Fritsch Pulverisette) in a tungsten carbide jar with tungsten carbide balls under Ar atmosphere for 4h at 300 rpm. The powders were then consolidated into dense cylinders using spark plasma sintering using a Dr. Sinter SPS apparatus (FUJI ELECTRONIC INDUSTRIAL CO., LTD.). Graphite dies of inner diameter  $\phi = 10 \text{ mm}$  lined with graphite paper and graphite punches were used. The sintering was performed under dynamic vacuum ( $<4 \text{ Pa}$ ) with an applied uniaxial pressure of 40 MPa. The temperature was controlled using an optical pyrometer. The sintering schedules included a heating step to  $600^\circ\text{C}$  over 10 min

followed by a heating step at a heating rate of  $50^{\circ}\text{C min}^{-1}$  to the final sintering temperature of  $900^{\circ}\text{C}$  where it was kept for 30 min before cooling down to room temperature afterwards.

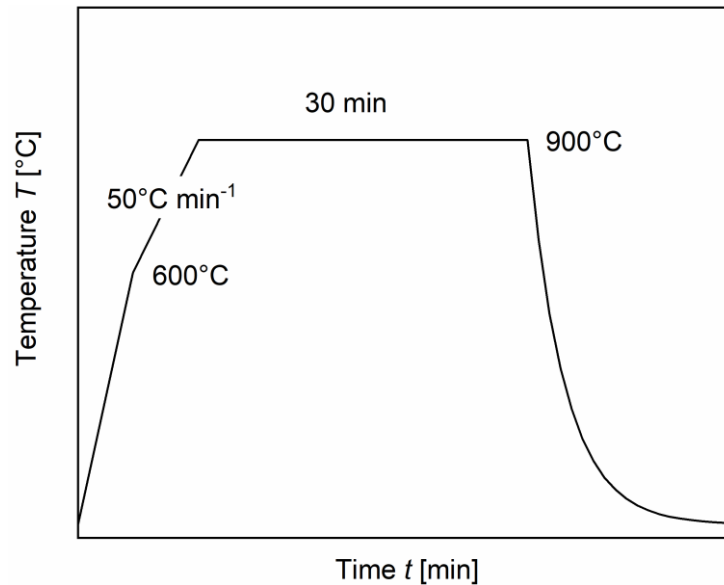


**Figure 5.1** Sintering schedule for Full Heusler  $\text{Fe}_2\text{V}_{1-x}(\text{Co},\text{Mn})_x\text{Al}$ .

The sintered samples were characterized by XRD measurements for phase identification. Quantitative analysis was performed by WDX-EPMA SEM measurements.

The magnetic properties were measured using a MPMS (Quantum Design) instrument utilizing a SQUID magnetometer. Magnetic susceptibility measurements were performed in a temperature range of 2 – 325 K at applied magnetic fields of 0.1 – 10 kOe. Magnetization measurements were carried out at temperatures of 5, 100, 200 and 300 K with applied magnetic fields up to 70 kOe.

The thermoelectric transport properties (Seebeck coefficient, electrical resistivity and thermal conductivity) were measured using a PPMS instrument (Quantum Design) in a temperature range of 10 – 373 K under applied magnetic fields of 0 and 90 kOe using the TTO option. The electrical current, temperature gradient and magnetic field were all applied in the same directions. Continuous measurements were performed with a heating rate of  $0.35 - 0.4 \text{ K min}^{-1}$ .

Additional measurements of the electrical resistivity were performed using the ACT option of the PPMS instrument due to large scatter in the resistivity data measurement under the applied magnetic field ( $H = 90 \text{ kOe}$ ) in the TTO measurement. The ACT measurement setup is shown in Figure 5.2. This setup was used for applying the magnetic field parallel to the electrical current.

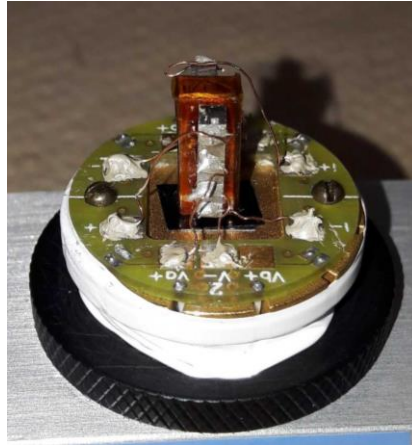


**Figure 5.2** ACT electrical resistivity measurement setup. A copper block (high thermal conductivity for even temperature distribution in the sample) is wrapped in Kapton tape for electrical insulation. Short copper wires are attached to the samples with two-component silver paste and connected to the contacts of the ACT sample puck.

### 5.3 Results and Discussion

#### 5.3.1 Characterization

The XRD patterns shown in Figure 5.3 were taken on the polished surface of the sintered samples. The mechanical stress upon grinding in the mortar to pulverize the sample could induce disorder in the ordered L2<sub>1</sub> structure. [79]

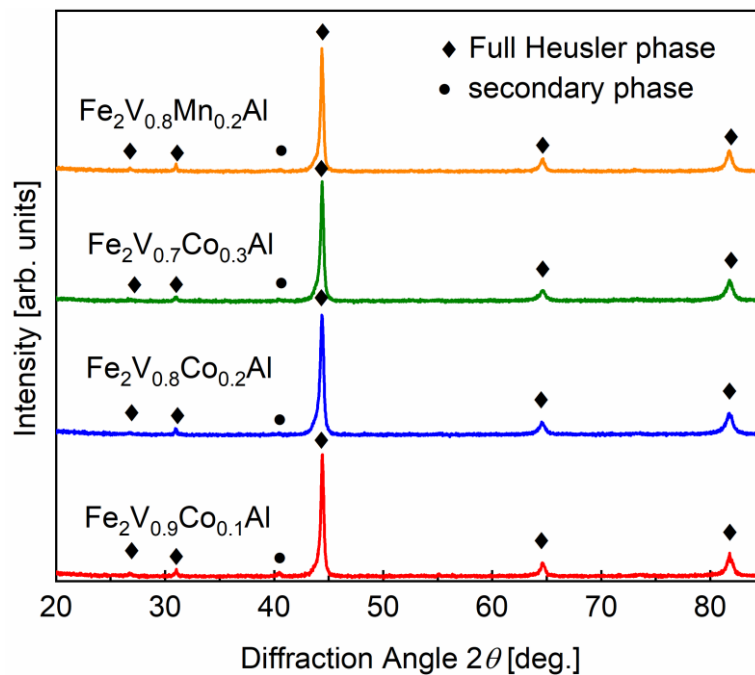


**Figure 5.3** XRD patterns of the samples  $\text{Fe}_2\text{V}_{1-x}\text{Co}_x\text{Al}$  and  $\text{Fe}_2\text{V}_{0.8}\text{Mn}_{0.2}\text{Al}$  after spark plasma sintering at 900 °C using Cu K $\alpha$  radiation.

All samples in Figure 5.3 showed the ordered  $L2_1$  structure for the Full Heusler phase. The XRD patterns show only small amounts of impurities which were identified as aluminium oxide and tungsten carbide.

The WDX-EPMA SEM analysis (Table 5.1) shows that Co and Mn were successfully introduced into the structure. The quantitative analyses of the Full Heusler main phases show a slight deficiency in Al and a slightly higher V content. Whether the latter is due to matrix effects or an actual increase in the V content in the course of the sample preparation remains to be determined. The transport properties of  $\text{Fe}_2\text{VAl}$  are very sensitive to off-stoichiometry [82,90,173], therefore we are currently investigating the effects of off-stoichiometry in the samples with V/Co substitution in the series  $\text{Fe}_2\text{V}_{0.9}\text{Co}_{0.1}\text{Al}_{1\pm x}$  on the magnetic and thermoelectric properties. The Mn doped samples showed a deficiency in Mn compared to the nominal composition. This corresponds well to higher weight losses ( $\sim 2$  wt.%) observed during the arc melting process. A new series of samples with Mn substitution  $\text{Fe}_2\text{V}_{1-x}\text{Mn}_x\text{Al}$  has been prepared and weight losses during arc melting have been kept below 0.7 wt.% for all samples, thus ensuring only small deviations from the nominal composition.

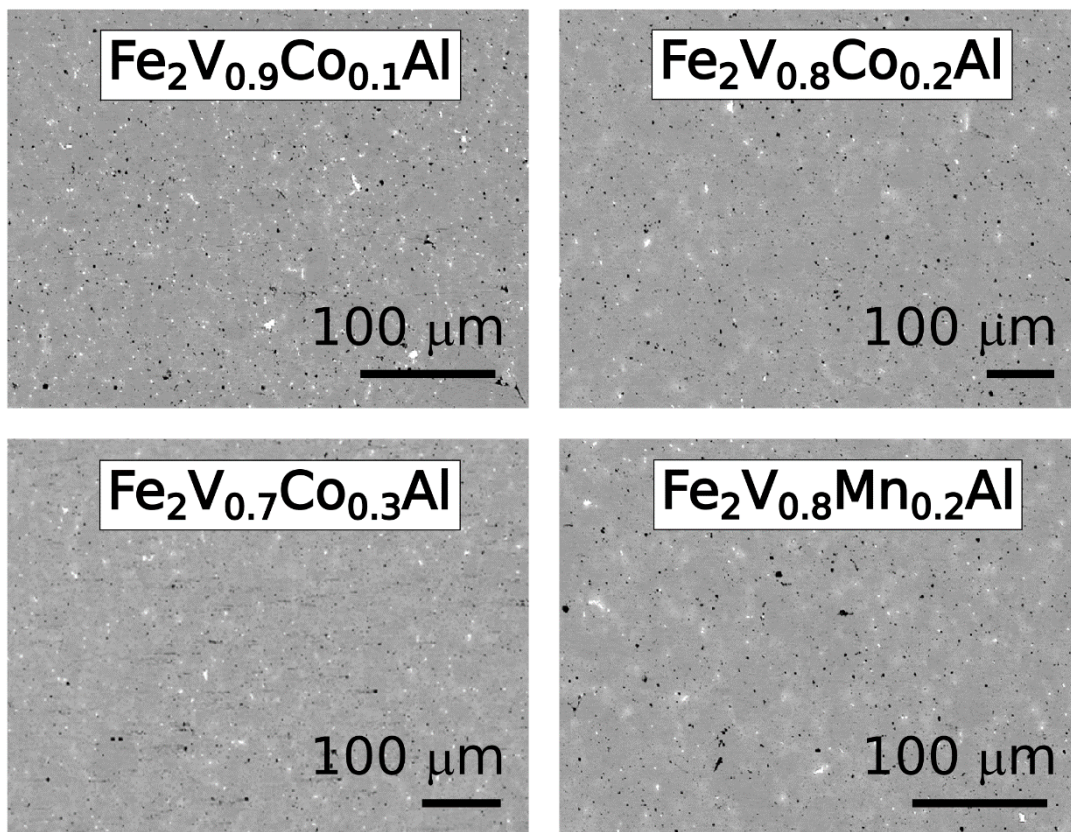


**Figure 5.4** SEM micrographs (BSE detector) of the samples  $\text{Fe}_2\text{V}_{1-x}\text{Co}_x\text{Al}$  and  $\text{Fe}_2\text{V}_{0.8}\text{Mn}_{0.2}\text{Al}$  (grey) after spark plasma sintering at 900 °C. The samples contain WC impurities (white) due to contamination from the jar and balls during the ball milling and  $\text{Al}_2\text{O}_3$  and small pores (black).

**Table 5.1** WDX-EPMA SEM analysis of the samples  $\text{Fe}_2\text{V}_{1-x}\text{Co}_x\text{Al}$  and  $\text{Fe}_2\text{V}_{0.8}\text{Mn}_{0.2}\text{Al}$  after spark plasma sintering at 900 °C.

Nominal composition	Measured composition
$\text{Fe}_2\text{V}_{0.9}\text{Co}_{0.1}\text{Al}$	$\text{Fe}_2\text{V}_{1.052}\text{Co}_{0.103}\text{Al}_{0.942}$
$\text{Fe}_2\text{V}_{0.8}\text{Co}_{0.2}\text{Al}$	$\text{Fe}_2\text{V}_{0.936}\text{Co}_{0.204}\text{Al}_{0.945}$
$\text{Fe}_2\text{V}_{0.7}\text{Co}_{0.3}\text{Al}$	$\text{Fe}_2\text{V}_{0.827}\text{Co}_{0.304}\text{Al}_{0.948}$
$\text{Fe}_2\text{V}_{0.8}\text{Mn}_{0.2}\text{Al}$	$\text{Fe}_2\text{V}_{0.875}\text{Mn}_{0.118}\text{Al}_{0.942}$

### 5.3.2 Magnetic Properties

Stoichiometric  $\text{Fe}_2\text{VAl}$  has a non-magnetic ground state. [172] Upon substitution of V with Co we see ferromagnetic behavior. Due to the loss of Mn in the arc melting process described in Section 5.3.1 only the magnetic properties of the Co doped samples have been investigated in detail so far.

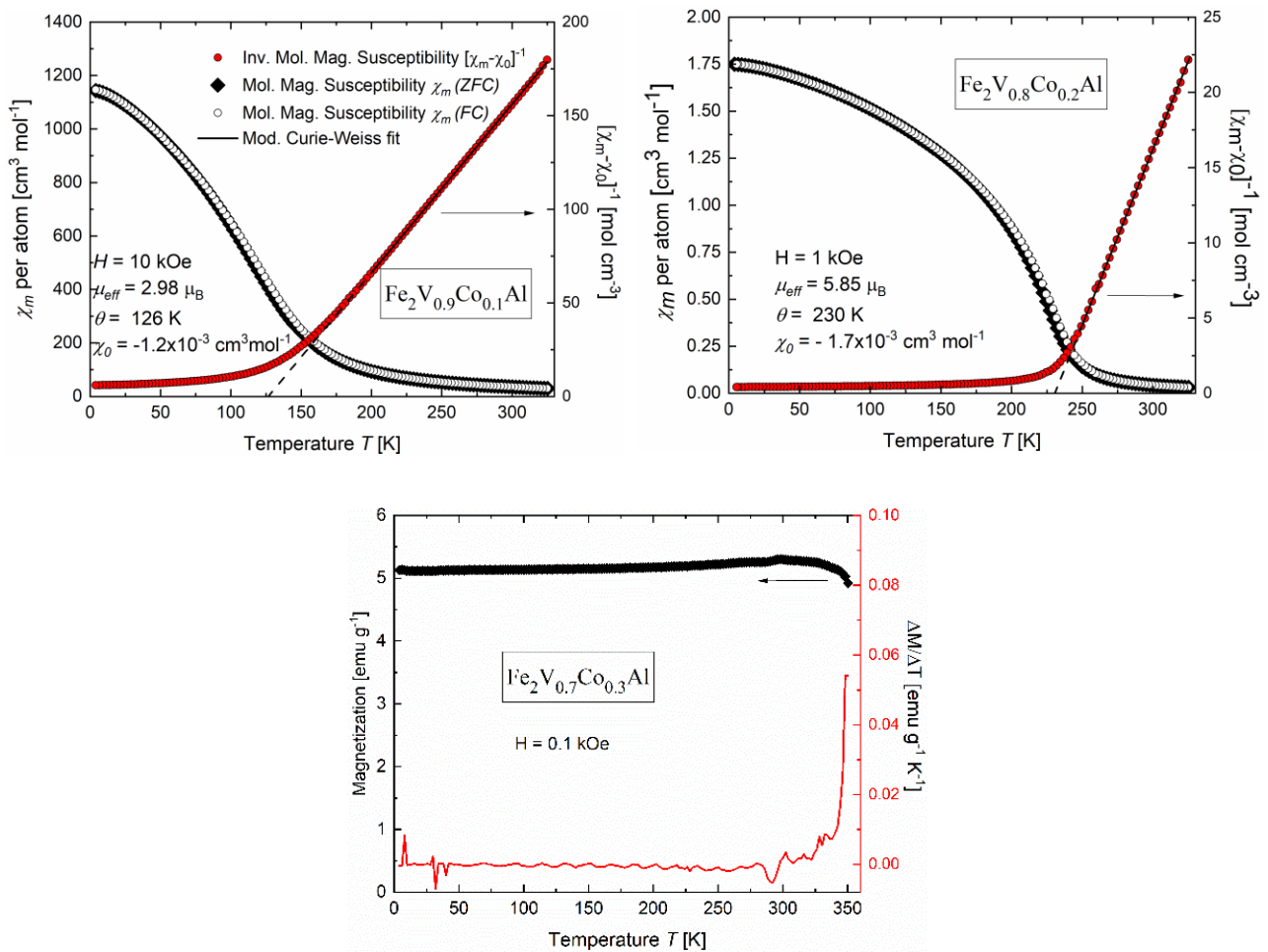


**Figure 5.5** Temperature dependence of the magnetic susceptibility/magnetization of the samples  $\text{Fe}_2\text{V}_{1-x}\text{Co}_x\text{Al}$ .

The temperature dependence of the magnetic susceptibility / magnetization in Figure 5.5 for the samples  $\text{Fe}_2\text{V}_{1-x}\text{Co}_x\text{Al}$  shows an increase in the Curie temperature  $\theta$  and the effective magnetic moment  $\mu_{\text{eff}}$  with increasing Co content. The Curie temperature of the sample  $\text{Fe}_2\text{V}_{0.7}\text{Co}_{0.3}\text{Al}$  appears to lie just outside the temperature range of the MPMS instrument as can be seen from the  $\Delta M/\Delta T$  vs.  $T$  plot.

The magnetic field dependence of the magnetization  $M$  is plotted in Figure 5.6. The saturation magnetization increases with increasing Co content with overall relatively low values of 0.3 – 0.7  $\mu_B$  per Co and Fe atom.

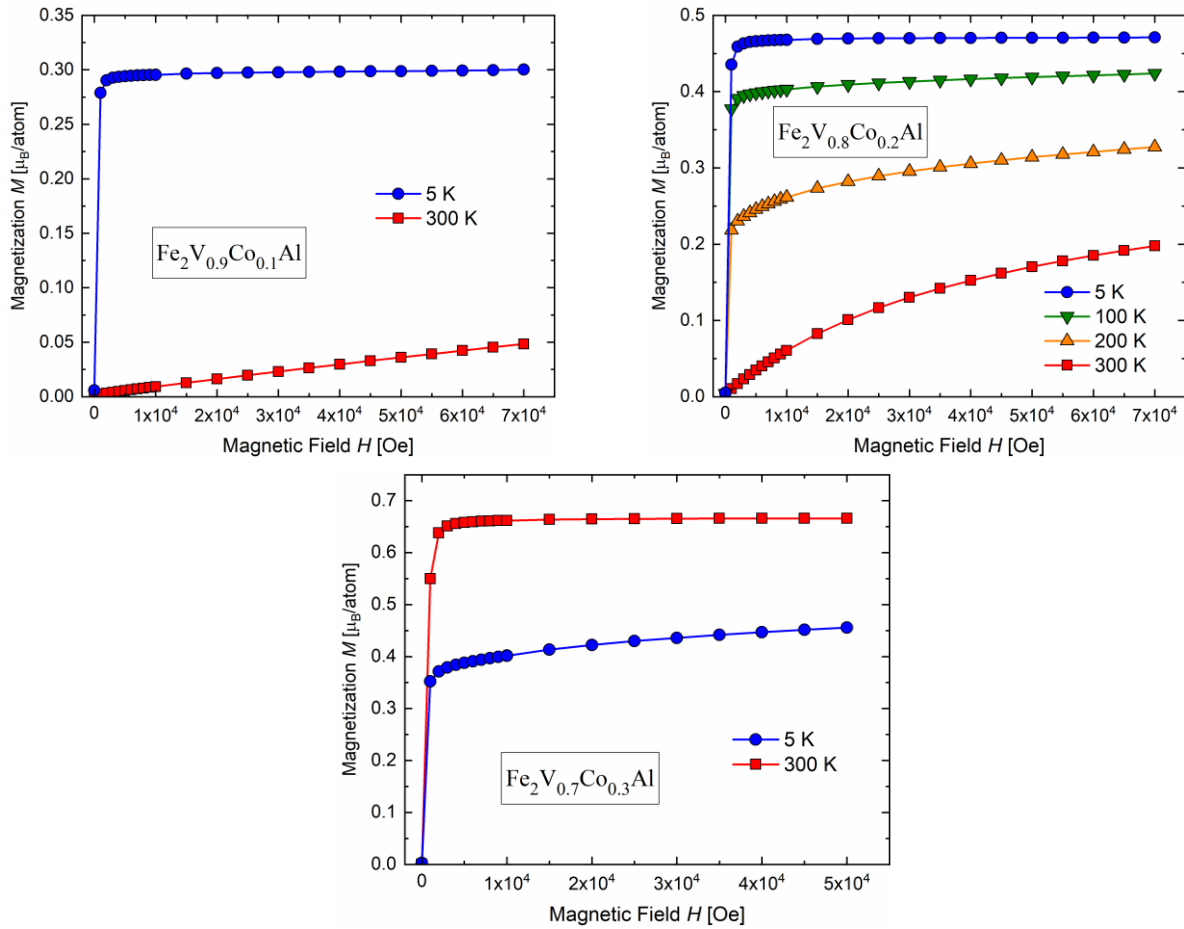


**Figure 5.6** Magnetic field dependence of the magnetization of the samples  $\text{Fe}_2\text{V}_{1-x}\text{Co}_x\text{Al}$  at 5 – 300 K.

### 5.3.3 Thermoelectric Properties

The thermoelectric properties of the samples  $\text{Fe}_2\text{V}_{1-x}\text{Co}_x\text{Al}$  and  $\text{Fe}_2\text{V}_{0.8}\text{Mn}_{0.2}\text{Al}$  are shown in Figure 5.7. Undoped, stoichiometric  $\text{Fe}_2\text{VAl}$  is a p-type semiconductor-like behavior with a room temperature Seebeck coefficient of roughly  $25 \mu\text{V K}^{-1}$ . [82]

The electrical resistivity in the series  $\text{Fe}_2\text{V}_{1-x}\text{Co}_x\text{Al}$  is reduced with increasing Co substitution. The Seebeck coefficient is negative (to determine whether this is due to the small amount of Al deficiency reference samples

of stoichiometric undoped  $\text{Fe}_2\text{VAl}$  have been prepared and will be measured) and the absolute value diminishes with increasing Co content. Consequently, the overall power factor is greatly reduced with increasing amount of Co. The Mn doped sample showed p-type semiconducting behavior over the whole temperature range. This is most likely due to the Mn loss in the arc melting process, similar trends in the thermoelectric properties have been reported for V-deficient  $\text{Fe}_2\text{VAl}$ . [82]

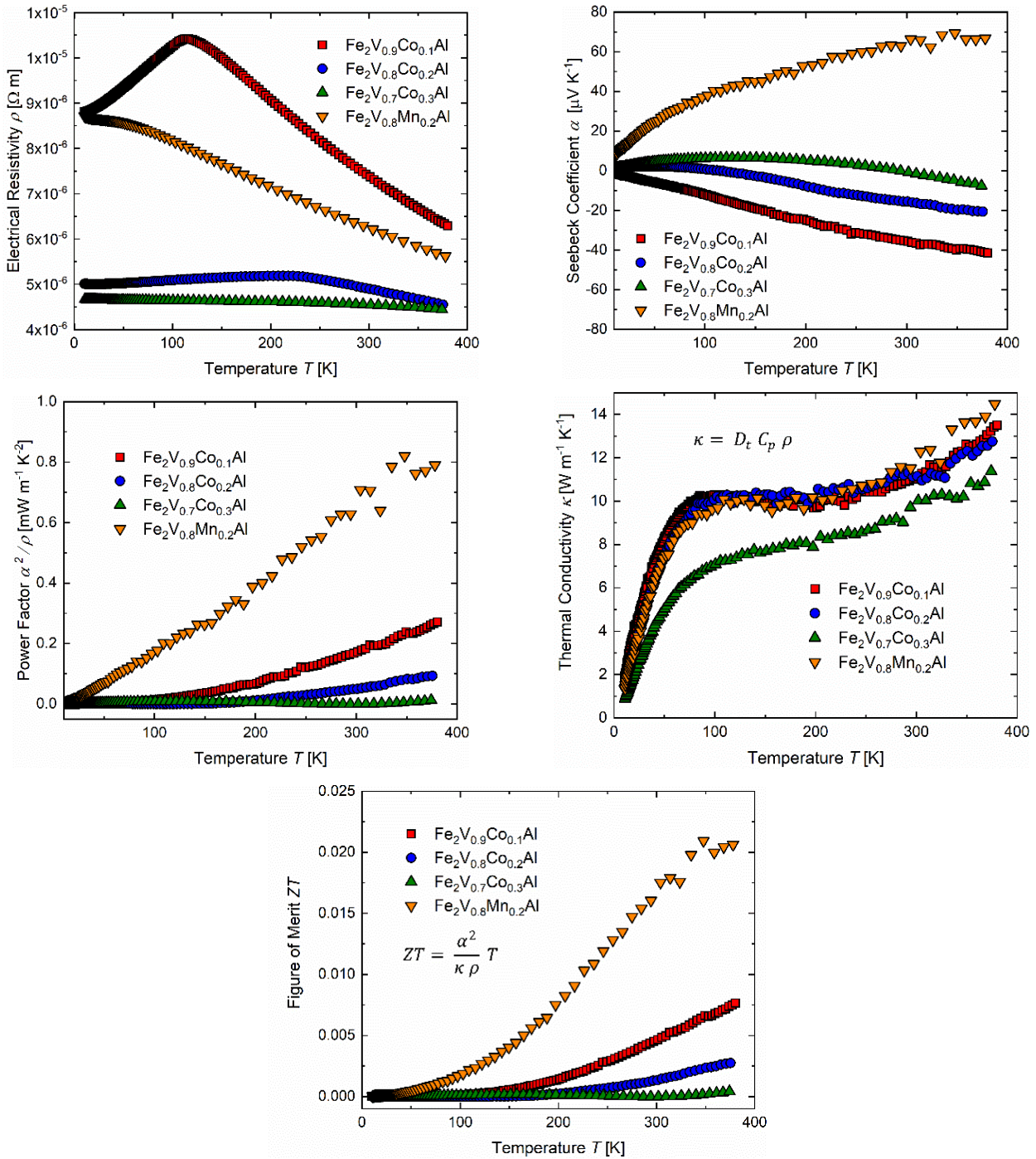


**Figure 5.7** Temperature dependence of the thermoelectric properties of the samples  $\text{Fe}_2\text{V}_{1-x}\text{Co}_x\text{Al}$  and  $\text{Fe}_2\text{V}_{0.8}\text{Mn}_{0.2}\text{Al}$  in the temperature range 10 – 373 K measured by PPMS-TTO.

The electrical resistivity of  $\text{Fe}_2\text{V}_{0.9}\text{Co}_{0.1}\text{Al}$  and  $\text{Fe}_2\text{V}_{0.8}\text{Co}_{0.2}\text{Al}$  show metallic behavior at low temperatures  $T < \theta$  with a maximum at the Curie temperature  $\theta$  where it changes to semiconducting behavior for  $T > \theta$ . When applying a magnetic field this maximum, which is caused by the scattering of conduction electrons on spin fluctuations, is suppressed.  $\text{Fe}_2\text{V}_{0.7}\text{Co}_{0.3}\text{Al}$  and  $\text{Fe}_2\text{V}_{0.8}\text{Mn}_{0.2}\text{Al}$  show semiconducting behavior throughout the whole temperature range.

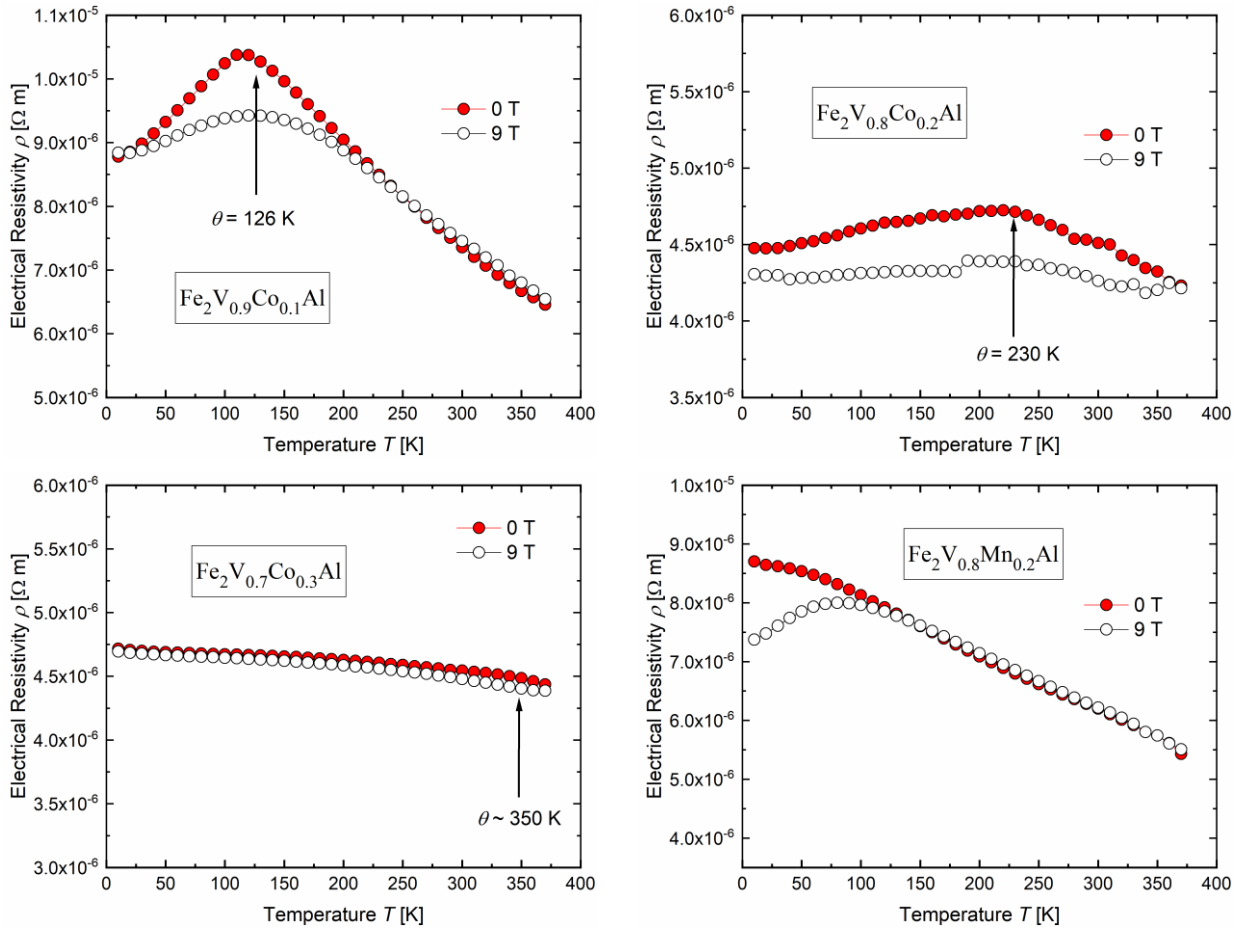


**Figure 5.8** Temperature dependence of the electrical resistivity of the samples  $\text{Fe}_2\text{V}_{1-x}\text{Co}_x\text{Al}$  and  $\text{Fe}_2\text{V}_{0.8}\text{Mn}_{0.2}\text{Al}$  in the temperature range 10 – 373 K with and without applied magnetic field measured by PPMS-ACT.

The effect of the applied magnetic field on the temperature dependence of the Seebeck coefficient is shown in Figure 5.9. The contribution of electrons as charge carriers to the Seebeck coefficient is reduced when a strong magnetic field is applied. This effect is most pronounced close to the Curie temperature  $\theta$  where a maximum in the plot of  $|\alpha_{0T} - \alpha_{9T}|$  against the temperature can be observed (Figure 5.10). This is attributed to spin fluctuation contributions to the Seebeck coefficient, which is suppressed by the application of a magnetic field. [16] In the samples  $\text{Fe}_2\text{V}_{0.8}\text{Co}_{0.2}\text{Al}$  and  $\text{Fe}_2\text{V}_{0.7}\text{Co}_{0.3}\text{Al}$  a positive contribution to the Seebeck coefficient can be observed at low temperatures.

In these samples, both holes and electrons contribute to the Seebeck coefficient according to

$$\alpha = \frac{\alpha_p \sigma_p + \alpha_n \sigma_n}{\sigma_p + \sigma_n} \quad (5.1)$$

with  $\sigma_n$ ,  $\sigma_p$ ,  $\alpha_n$  and  $\alpha_p$  being the electrical conductivity and Seebeck coefficient due to electrons and holes respectively. This behavior resembles the temperature dependence of  $\text{Fe}_{2-x}\text{Ni}_x\text{VAl}$  in which an impurity state was introduced in the electronic DOS in the pseudo-gap by the Fe/Ni substitution. [174]

The contribution of holes to the Seebeck coefficient appears to be unaffected by the magnetic field however as shown in Figure 5.9 on the p-type  $\text{Fe}_2\text{V}_{0.8}\text{Mn}_{0.2}\text{Al}$ .

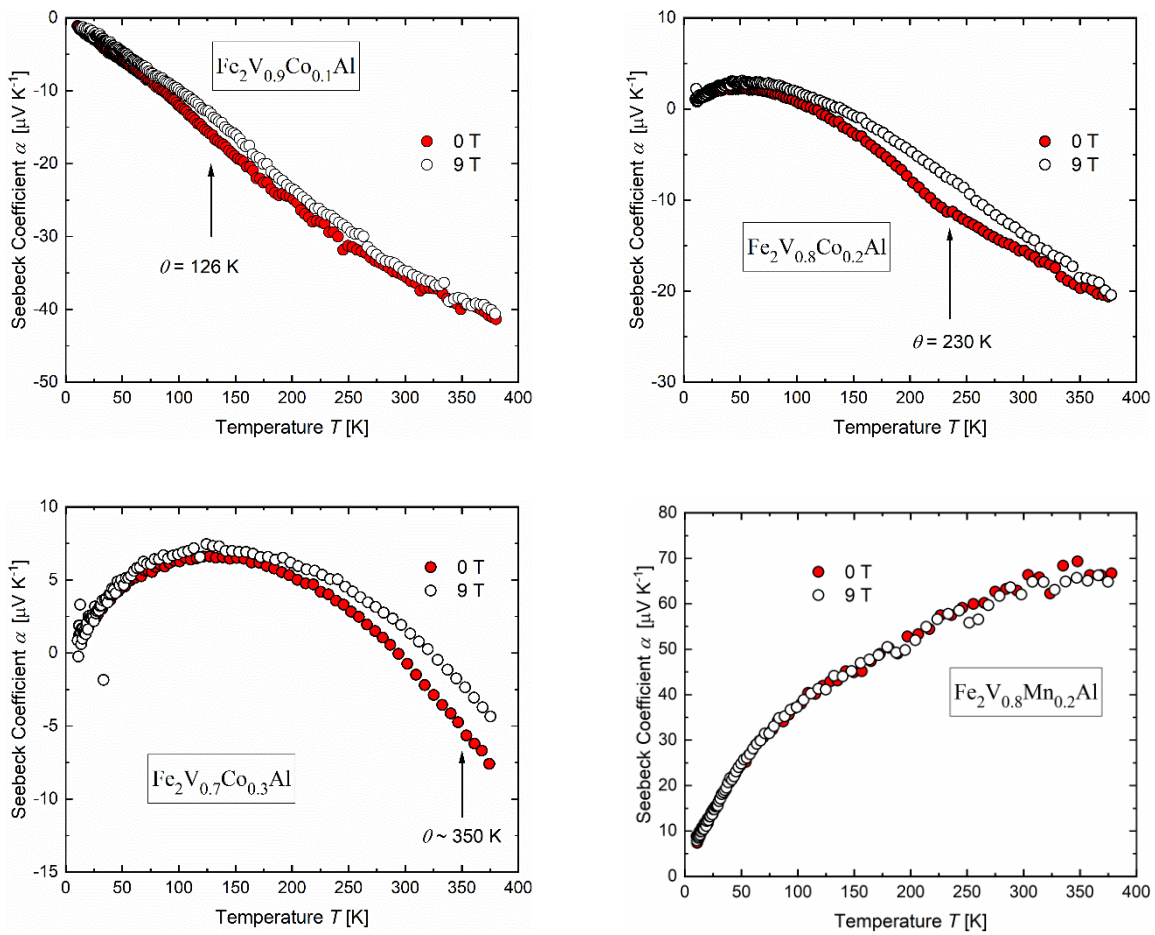


**Figure 5.9** Temperature dependence of the Seebeck coefficient of the samples  $\text{Fe}_2\text{V}_{1-x}\text{Co}_x\text{Al}$  and  $\text{Fe}_2\text{V}_{0.8}\text{Mn}_{0.2}\text{Al}$  in the temperature range 10 – 373 K with and without applied magnetic field.

The maximum of  $|\alpha_{0T} - \alpha_{9T}|$  is shifted towards higher temperatures with increasing Co content in the material in correlation to the change in the Curie temperature. At the same time, the absolute value of the Seebeck coefficient is reduced, resulting in a deterioration of the overall thermoelectric performance. To optimize the thermoelectric properties with a maximum in the Seebeck coefficient enhancement close to room temperature,

additional samples with fixed V/Co (and V/Mn if the newly synthesized  $\text{Fe}_2\text{V}_{1-x}\text{Mn}_x\text{Al}$  samples show ferromagnetic behavior) substitution and additional variation in either the Al content or Al/Si substitution will be necessary.

It is difficult to estimate the total spin fluctuation contribution to the Seebeck coefficient due to the additional contribution by holes. The total contribution can be estimated by the difference of the measured Seebeck coefficient and the linear extrapolation of the low temperature part of the Seebeck measurement which is assumed to be equal to the Seebeck from the diffusion of charge carriers.[16]

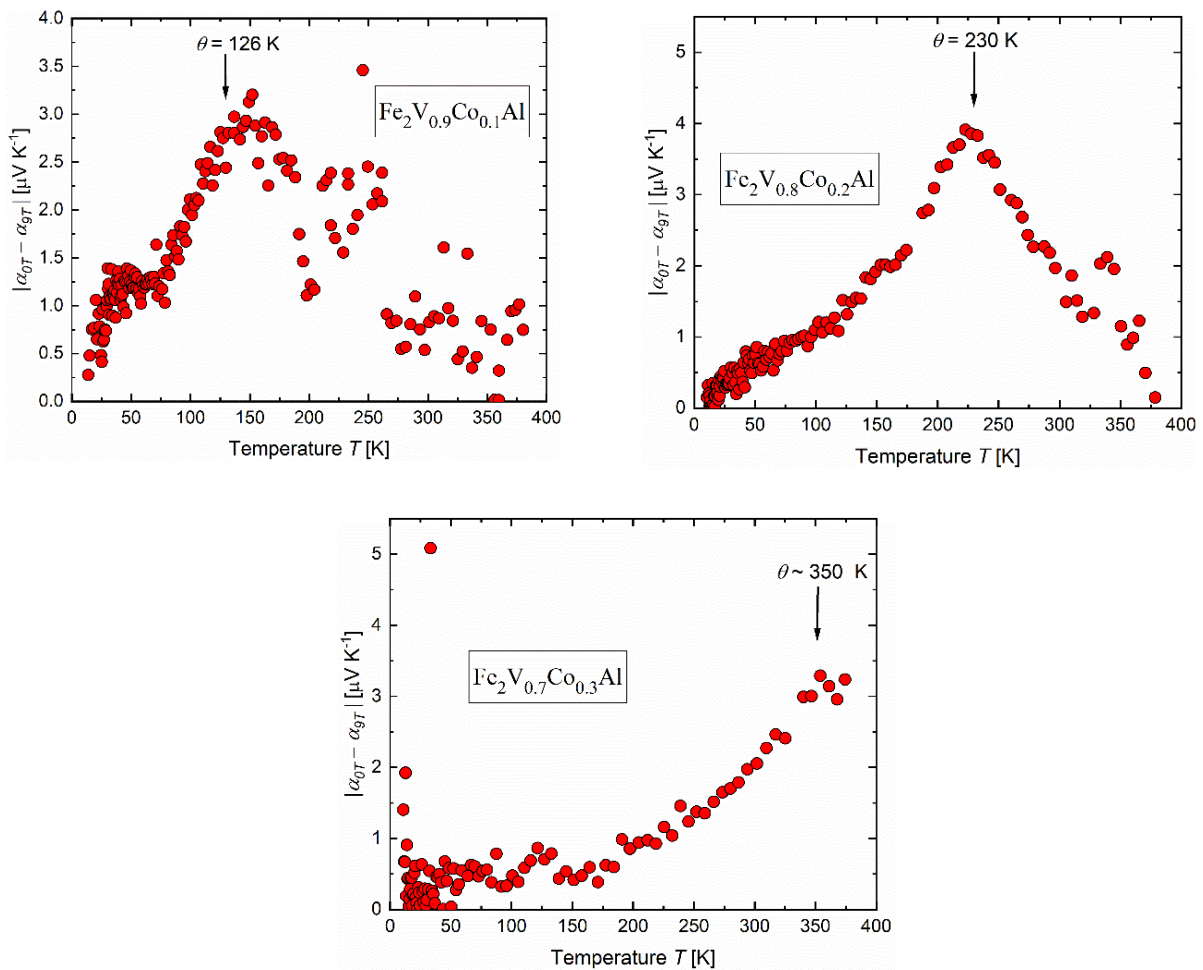


**Figure 5.10** Temperature dependence of the Seebeck coefficient with and without applied magnetic field  $|\alpha_{0T} - \alpha_{9T}|$  of the samples  $\text{Fe}_2\text{V}_{1-x}\text{Co}_x\text{Al}$  in the temperature range 10 – 373 K.

## 5.4 Conclusion

The thermoelectric and magnetic properties of  $\text{Fe}_2\text{V}_{(1-x)}\text{M}_x\text{Al}$  ( $M = \text{Co}, \text{Mn}; x = 0.1 - 0.3$ ) Heusler alloys have been studied at low temperatures. Substitution of V with Co resulted in weakly ferromagnetic n-type materials which showed the desired enhancement of the Seebeck coefficient through spin fluctuation. By increasing the cobalt content, it was possible to shift the Curie temperature and thus the temperature of maximum

enhancement of the Seebeck coefficient towards temperatures  $> 300$  K. Increased doping lead to a reduction in the power factor, most likely due to the introduction of a Co impurity band in the pseudo-gap. Further studies to optimize the thermoelectric properties of the material, for example by varying the composition or co-doping, will be required.

Mn doped samples showed p-type behavior due to Mn losses which were observed during arc melting. The Seebeck coefficient of the p-type sample of nominal composition  $\text{Fe}_2\text{V}_{0.8}\text{Mn}_{0.2}\text{Al}$  showed no difference in the measurement of the Seebeck coefficient with and without the application of magnetic fields. A new series of Mn doped samples is being prepared and measured.

### 5.5 Acknowledgements

We wish to thank Mitsuaki Nishio of the NIMS Sengen Materials Analysis Station for performing the quantitative analysis by WDX-EPMA SEM.

## **Conclusion and Outlook**

In this thesis, thermoelectric materials for high and room temperature in an effort to explore novel areas of application have been studied. The main results will be summarized here.

Higher borides –  $\text{REB}_{66}$  ( $\text{RE} = \text{Y}, \text{Sm}, \text{Ho}, \text{Tm}$  and  $\text{Yb}$ ) and boron carbide - have been studied for the potential application as high temperature thermoelectric materials. These results contribute to the understanding of the physical properties of these materials and also their processing.  $\text{REB}_{66}$  was studied in both single crystalline as well as polycrystalline form. The investigation of single crystalline  $\text{YbB}_{66}$  had the purpose to determine the possible contribution of mixed valence to the thermoelectric properties of  $\text{REB}_{66}$  materials. It was however found by the determination of the effective magnetic moment that ytterbium in  $\text{YbB}_{66}$  is exclusively trivalent. Its thermoelectric transport properties were very similar to  $\text{SmB}_{66}$ . It was found from the determination of the chemical composition (by inductively coupled plasma atomic emission spectroscopy and by single crystal structure refinement) that the chemical composition of the  $\text{YbB}_{66}$  single crystal was more ytterbium-rich with an  $\text{Yb}:\text{B}$  ratio of approximately 1:59. It is therefore suggested that the composition is the main influential factor for the electrical properties in  $\text{REB}_{66}$  instead of differences in the rare earth element. Regarding  $\text{SmB}_{66}$ , an alternative method to the measurement of the magnetic susceptibility for determination of the valence state of samarium in  $\text{SmB}_{66}$  should be employed considering the deviations of the effective magnetic moment of  $\text{Sm}(+3)$  from the theoretical values. To further elaborate these findings, an alternative synthesis method to the difficult process of single crystal growth for  $\text{REB}_{66}$  compounds was established. The process involves borothermal reduction, arc melting and spark plasma sintering to prepare single phase  $\text{REB}_{66}$  samples of high purity. The thermoelectric properties of polycrystalline  $\text{REB}_{66}$  prepared by this process were shown to be equivalent to those of the single crystals from previous investigations. This faster and simpler process could help with the potential industrial processing of these high temperature thermoelectric materials. The process currently involves arc melting for the formation of the  $\text{REB}_{66}$  phase which is responsible for some uncertainty in the chemical composition of the materials. To further improve this process, it will be necessary to find conditions to fully form the  $\text{REB}_{66}$  phase in the initial sintering in the high-frequency induction furnace to omit the arc melting.

The processing and thermoelectric properties, particularly the electrical transport properties, were further studied on high purity boron carbide (synthesized by a solution based method by collaborators) and commercially available boron carbide powders. Higher borides generally have highly disordered and complex crystal structures and unusual physical properties. Different conduction mechanisms were compared to further the understanding of the thermoelectric properties of these materials by measuring the temperature dependent properties in a temperature range of 10 – 973 K. It was proposed that the electrical properties of boron carbide could be described using the nearest-neighbor hopping mechanism instead of the bipolaron hopping / variable range hopping + band conduction used so far. This is supported by the temperature dependence of electrical resistivity and Seebeck coefficient which fit the theoretical predictions of the nearest-neighbor hopping mechanism fairly well.

While a major part of the work in this thesis is dedicated to the investigation of high temperature thermoelectric materials, there is additional interest in finding high performance materials on the other end of the spectrum for low/room temperature applications.  $\text{Fe}_2\text{VAI}$  Full Heusler alloys have been investigated for this purpose and promising initial results were found. Substitution of V by Co in  $\text{Fe}_2\text{VAI}$  was found to be successful in achieving ferromagnetic materials with Curie temperatures of magnetic ordering increasing with increasing Co content. This was first aim of this work since the spin fluctuation contribution to the Seebeck coefficient has a maximum at the Curie temperature. While the initial goal was achieved, the thermoelectric performance of the material is still low so further improvement will be necessary. To this end, changes in the composition and different substitutions should be employed since the material is very susceptible to off-stoichiometry.

## **List of Publications**

**1. “On the thermoelectric and magnetic properties, hardness, and crystal structure of the higher boride  $\text{YbB}_{66}$ ”**

P. Sauerschnig, K. Tsuchiya, T. Tanaka, Y. Michiue, O. Sologub, S. Yin, A. Yoshikawa, T. Shishido, and T. Mori

Journal of Alloys and Compounds 813 (2020) 152182.

**2. “Thermoelectric properties of phase pure boron carbide prepared by a solution-based method”**

P. Sauerschnig, J.L. Watts, J.B. Vaney, P.C. Talbot, J.A. Alarco, I.D.R. Mackinnon, and T. Mori

Advances in Applied Ceramics 119:2 (2020) 97-106

**3. “Thermoelectric and magnetic properties of spark plasma sintered  $\text{REB}_{66}$  ( $\text{RE} = \text{Y, Sm, Ho, Tm, Yb}$ )”**

P. Sauerchnig, J.B. Vaney, Y. Michiue, K. Yubuta, A. Yoshikawa, T. Shishido, and T. Mori

(under review)

**4. “Study of the thermopower enhancement by spin fluctuation in ferromagnetic  $\text{Fe}_2\text{V}_{1-x}(\text{Mn,Co})_x\text{Al}$  Heusler alloys”**

P. Sauerchnig, N. Tsujii and T. Mori

(in preparation)

## List of Figures

- Figure 1.1** Thermoelectric generator (left) and Peltier element (right). 7
- Figure 1.2** Carrier concentration dependence of the thermoelectric properties. Copyright Nature Publishing Group[22] 8
- Figure 1.3** Conversion efficiency for several types of heat engines with  $T_{\text{cold}} = 300$  K. Copyright by Annual Reviews [18] 9
- Figure 1.4** Literature  $ZT$  values for higher boride materials. References: [a] H.K. Kim et al. [40], [b] T. Akashi et al. [41], [c] J.-L. Innocent et al. [42], M.A. Hossain et al. [43], [e] M.A. Hossain et al. [8], [f] A. Sussardi et al. [7], [g] A. Prytuliak et al. [44], [h] S. Maruyama et al. [30]. 12
- Figure 1.5** Hexagonal (blue) and rhombohedral (red) unit cell of boron carbide. Copyright by John Wiley and Sons [62] 15
- Figure 1.6** Elements forming  $X_2YZ$  Heusler alloys (Available under CC-BY-SA license: <http://creativecommons.org/licenses/by-sa/3.0/deed.en>)[77] 16
- Figure 1.7**  $\text{Fe}_2\text{VAI}$  band structure near  $E_F$  (left) and electronic density of states  $N(E)$  (right). Contributions from Fe d (dotted) and V d (dashed) electronic states. [85] 17
- Figure 1.8** Optical floating zone single crystal growth experimental setup. 19
- Figure 1.9** Floating zone single crystal growth from polycrystalline seed rod (schematic). (After [99] and [100]) 21
- Figure 1.10** Spark plasma sintering system (schematic). 22
- Figure 1.11** Seebeck coefficient and electrical resistivity (a) measurement setup (schematic) (b) sample shape and dimensions. 23
- Figure 1.12** Laser flash analysis (a) measurement setup (schematic) (b) sample shape and dimensions. 25
- Figure 2.1** Optical floating zone single crystal growth setup (here  $\text{SmB}_{66}$ ). The seed rod is placed at the bottom in an alumina sample holder. The feed rod is suspended from the top by tungsten wires. The light of four xenon lamps is focused in the center by mirrors. 30
- Figure 2.2** The  $\text{YbB}_{66}$  crystal was cleaved along its growth direction. [127] 31
- Figure 2.3**  $\text{YbB}_{66}$  XRD patterns for the cleaved surface and the simulated powder pattern according to the single crystal structural solution.  $\text{Cu-K}\alpha_{1,2}$  - radiation was used for the measurement of the cleaved 32

surface. The presence of exclusively (h 0 0) reflections suggest crystal growth orientation along the a-axis. [127]

**Figure 2.4** Isosurface plot of the probability densities of Yb1 and Yb2 atoms. Isosurface level is 1 (atom/Å<sup>3</sup>). [127] 33

**Figure 2.5** Partial view of the unit cell of YbB<sub>66</sub> and SmB<sub>66</sub>. (0 ≤ x ≤ 0.5 and 0 ≤ y ≤ 0.5). B<sub>12</sub>(B<sub>12</sub>)<sub>12</sub> super-icosahedra are drawn in yellow with a brown central B<sub>12</sub> icosahedron. “B<sub>80</sub> clusters” are formed by red boron atoms. RE-RE pairs are drawn in grey (partially occupied). The additionally introduced boron sites with low occupancy and the 192j Yb<sub>2</sub>/Sm<sub>2</sub> positions have been omitted in this figure for visual clarity. [127] 35

**Figure 2.6** Molar magnetic susceptibility  $\chi_m$  and inverse molar magnetic susceptibility  $(\chi_m - \chi_0)^{-1}$  of YbB<sub>66</sub> plotted against the temperature  $T$  with modified Curie-Weiss fitting. [127] 38

**Figure 2.7** Temperature dependence of the electrical resistivity  $\rho$  with SmB<sub>66</sub> [7], YB<sub>66</sub> [56], YB<sub>48</sub> [8] and ErB<sub>66</sub> [119] as reference values. [127] 40

**Figure 2.8** Temperature dependence of YbB<sub>66</sub>  $\log \rho$  against  $T^{-0.25}$  according to Mott’s variable range hopping mechanism with SmB<sub>66</sub> [7], YB<sub>66</sub> [56], YB<sub>48</sub> [8] and ErB<sub>66</sub> [119] as reference values. [127] 41

**Figure 2.9** Temperature dependence of the Seebeck coefficient of YbB<sub>66</sub> with SmB<sub>66</sub> [7], YB<sub>66</sub> [56], YB<sub>48</sub> [8] and ErB<sub>66</sub> [119] as reference values. [127] 43

**Figure 2.10** Temperature dependence of the Power Factor of YbB<sub>66</sub> with SmB<sub>66</sub> [7], YB<sub>66</sub> [56], YB<sub>48</sub> [8] and ErB<sub>66</sub> [119] as reference values. [127] 43

**Figure 2.11** Temperature dependence of the thermal diffusivity  $D_t$  of YbB<sub>66</sub> with SmB<sub>66</sub> [7] as reference. [127] 44

**Figure 2.12** Temperature dependence of the specific heat  $C_p$  of YbB<sub>66</sub> with SmB<sub>66</sub> [7] as reference. [127] 44

**Figure 2.13** Temperature dependence of the thermal conductivity  $\kappa$  of YbB<sub>66</sub> with SmB<sub>66</sub> [7], YB<sub>66</sub> [56] and YB<sub>48</sub> [8] as reference values. [127] 45

**Figure 2.14** Temperature dependence of the dimensionless Figure of Merit ZT of YbB<sub>66</sub> with SmB<sub>66</sub> [7], YB<sub>66</sub> [56] and YB<sub>48</sub> [8] as reference values. [127] 46

**Figure 3.1** Sintering schedule for REB<sub>66</sub>. 49

- Figure 3.2** XRD patterns of REB<sub>66</sub> (RE = Y, Sm, Ho, Tm, Yb) prepared by spark plasma sintering. 52  
Peaks of Si<sub>3</sub>N<sub>4</sub> (●) introduced from the mortar during pulverization for the powder XRD measurement. The Bragg-positions at the bottom refer to the YB<sub>66</sub> structure- type.[46]
- Figure 3.3** SEM-EDX images of REB<sub>66</sub> samples prepared by spark plasma sintering. The samples 53  
show density close to 100% of the theoretical values with the exception of YB<sub>66</sub>. The elemental mapping of the samples shows that the prepared samples are homogenous and single phase, with the exception of SmB<sub>66</sub> and YbB<sub>66</sub>. SmB<sub>66</sub> has small quantities of SmB<sub>6</sub> (bright). Yb-mapping shows a Yb-deficient secondary phase, which is slightly B-richer, most likely β-rhombohedral boron (bright phase in B mapping, dark phase in Yb mapping).
- Figure 3.4** SEM images (mixed BSE+SE detector) of SmB<sub>66</sub> sintered at 1750 °C. The sample contains 54  
areas with secondary phases, SmB<sub>6</sub> (bright) and elemental boron (dark). Top: sample edge, Bottom: sample center.
- Figure 3.5** Magnetic Susceptibility of REB<sub>66</sub> (RE = Ho, Tm, Yb) prepared by spark plasma sintering 56  
measured with an applied magnetic field of H = 1 kOe. Theoretical values for  $\mu_{\text{eff}}(\text{RE}^{3+}) = g[J(J+1)]^{1/2}$  taken from “Kittel – Introduction to Solid State Physics”[131] The curve fitting was performed for the temperature region 100 – 300 K in which all samples follow ideal Curie-Weiss behavior. The dashed line shows the continuation of the fitting curve up to the respective Curie-Weiss temperature.
- Figure 3.6** Plot of the Curie-Weiss temperatures of REB<sub>66</sub> for the trivalent rare earth ions adapted from 57  
T. Mori.[4] Value for YbB<sub>66</sub> single crystal from Sauerschnig et al.[127]
- Figure 3.7** Electrical resistivity  $\rho$  for REB<sub>66</sub> (RE = Y, Sm, Ho, Tm, Yb) according to Mott’s variable 58  
range hopping mechanism prepared by spark plasma sintering. Data for the single crystal of SmB<sub>66</sub> and YbB<sub>66</sub> plotted as a reference. [7,127]
- Figure 3.8** Seebeck coefficient  $\alpha$  for REB<sub>66</sub> (RE = Y, Sm, Ho, Tm, Yb) prepared by spark plasma 60  
sintering. Data for the single crystal of SmB<sub>66</sub> and YbB<sub>66</sub> plotted as a reference. [7,127]
- Figure 3.9** Power Factor  $\alpha^2/\rho$  for REB<sub>66</sub> (RE = Y, Sm, Ho, Tm, Yb) prepared by spark plasma sintering. 61  
Data for the single crystal of SmB<sub>66</sub> and YbB<sub>66</sub> plotted as a reference. [7,127]
- Figure 3.10** Thermal conductivity  $\kappa$  of REB<sub>66</sub> (RE = Y, Sm, Ho, Tm, Yb) prepared by spark plasma 62  
sintering.  $D_t$ ,  $C_p$  and  $\rho$  are the thermal diffusivity, specific heat and density respectively. Data for the single crystal of SmB<sub>66</sub> and YbB<sub>66</sub> plotted as a reference. [7,127]
- Figure 3.11** Figure of merit  $ZT$  of REB<sub>66</sub> (RE = Y, Sm, Ho, Tm, Yb) prepared by spark plasma sintering. 63  
 $\alpha$ ,  $\kappa$  and  $\rho$  are the Seebeck coefficient, thermal conductivity and electrical resistivity respectively. The

data of Seebeck coefficient and resistivity were interpolated to match the measurement temperature of the thermal conductivity. Data for the single crystal of  $\text{SmB}_{66}$  and  $\text{YbB}_{66}$  plotted as a reference. [7,127]

- Figure 4.1** Sintering schedule for boron carbide. 67
- Figure 4.2** Powder XRD patterns (Co  $K_{\alpha}$  radiation) for four boron carbide samples. Key reflections for boron carbide are indexed;  $\blacklozenge$  shows the position of free carbon. [108] 68
- Figure 4.3** SEM images of boron carbide samples showing significant differences in particle size and morphology. Samples are (a) Boron Carbide 3, (b) Boron Carbide 2, (c) Boron Carbide 1 and (d) High Purity. [108] 79
- Figure 4.4** Relative density of the Boron Carbide 3 sintered at different temperatures at 50 MPa applied pressure and holding time of 10 min. 70
- Fig. 4.5** X-Ray diffraction patterns of boron carbide samples after SPS sintering showing a free carbon peak at  $26.5^{\circ}$  ( $\blacklozenge$ ). Additional peaks due to contamination from  $\text{Si}_3\text{N}_4$  ( $\bullet$ ) mortar during pulverization in preparation for the XRD measurements. [108] 71
- Figure 4.6** X-Ray diffraction patterns of boron carbide samples after SPS sintering showing a free carbon ( $\blacklozenge$ ) peak at  $26.5^{\circ}$ . Additional peak at  $27.0^{\circ}$  due to contamination from  $\text{Si}_3\text{N}_4$  ( $\bullet$ ) mortar during pulverization in preparation for the XRD measurements. [108] 72
- Figure 4.7** Fracture surface image of the sintered High Purity boron carbide powder showing close to 100% densification. The surface was freshly fractured before the measurement. [108] 72
- Figure 4.8** Temperature dependence of the electrical resistivity  $\rho$  of boron carbide samples. [108] 74
- Figure 4.9** Plot of the electrical resistivity  $\rho$  vs.  $T^{-1/4}$  according to Mott's variable range hopping conduction for the whole temperature range 25 – 973 K (left) and the low temperature range 25 – 300 K (right) for the samples High Purity and Boron Carbide 2. The black line indicates the fitting of the resistivity following the VRH conduction mechanism. 74
- Figure 4.10** Plot of the electrical resistivity  $\rho / T$  vs.  $1000 / T$  according to the small bipolaron hopping conduction mechanism and electrical resistivity  $\rho$  vs  $1000 / T$  according to Arrhenius-type conduction (thermally activated band conduction or Nearest-Neighbor Hopping conduction) for the samples High Purity and Boron Carbide 2. [108] 75
- Figure 4.11** Temperature dependence of the Seebeck coefficient  $\alpha$  of boron carbide samples. [108] 77
- Figure 4.12** Temperature dependence of the power factor  $pf = \alpha^2/\rho$  of boron carbide samples. [108] 78
- Figure 4.13** Temperature dependence of the thermal conductivity  $\kappa$  of boron carbide samples. [108] 80

- Figure 4.14** Temperature dependence of the figure of merit  $ZT$  of boron carbide samples. [108] 80
- Figure 5.1** Sintering schedule for Full Heusler  $\text{Fe}_2\text{V}_{1-x}(\text{Co,Mn})_x\text{Al}$  . 84
- Figure 5.2** ACT electrical resistivity measurement setup. A copper block (high thermal conductivity for even temperature distribution in the sample) is wrapped in Kapton tape for electrical insulation. Short copper wires are attached to the samples with two-component silver paste and connected to the contacts of the ACT sample puck. 85
- Figure 5.3** XRD patterns of the samples  $\text{Fe}_2\text{V}_{1-x}\text{Co}_x\text{Al}$  and  $\text{Fe}_2\text{V}_{0.8}\text{Mn}_{0.2}\text{Al}$  after spark plasma sintering at 900 °C using Cu  $K\alpha$  radiation. 85
- Figure 5.4** SEM micrographs (BSE detector) of the samples  $\text{Fe}_2\text{V}_{1-x}\text{Co}_x\text{Al}$  and  $\text{Fe}_2\text{V}_{0.8}\text{Mn}_{0.2}\text{Al}$  (grey) after spark plasma sintering at 900 °C. The samples contain WC impurities (white) due to contamination from the jar and balls during the ball milling and  $\text{Al}_2\text{O}_3$  and small pores (black). 86
- Figure 5.5** Temperature dependence of the magnetic susceptibility/magnetization of the samples  $\text{Fe}_2\text{V}_{1-x}\text{Co}_x\text{Al}$ . 87
- Figure 5.6** Magnetic field dependence of the magnetization of the samples  $\text{Fe}_2\text{V}_{1-x}\text{Co}_x\text{Al}$  at 5 – 300 K. 88
- Figure 5.7** Temperature dependence of the thermoelectric properties of the samples  $\text{Fe}_2\text{V}_{1-x}\text{Co}_x\text{Al}$  and  $\text{Fe}_2\text{V}_{0.8}\text{Mn}_{0.2}\text{Al}$  in the temperature range 10 – 373 K measured by PPMS-TTO. 89
- Figure 5.8** Temperature dependence of the electrical resistivity of the samples  $\text{Fe}_2\text{V}_{1-x}\text{Co}_x\text{Al}$  and  $\text{Fe}_2\text{V}_{0.8}\text{Mn}_{0.2}\text{Al}$  in the temperature range 10 – 373 K with and without applied magnetic field measured by PPMS-ACT. 90
- Figure 5.9** Temperature dependence of the Seebeck coefficient of the samples  $\text{Fe}_2\text{V}_{1-x}\text{Co}_x\text{Al}$  and  $\text{Fe}_2\text{V}_{0.8}\text{Mn}_{0.2}\text{Al}$  in the temperature range 10 – 373 K with and without applied magnetic field. 91
- Figure 5.10** Temperature dependence of the Seebeck coefficient with and without applied magnetic field  $|\alpha_{0T} - \alpha_{9T}|$  of the samples  $\text{Fe}_2\text{V}_{1-x}\text{Co}_x\text{Al}$  in the temperature range 10 – 373 K. 92

## List of Tables

<b>Table 1.1</b> Standardized crystallographic data for Cu <sub>2</sub> MnAl structure type. [77,78]	17
<b>Table 2.1</b> Crystal data and details for data collection and refinement. [127]	34
<b>Table 2.2</b> Atomic coordinates, atomic displacement parameters and occupancies of the refinement of the crystal structure of a YbB <sub>66</sub> single crystal. [127]	36
<b>Table 2.3</b> Atomic coordinates, atomic displacement parameters and occupancies of the refinement of the crystal structure of a SmB <sub>66</sub> single crystal.	37
<b>Table 3.1</b> Summarized sintering parameters and characterization results of REB <sub>66</sub> (RE = Y, Sm, Ho, Tm, Yb) prepared by spark plasma sintering.	51
<b>Table 3.2</b> Magnetic properties of REB <sub>66</sub> (RE = Ho, Tm, Yb). Curie constant C, Curie-Weiss temperature $\theta$ and effective magnetic moment $\mu_{eff}$ derived from fitting the inverse magnetic susceptibility $\chi^{-1}$ . The theoretical effective magnetic moment $\mu_{eff}(RE^{3+}) = g[J(J+1)]^{1/2}$ is taken from “Kittel – Introduction to Solid State Physics” [131].	55
<b>Table 3.3</b> Characteristic temperatures and resistivity of REB <sub>66</sub> (RE=Y, Sm, Ho, Tm, Yb) according to Mott’s variable-range hopping (VRH) mechanism.	59
<b>Table 4.1</b> Sintering temperatures and holding times (at sintering temperature). [108]	66
<b>Table 4.2</b> Phase weight content (wt%) and corresponding carbon content (at%) of phases and associated R <sub>wp</sub> value for boron carbide samples reproduced from the work of <i>Watts et al.</i> [13] [108]	69
<b>Table 4.3</b> Average particle sizes for boron carbide samples. [108]	70
<b>Table 4.4</b> Densities of the sintered boron carbide powder. [108]	71
<b>Table 4.5</b> Activation/Hopping energies for the small bipolaron hopping (BPH) and nearest neighbor hopping (NNH)/Thermally activated conduction (TAC). [108]	76
<b>Table 5.1</b> WDX-EPMA SEM analysis of the samples Fe <sub>2</sub> V <sub>1-x</sub> Co <sub>x</sub> Al and Fe <sub>2</sub> V <sub>0.8</sub> Mn <sub>0.2</sub> Al after spark plasma sintering at 900 °C.	87

**List of Abbreviations**

ACT	alternating current transport
BPH	bipolaron hopping
BSE	backscattered electron
CIP	cold isostatic press
CVD	chemical vapor deposition
DSC	differential scanning calorimetry
DOS	density of states
EDX	energy-dispersive X-Ray detector
FC	field cooling
FE	field emission
h-BN	hexagonal boron nitride
HF	high frequency
ICP-AES	inductively coupled plasma atomic emission spectroscopy
LFA	laser flash analysis
MEM	maximum entropy method
MPMS	magnetic properties measurement system
HPT	high pressure torsion
NNH	nearest neighbor hopping
PPMS	physical properties measurement system
RE	rare earth
RKKY	Ruderman-Kittel-Kasuya-Yosida interaction
SE	secondary electron
SEM	scanning electron microscopy
SQUID	superconducting quantum interference device
SPS	spark plasma sintering
TAC	thermally activated band conduction
TTO	thermal transport option
WDX	wavelength dispersive X-Ray detector
XPS	X-Ray photoelectron spectroscopy
XRD	X-Ray diffraction
ZFC	zero-field cooling

## List of Physical Quantities, Natural Constants and Their Units

Activation energy	$E_A, \varepsilon_3$	[eV]
Characteristic resistivity	$\rho_0$	[ $\Omega$ m]
Characteristic temperature	$T_0$	[K]
Cross section area	$A$	[m <sup>2</sup> ]
Curie constant	$C$	[cm <sup>3</sup> K mol <sup>-1</sup> Oe <sup>-1</sup> ]
Curie / Curie-Weiss temperature	$\theta$	[K]
Density	$\rho_m$	[g cm <sup>-3</sup> ]
Density of States	$N(E)$	[eV <sup>-1</sup> ]
Diameter	$\phi$	[m]
Effective mass	$m^*$	[ $m_e$ ]
Charge carrier concentration	$n$	[cm <sup>-3</sup> ]
Charge carrier mobility	$\mu$	[m <sup>2</sup> V <sup>-1</sup> s <sup>-1</sup> ]
Fermi energy	$E_F$	[eV]
Figure of merit	$ZT$	[-]
Heat energy	$Q$	[J]
Hopping energy (NNH)	$E_H$	[eV]
Electrical current	$I$	[A]
Electrical conductivity	$\sigma$	[S m <sup>-1</sup> , $\Omega^{-1}$ m <sup>-1</sup> ]
Electrical resistance	$R$	[ $\Omega$ ]
Electrical resistivity	$\rho$	[ $\Omega$ m]
Gyromagnetic ratio	$g$	[-]
Length	$l, d$	[m]
Localization length	$\xi$	[m, Å]
Magnetic field strength	$H$	[Oe, A m <sup>-1</sup> ]
Magnetic Moment	$\mu$	[emu]
Magnetic Susceptibility	$\chi$	[emu cm <sup>-3</sup> Oe <sup>-1</sup> ]
Magnetization	$M$	[emu]
Mass	$m$	[kg]
Power factor	$pf$	[W m <sup>-1</sup> K <sup>-1</sup> ]
Pressure	$P$	[Pa]
Seebeck coefficient	$\alpha$	[V K <sup>-1</sup> ]
Sommerfeld coefficient	$\gamma$	[J g <sup>-1</sup> K <sup>-2</sup> ]
Specific heat	$C_p$	[J g <sup>-1</sup> K <sup>-1</sup> ]
Temperature	$T$	[K, °C]
Thermal conductivity	$\kappa$	[W m <sup>-1</sup> K <sup>-1</sup> ]
Thermal diffusivity	$D_t$	[m <sup>2</sup> s <sup>-1</sup> ]

Thermal-electrical conversion efficiency	$\eta$	[-]
Time	$t$	[s]
Total angular momentum quantum number	$J$	[-]
Vickers hardness	$HV$	[Pa, kp mm <sup>-2</sup> ]
Voltage	$\Delta V$	[V]
Volume fraction	$v$	[-]
Avogadro number	$N_A$	[6.022 x 10 <sup>23</sup> mol <sup>-1</sup> ]
Bohr magneton	$\mu_B$	[9.274 x 10 <sup>-24</sup> A m <sup>2</sup> ]
Boltzmann constant	$k_B$	[1.381 x 10 <sup>-23</sup> J K <sup>-1</sup> ]
Electron rest mass	$m_e$	[9.109 x 10 <sup>-31</sup> kg]
Elemental charge	$e$	[1.602 x 10 <sup>-19</sup> C]
Vacuum permeability	$\mu_0$	[4 $\pi$ x 10 <sup>-7</sup> V s A <sup>-1</sup> m <sup>-1</sup> ]

## **References**

- [1] D. Beretta, N. Neophytou, J.M. Hodges, M.G. Kanatzidis, D. Narducci, M. Martin- Gonzalez, M. Beekman, B. Balke, G. Cerretti, W. Tremel, A. Zevalkink, A.I. Hofmann, C. Müller, B. Döring, M. Campoy-Quiles, M. Caironi, Thermoelectrics: From history, a window to the future, *Mater. Sci. Eng. R Reports*. (2018). doi:10.1016/J.MSER.2018.09.001.
- [2] T. Mori, Novel Principles and Nanostructuring Methods for Enhanced Thermoelectrics, *Small*. 13 (2017) 1702013. doi:10.1002/sml.201702013.
- [3] C.B. Vining, An inconvenient truth about thermoelectrics, *Nat. Mater.* 8 (2009) 83–85. doi:10.1038/nmat2361.
- [4] T. Mori, Higher Borides, in: *Handb. Phys. Chem. Rare Earths*, Elsevier, 2008: pp. 105–173. doi:10.1016/S0168-1273(07)38003-3.
- [5] T. Mori, Thermoelectric and magnetic properties of rare earth borides: Boron cluster and layered compounds, *J. Solid State Chem.* 275 (2019) 70–82. doi:10.1016/J.JSSC.2019.03.046.
- [6] K. Yazawa, M. Hao, B. Wu, A.K. Silaen, C.Q. Zhou, T.S. Fisher, A. Shakouri, Thermoelectric topping cycles for power plants to eliminate cooling water consumption, *Energy Convers. Manag.* 84 (2014) 244–252. doi:https://doi.org/10.1016/j.enconman.2014.04.031.
- [7] A. Sussardi, T. Tanaka, A.U. Khan, L. Schlapbach, T. Mori, Enhanced thermoelectric properties of samarium boride, *J. Mater.* 1 (2015) 196–204. doi:10.1016/J.JMAT.2015.07.007.
- [8] M.A. Hossain, I. Tanaka, T. Tanaka, A.U. Khan, T. Mori, YB<sub>48</sub> the metal rich boundary of YB<sub>66</sub>; crystal growth and thermoelectric properties, *J. Phys. Chem. Solids.* 87 (2015) 221–227. doi:10.1016/J.JPCS.2015.08.015.
- [9] M. Bouchacourt, F. Thevenot, The correlation between the thermoelectric properties and stoichiometry in the boron carbide phase B<sub>4</sub>C-B<sub>10.5</sub>C, *J. Mater. Sci.* 20 (1985) 1237–1247. doi:10.1007/BF01026319.
- [10] M. Mikami, M. Mizoshiri, K. Ozaki, H. Takazawa, A. Yamamoto, Y. Terazawa, T. Takeuchi, Evaluation of the Thermoelectric Module Consisting of W-Doped Heusler Fe<sub>2</sub>VAl Alloy, *J. Electron. Mater.* 43 (2014) 1922–1926. doi:10.1007/s11664-013-2910-7.
- [11] H. Park, D. Lee, G. Park, S. Park, S. Khan, J. Kim, W. Kim, Energy harvesting using thermoelectricity for IoT (Internet of Things) and E-skin sensors, *J. Phys. Energy.* 1 (2019) 42001. doi:10.1088/2515-7655/ab2f1e.

- [12] M. Kasaya, F. Iga, M. Takigawa, T. Kasuya, Mixed Valence Properties of  $\text{YbB}_{12}$ , *J. Magn. Magn. Mater.* 47–48 (1985) 429–435. doi:10.1016/0304-8853(85)90458-5.
- [13] J.L. Watts, H.J. Spratt, P.C. Talbot, J.A. Alarco, N.A. Raftery, I.D.R. Mackinnon, Precision structural and phase analysis of boron carbide, *Ceram. Int.* (2020). doi:<https://doi.org/10.1016/j.ceramint.2020.01.120>.
- [14] T.L. Aselage, D. Emin, S.S. McCready, Bipolaron Hopping Conduction in Boron Carbides, *Phys. Status Solidi.* 218 (2000) 255–258. doi:10.1002/(SICI)1521-3951(200003)218:1<255::AID-PSSB255>3.0.CO;2-S.
- [15] H. Werheit, Present knowledge of electronic properties and charge transport of icosahedral boron-rich solids, *J. Phys. Conf. Ser.* 176 (2009) 012019, 11 pp. doi:10.1088/1742-6596/176/1/012019.
- [16] N. Tsujii, A. Nishide, J. Hayakawa, T. Mori, Observation of enhanced thermopower due to spin fluctuation in weak itinerant ferromagnet, *Sci. Adv.* 5 (2019) eaat5935. doi:10.1126/sciadv.aat5935.
- [17] T.J. Seebeck, Ueber die magnetische Polarisation der Metalle und Erze durch Temperaturdifferenz, *Ann. Phys.* 82 (1826) 253–286. doi:10.1002/andp.18260820302.
- [18] A. Shakouri, Recent Developments in Semiconductor Thermoelectric Physics and Materials, *Annu. Rev. Mater. Res.* 41 (2011) 399–431. doi:10.1146/annurev-matsci-062910-100445.
- [19] A.F. Ioffe, L.S. Stil'bans, E.K. Iordanishvili, T.S. Stavitskaya, A. Gelbtuch, G. Vineyard, *Semiconductor Thermoelements and Thermoelectric Cooling*, *Phys. Today.* 12 (1959) 42–42. doi:10.1063/1.3060810.
- [20] J.R. Sootsman, D.Y. Chung, M.G. Kanatzidis, New and Old Concepts in Thermoelectric Materials, *Angew. Chemie Int. Ed.* 48 (2009) 8616–8639. doi:10.1002/anie.200900598.
- [21] M.S. Dresselhaus, G. Chen, M.Y. Tang, R.G. Yang, H. Lee, D.Z. Wang, Z.F. Ren, J.-P. Fleurial, P. Gogna, New Directions for Low-Dimensional Thermoelectric Materials, *Adv. Mater.* 19 (2007) 1043–1053. doi:10.1002/adma.200600527.
- [22] G.J. Snyder, E.S. Toberer, Complex thermoelectric materials, *Nat. Mater.* 7 (2008) 105–114. doi:10.1038/nmat2090.
- [23] B. Cai, H. Hu, H.-L. Zhuang, J.-F. Li, Promising materials for thermoelectric applications, *J. Alloys Compd.* 806 (2019) 471–486. doi:10.1016/J.JALLCOM.2019.07.147.
- [24] D.M. Rowe, ed., *Thermoelectrics Handbook: Macro to Nano*, 1st ed., CRC Press, Boca Raton, 2006. <https://www.taylorfrancis.com/books/9781315220390>.
- [25] D.M. Rowe, ed., *CRC Handbook of Thermoelectrics*, 1st Editio, CRC Press, 1995.

- [26] H. Werheit, Boron Compounds, in: O. Madelung (Ed.), Landolt-Börnstein, Numer. Data Funct. Relationships Sci. Technol. Gr. III, Vol. 41 D, Springer, Berlin, 2000: pp. 1–491.
- [27] H. Werheit, Boron and Boron-Rich Compounds, in: Y. Kumashiro (Ed.), Electr. Refract. Mater., Marcel Dekker Inc., New York, 2000: pp. 589–653.
- [28] M.I. Fedorov, A.E. Engalychev, V.K. Zaitsev, A.E. Kaliazin, F.Y. Solomkin, Universal thermoelectric unit, AIP Conf. Proc. 316 (1994) 324–327. doi:10.1063/1.46825.
- [29] T. Mori, T. Nishimura, K. Yamaura, E. Takayama-Muromachi, High temperature thermoelectric properties of a homologous series of n-type boron icosahedra compounds: A possible counterpart to p-type boron carbide, J. Appl. Phys. 101 (2007) 093714. doi:10.1063/1.2730571.
- [30] S. Maruyama, Y. Miyazaki, K. Hayashi, T. Kajitani, T. Mori, Excellent p-n control in a high temperature thermoelectric boride, Appl. Phys. Lett. 101 (2012) 152101. doi:10.1063/1.4758297.
- [31] R. Schmechel, H. Werheit, Correlation between structural defects and electronic properties of icosahedral boron-rich solids, J. Phys. Condens. Matter. 11 (1999) 6803–6813. doi:10.1088/0953-8984/11/35/316.
- [32] R. Schmechel, H. Werheit, Structural Defects of Some Icosahedral Boron-Rich Solids and Their Correlation with the Electronic Properties, J. Solid State Chem. 154 (2000) 61–67. doi:10.1006/jssc.2000.8812.
- [33] H. Werheit, On the Electronic Properties of Icosahedral Boron-Rich Solids, in: Mater. Sci. Carbides, Nitrides Borides, Springer Netherlands, Dordrecht, 1999: pp. 65–86. doi:10.1007/978-94-011-4562-6\_5.
- [34] H.C. Longuet-Higgins, M.D. V Roberts, H.J. Emeleus, The electronic structure of an icosahedron of boron atoms, Proc. R. Soc. London. Ser. A. Math. Phys. Sci. 230 (1955) 110–119. doi:10.1098/rspa.1955.0115.
- [35] D. Emin, Unusual properties of icosahedral boron-rich solids, J. Solid State Chem. 179 (2006) 2791–2798. doi:10.1016/J.JSSC.2006.01.014.
- [36] D. Emin, Bonding and doping of simple icosahedral-boride semiconductors, J. Solid State Chem. 177 (2004) 1619–1623. doi:10.1016/J.JSSC.2003.12.017.
- [37] O.A. Golikova, Semiconductors with Complex Lattice and the Amorphization Problem, Phys. Status Solidi. 101 (1987) 277–314. doi:10.1002/pssa.2211010202.
- [38] D.G. Cahill, H.E. Fischer, S.K. Watson, R.O. Pohl, G.A. Slack, Thermal properties of boron and borides, Phys. Rev. B. 40 (1989) 3254–3260. doi:10.1103/PhysRevB.40.3254.

- [39] G.A. Slack, D.W. Oliver, F.H. Hornt, Thermal Conductivity of Boron and Some Boron Compounds\*, *Phys. Rev. B.* 4 (1971) 1714–1720. <https://journals.aps.org/prb/pdf/10.1103/PhysRevB.4.1714> (accessed March 25, 2019).
- [40] H.K. Kim, T. Nakayama, J. Shimizu, K. Kimura, Effects of Metal Doping on Thermoelectric Properties of Arc-Melted and Hot-Pressed  $\beta$ -Rhombohedral Boron, *Mater. Trans.* 49 (2008) 593–599. doi:10.2320/matertrans.E-MRA2007890.
- [41] T. Akashi, T. Itoh, I. Gunjishima, H. Masumoto, T. Goto, Thermoelectric Properties of Hot-pressed Boron Suboxide ( $B_6O$ ), *Mater. Trans.* 43 (2002) 1719–1723. doi:10.2320/matertrans.43.1719.
- [42] J.-L. Innocent, D. Portehault, G. Gouget, S. Maruyama, I. Ohkubo, T. Mori, Thermoelectric properties of boron carbide/HfB<sub>2</sub> composites, *Mater. Renew. Sustain. Energy.* 6 (2017) 1–7. doi:10.1007/s40243-017-0090-8.
- [43] M.A. Hossain, I. Tanaka, T. Tanaka, A.U. Khan, T. Mori, Crystal growth and anisotropy of high temperature thermoelectric properties of yttrium borosilicide single crystals, *J. Solid State Chem.* 233 (2016) 1–7. doi:10.1016/J.JSSC.2015.10.006.
- [44] A. Prytuliak, S. Maruyama, T. Mori, Anomalous effect of vanadium boride seeding on thermoelectric properties of YB<sub>22</sub>C<sub>2</sub>N, *Mater. Res. Bull.* 48 (2013) 1972–1977. doi:10.1016/j.materresbull.2013.01.043.
- [45] A.U. Seybolt, An exploration of high boron alloys, *Trans. Am. Soc. Met.* 52 (1960) 971–989.
- [46] S.M. Richards, J.S. Kaspar, The crystal structure of YB<sub>66</sub>, *Acta Crystallogr. B.* 25 (1969) 237–251. doi:10.1107/S056774086900207X.
- [47] G.A. Slack, D.W. Oliver, G.D. Brower, J.D. Young, Properties of melt-grown single crystals of “YB<sub>68</sub>,” *J. Phys. Chem. Solids.* 38 (1977) 45–49. doi:10.1016/0022-3697(77)90144-5.
- [48] I. Higashi, K. Kobayashi, T. Tanaka, Y. Ishizawa, Structure Refinement of YB<sub>62</sub> and YB<sub>56</sub> of the YB<sub>66</sub>-Type Structure, *J. Solid State Chem.* 133 (1997) 16–20. doi:10.1006/jssc.1997.7308.
- [49] T. Tanaka, K. Kamiya, T. Numazawa, A. Sato, S. Takenouchi, The effect of transition metal doping on thermal conductivity of YB<sub>66</sub>, *Zeitschrift Für Krist. - Cryst. Mater.* 221 (2006) 472–476. doi:10.1524/zkri.2006.221.5-7.472.
- [50] K. Schwetz, P. Ettmayer, R. Kieffer, A. Lipp, Über die Hektoboridphasen der Lanthaniden und Aktiniden, *J. Less Common Met.* 26 (1972) 99–104. doi:10.1016/0022-5088(72)90012-4.
- [51] D.W. Oliver, G.D. Brower, Growth of single crystal YB<sub>66</sub> from the melt, *J. Cryst. Growth.* 11 (1971) 185–190. doi:10.1016/0022-0248(71)90083-2.

- [52] D.W. Oliver, G.D. Brower, F.H. Horn, Cold metal crucible system for synthesis, zone refining, and Czochralski crystal growth of refractory metals and semiconductors, *J. Cryst. Growth.* 12 (1972) 125–131. doi:[https://doi.org/10.1016/0022-0248\(72\)90041-3](https://doi.org/10.1016/0022-0248(72)90041-3).
- [53] D.W. Oliver, G.D. Brower, F.H. Horn, Cold metal crucible system for synthesis, zone refining, and Czochralski crystal growth of refractory metals and semiconductors, *J. Cryst. Growth.* 12 (1972) 125–131. doi:10.1016/0022-0248(72)90041-3.
- [54] O.A. Golikova, A. Tadzhiev, Electrical properties of MB<sub>66</sub> compounds, *J. Less Common Met.* 82 (1981) 169–171. doi:10.1016/0022-5088(81)90215-0.
- [55] T. Mori, T. Tanaka, High temperature thermoelectric properties of heavily Nb-doped YB<sub>66</sub> single crystals, 2005. doi:10.1109/ICT.2005.1519964.
- [56] T. Mori, T. Tanaka, Effect of transition metal doping and carbon doping on thermoelectric properties of YB<sub>66</sub> single crystals, *J. Solid State Chem.* 179 (2006) 2889–2894. doi:10.1016/J.JSSC.2006.01.064.
- [57] H.K. Clark, J.L. Hoard, The Crystal Structure of Boron Carbide, *J. Am. Chem. Soc.* 65 (1943) 2115–2119. doi:10.1021/ja01251a026.
- [58] G. Will, K.H. Kossobutzki, An X-ray diffraction analysis of boron carbide, B<sub>13</sub>C<sub>2</sub>, *J. Less Common Met.* 47 (1976) 43–48. doi:[https://doi.org/10.1016/0022-5088\(76\)90072-2](https://doi.org/10.1016/0022-5088(76)90072-2).
- [59] K.A. Schwetz, P. Karduck, Investigations in the boron-carbon system with the aid of electron probe microanalysis, *J. Less Common Met.* 175 (1991) 1–11. doi:[https://doi.org/10.1016/0022-5088\(91\)90345-5](https://doi.org/10.1016/0022-5088(91)90345-5).
- [60] P.F. Rogl, J. Vřešťál, T. Tanaka, S. Takenouchi, The B-rich side of the B–C phase diagram, *Calphad.* 44 (2014) 3–9. doi:10.1016/J.CALPHAD.2013.07.016.
- [61] M. Bouchacourt, F. Thevenot, Analytical Investigations in the B-C System, *J. Less Common Met.* 82 (1981) 219–226.
- [62] V. Domnich, S. Reynaud, R.A. Haber, M. Chhowalla, Boron Carbide: Structure, Properties, and Stability under Stress, *J. Am. Ceram. Soc.* 94 (2011) 3605–3628. doi:10.1111/j.1551-2916.2011.04865.x.
- [63] I. Gunjishima, T. Akashi, T. Goto, Thermoelectric Properties of Single Crystalline B<sub>4</sub>C Prepared by a Floating Zone Method, *Mater. Trans.* 42 (2001) 1445–1450. doi:10.2320/matertrans.42.1445.
- [64] C. Wood, D. Emin, Conduction mechanism in boron carbide, *Phys. Rev. B.* 29 (1984) 4582–4587. doi:10.1103/PhysRevB.29.4582.

- [65] T.L. Aselage, D. Emin, Boron Carbides: Unconventional High-Temperature Thermoelectrics, in: Chem. Phys. Mater. Sci. Thermoelectr. Mater. - Beyond Bismuth Telluride, 2003: pp. 55–70. doi:10.1007/978-1-4419-9278-9\_4.
- [66] T. Goto, J. Li, T. Hirai, Preparation of B-C System Solid Solutions by Arc Melting and their Thermoelectric Properties., J. Japan Soc. Powder Powder Metall. 43 (1996) 306–310. doi:10.2497/jjspm.43.306.
- [67] K. Koumoto, T. Seki, C.H. Pai, H. Yanagida, CVD Synthesis and Thermoelectric Properties of Boron Carbide, J. Ceram. Soc. Japan. 100 (1992) 853–857. doi:10.2109/jcersj.100.853.
- [68] T. Goto, J. Li, T. Hirai, Preparation of B<sub>4</sub>C-TiB<sub>2</sub> System Composites by Arc Melting and their Thermoelectric Properties., J. Japan Soc. Powder Powder Metall. 44 (1997) 60–64. doi:10.2497/jjspm.44.60.
- [69] I. Gunjishima, T. Akashi, T. Goto, Thermoelectric Properties of Directionally Solidified B<sub>4</sub>C-TiB<sub>2</sub> Composites by an FZ Method., J. Japan Soc. Powder Powder Metall. 47 (2000) 1184–1188. doi:10.2497/jjspm.47.1184.
- [70] B. Feng, H.-P. Martin, A. Michaelis, In Situ Preparation and Thermoelectric Properties of B<sub>4</sub>C<sub>1-x</sub> – TiB<sub>2</sub> Composites, J. Electron. Mater. 42 (2013) 2314–2319. doi:10.1007/s11664-012-2413-y.
- [71] J. Li, T. Goto, T. Hirai, Microstructure and Thermoelectric Properties of B<sub>4</sub>C-SiB<sub>n</sub>-Si Composites Prepared by Arc Melting, J. Ceram. Soc. Japan. 106 (1998) 194–197. doi:10.2109/jcersj.106.194.
- [72] J. Li, T. Goto, T. Hirai, Thermoelectric Properties of B<sub>4</sub>C-SiB<sub>n</sub> (n=4, 6, 14) In-situ Composites, Mater. Trans. JIM. 40 (1999) 314–319. doi:10.2320/matertrans1989.40.314.
- [73] K.-. Cai, C.-W. Nan, Y. Paderno, D.. McLachlan, Effect of titanium carbide addition on the thermoelectric properties of B<sub>4</sub>C ceramics, Solid State Commun. 115 (2000) 523–526. doi:10.1016/S0038-1098(00)00245-3.
- [74] K. Cai, C.-W. Nan, The influence of W<sub>2</sub>B<sub>5</sub> addition on microstructure and thermoelectric properties of B<sub>4</sub>C ceramic, Ceram. Int. 26 (2000) 523–527. doi:10.1016/S0272-8842(99)00089-9.
- [75] V. Lankau, H.-P. Martin, R. Hempel-Weber, N. Oeschler, A. Michaelis, Preparation and Thermoelectric Characterization of SiC-B<sub>4</sub>C Composites, J. Electron. Mater. 39 (2010) 1809–1813. doi:10.1007/s11664-010-1129-0.
- [76] F. Heusler, Über magnetische Manganlegierungen, in: Verhandlungen Der Dtsch. Phys. Gesellschaft, 1903: pp. 217–219.

- [77] M. Yin, J. Hasier, • Philip Nash, A review of phase equilibria in Heusler alloy systems containing Fe, Co or Ni, *J. Mater. Sci.* 51 (2016) 50–70. doi:10.1007/s10853-015-9389-y.
- [78] A.J. Bradley, J.W. Rodgers, W.L. Bragg, The crystal structure of the heusler alloys, *Proc. R. Soc. London. Ser. A, Contain. Pap. a Math. Phys. Character.* 144 (1934) 340–359. doi:10.1098/rspa.1934.0053.
- [79] S. Maier, S. Denis, S. Adam, J.-C. Crivello, J.-M. Joubert, E. Alleno, Order-disorder transitions in the  $\text{Fe}_2\text{VAl}$  Heusler alloy, *Acta Mater.* 121 (2016) 126–136. doi:10.1016/J.ACTAMAT.2016.08.080.
- [80] M. Mikami, K. Kobayashi, T. Kawada, K. Kubo, N. Uchiyama, Development of a Thermoelectric Module Using the Heusler Alloy  $\text{Fe}_2\text{VAl}$ , *J. Electron. Mater.* 38 (2009) 1121–1126. doi:10.1007/s11664-009-0724-4.
- [81] H. Kato, M. Kato, Y. Nishino, U. Mizutani, S. Asano, Effect of Silicon Substitution on Thermoelectric Properties of Heusler-type  $\text{Fe}_2\text{VAl}$  Alloy, *J. Japan Inst. Met.* 65 (2001) 652–656. doi:10.2320/jinstmet1952.65.7\_652.
- [82] Y. Nishino, H. Kato, M. Kato, U. Mizutani, Effect of off-stoichiometry on the transport properties of the Heusler-type  $\text{Fe}_2\text{VAl}$  compound, *Phys. Rev. B.* 63 (2001) 233303 (4). doi:10.1103/PhysRevB.63.233303.
- [83] C.S. Lue, Y.-K. Kuo, Thermoelectric properties of the semimetallic Heusler compounds  $\text{Fe}_{2-x}\text{V}_{1+x}\text{M}$  ( $\text{M} = \text{Al}, \text{Ga}$ ), *Phys. Rev. B.* 66 (2002) 085121(5). doi:10.1103/PhysRevB.66.085121.
- [84] H. Okamura, J. Kawahara, T. Nanba, S. Kimura, K. Soda, U. Mizutani, Y. Nishino, M. Kato, I. Shimoyama, H. Miura, K. Fukui, K. Nakagawa, H. Nakagawa, T. Kinoshita, Pseudogap Formation in the Intermetallic Compounds  $(\text{Fe}_{1-x}\text{V}_x)_3\text{Al}$ , *Phys. Rev. Lett.* 84 (2000) 3674–3677. doi:10.1103/PhysRevLett.84.3674.
- [85] D.J. Singh, I.I. Mazin, Electronic structure, local moments, and transport in  $\text{Fe}_2\text{VAl}$ , *Phys. Rev. B.* 57 (1998) 14352–14356.
- [86] H. Matsuura, Y. Nishino, U. Mizutani, S. Asano, Doping Effects on Thermoelectric Properties of the Pseudogap  $\text{Fe}_2\text{VAl}$  System, *J. Japan Inst. Met.* 66 (2002) 767–771. doi:10.2320/jinstmet1952.66.7\_767.
- [87] E.J. Skoug, C. Zhou, Y. Pei, D.T. Morelli, High Thermoelectric Power Factor Near Room Temperature in Full-Heusler Alloys, *J. Electron. Mater.* 38 (2009) 1221–1223. doi:10.1007/s11664-008-0626-x.
- [88] K. Renard, A. Mori, Y. Yamada, S. Tanaka, H. Miyazaki, Y. Nishino, Thermoelectric properties of the Heusler-type  $\text{Fe}_2\text{VTa}_x\text{Al}_{1-x}$  alloys, *J. Appl. Phys.* 115 (2014) 033707. doi:10.1063/1.4861419.

- [89] T. Mori, N. Ide, Y. Nishino, Thermoelectric Properties of p-Type  $\text{Fe}_2\text{V}_{1-x-y}\text{Ti}_x\text{Ta}_y\text{Al}$  Alloys, *J. Japan Inst. Met.* 72 (2008) 593–598. doi:10.2320/jinstmet.72.593.
- [90] M. Mikami, M. Inukai, H. Miyazaki, Y. Nishino, Effect of Off-Stoichiometry on the Thermoelectric Properties of Heusler-Type  $\text{Fe}_2\text{VAl}$  Sintered Alloys, *J. Electron. Mater.* 45 (2016) 1284–1289. doi:10.1007/s11664-015-3999-7.
- [91] Y. Nishino, S. Deguchi, U. Mizutani, thermal and transport properties of the Heusler-type  $\text{Fe}_2\text{VAl}_{1-x}\text{Ge}_x$  ( $0 \leq x \leq 0.20$ ) alloys: Effect of doping on lattice thermal conductivity, electrical resistivity, and Seebeck coefficient, *Phys. Rev. B.* 74 (2006) 115115-1–6. doi:10.1103/PhysRevB.74.115115.
- [92] S. Masuda, K. Tsuchiya, J. Qiang, H. Miyazaki, Y. Nishino, Effect of high-pressure torsion on the microstructure and thermoelectric properties of  $\text{Fe}_2\text{VAl}$ -based compounds, *J. Appl. Phys.* 124 (2018) 035106. doi:10.1063/1.5034390.
- [93] M. Mikami, Y. Kinemuchi, K. Ozaki, Y. Terazawa, T. Takeuchi, Thermoelectric properties of tungsten-substituted Heusler  $\text{Fe}_2\text{VAl}$  alloy, *J. Appl. Phys.* 111 (2012) 093710. doi:10.1063/1.4710990.
- [94] S.M. Koohpayeh, D. Fort, J.S. Abell, The optical floating zone technique: A review of experimental procedures with special reference to oxides, *Prog. Cryst. Growth Charact. Mater.* 54 (2008) 121–137. doi:10.1016/J.PCRYSGROW.2008.06.001.
- [95] T. Tanaka, S. Otani, Y. Ishizawa, Preparation of single crystals of  $\text{YB}_{66}$ , *J. Cryst. Growth.* 73 (1985) 31–36. doi:10.1016/0022-0248(85)90326-4.
- [96] T. Tanaka, S. Otani, Y. Ishizawa, Growth of high quality single crystals of  $\text{YB}_{66}$ , *J. Cryst. Growth.* 99 (1990) 994–997. doi:10.1016/S0022-0248(08)80069-3.
- [97] T. Tanaka, Z.U. Rek, J. Wong, M. Rowen, FZ crystal growth of monochromator-grade  $\text{YB}_{66}$  single crystals as guided by topographic and double-crystal diffraction characterization, *J. Cryst. Growth.* 192 (1998) 141–151. doi:10.1016/S0022-0248(98)00400-X.
- [98] T. Tanaka, A. Sato, S. Takenouchi, K. Kamiya, T. Numazawa, Floating-zone crystal growth of Nb-doped  $\text{YB}_{66}$  for soft X-ray monochromator use, *J. Cryst. Growth.* 275 (2005) e1889–e1893. doi:10.1016/J.JCRYSGRO.2004.11.270.
- [99] R. Hermann, J. Priede, G. Gerbeth, 8 - Floating Zone Growth of Oxides and Metallic Alloys, in: P.B.T.-H. of C.G. (Second E. Rudolph (Ed.), *Handb. Cryst. Growth*, Elsevier, Boston, 2015: pp. 281–329. doi:https://doi.org/10.1016/B978-0-444-63303-3.00008-0.
- [100] A. Zevalkink, <https://alexzevalkink.wordpress.com/research/>, (2020).

- [101] M. Suarez, A. Fernandez, J.L. Menendez, R. Torrecillas, H. U., J. Hennicke, R. Kirchner, T. Kessel, Challenges and Opportunities for Spark Plasma Sintering: A Key Technology for a New Generation of Materials, *J. Mater. Scien.* (2013) 319–342. doi:10.5772/53706.
- [102] Z.A. Munir, U. Anselmi-Tamburini, M. Ohyanagi, The Effect of Electric Field and Pressure on the Synthesis and Consolidation of Materials: A Review of the Spark Plasma Sintering Method, *J. Mater. Sci.* 41 (2006) 763–777. doi:10.1007/s10853-006-6555-2.
- [103] E. Alleno, D. Bérardan, C. Byl, C. Candolfi, R. Daou, R. Decourt, E. Guilmeau, S. Hébert, J. Hejtmanek, B. Lenoir, P. Masschelein, V. Ohorodnichuk, M. Pollet, S. Populoh, D. Ravot, O. Rouleau, M. Soulier, Invited Article: A round robin test of the uncertainty on the measurement of the thermoelectric dimensionless figure of merit of  $\text{Co}_{0.97}\text{Ni}_{0.03}\text{Sb}_3$ , *Rev. Sci. Instrum.* 86 (2015) 011301. doi:10.1063/1.4905250.
- [104] K.A. Borup, J. de Boor, H. Wang, F. Drymiotis, F. Gascoin, X. Shi, L. Chen, M.I. Fedorov, E. Müller, B.B. Iversen, G.J. Snyder, Measuring thermoelectric transport properties of materials, *Energy Environ. Sci.* 8 (2015) 423–435. doi:10.1039/C4EE01320D.
- [105] W.J. Parker, R.J. Jenkins, C.P. Butler, G.L. Abbott, Flash Method of Determining Thermal Diffusivity, Heat Capacity, and Thermal Conductivity, *J. Appl. Phys.* 32 (1961) 1679–1684. doi:10.1063/1.1728417.
- [106] J.J. Zajas, P. Heiselberg, Measurements of thermal diffusivity, specific heat capacity and thermal conductivity with LFA 447 apparatus, Aarlborg, 2013.
- [107] Laser Flash TC-7000 User manual, ULVAC-RIKO, Inc., n.d.
- [108] P. Sauerschnig, J.L. Watts, J.B. Vaney, P.C. Talbot, J.A. Alarco, I.D.R. Mackinnon, T. Mori, Thermoelectric properties of phase pure boron carbide prepared by a solution-based method, *Adv. Appl. Ceram.* 119 (2020) 97–106. doi:10.1080/17436753.2019.1705017.
- [109] M.J. O'Neill, Measurement of Specific Heat Functions by Differential Scanning Calorimetry., *Anal. Chem.* 38 (1966) 1331–1336. doi:10.1021/ac60242a011.
- [110] A.B. Spierings, M. Schneider, R. Eggenberger, Comparison of density measurement techniques for additive manufactured metallic parts, *Rapid Prototyp. J.* 17 (2011) 380–386. doi:10.1108/13552541111156504.
- [111] M. McElfresh, *Fundamentals of Magnetism and Magnetic Measurements*, (1994) 34.
- [112] B.D. Josephson, Possible new effects in superconductive tunnelling, *Phys. Lett.* 1 (1962) 251–253. doi:https://doi.org/10.1016/0031-9163(62)91369-0.

- [113] H. Werheit, K. de Groot, W. Malkemper, T. Lundström, On n-type  $\beta$  rhombohedral boron, *J. Less Common Met.* 82 (1981) 163–168. doi:10.1016/0022-5088(81)90214-9.
- [114] U. Kuhlmann, H. Werheit, T. Dose, T. Lundström, Influence of interstitially soluted iron on structural, optical and electrical properties of  $\beta$ -rhombohedral boron, *J. Alloys Compd.* 186 (1992) 187–200. doi:10.1016/0925-8388(92)90004-S.
- [115] H. Kim, K. Kimura, Vanadium Concentration Dependence of Thermoelectric Properties of beta-Rhombohedral Boron Prepared by Spark Plasma Sintering, *Mater. Trans.* 52 (2011) 41–48. doi:10.2320/matertrans.M2010272.
- [116] T. Mori, T. Nishimura, Thermoelectric properties of homologous p- and n-type boron-rich borides, *J. Solid State Chem.* 179 (2006) 2908–2915. doi:10.1016/J.JSSC.2006.03.030.
- [117] T. Mori, T. Nishimura, K. Yamaura, E. Takayama-Muromachi, High temperature thermoelectric properties of a homologous series of n-type boron icosahedra compounds: A possible counterpart to p-type boron carbide, *J. Appl. Phys.* 101 (2007) 093714. doi:10.1063/1.2730571.
- [118] T. Mori, T. Nishimura, W. Schnelle, U. Burkhardt, Y. Grin, The origin of the n-type behavior in rare earth borocarbide  $Y_{1-x}B_{28.5}C_4$ , *Dalt. Trans.* 43 (2014) 15048–15054. doi:10.1039/C4DT01303D.
- [119] T. Mori, High temperature thermoelectric properties of  $B_{12}$  icosahedral cluster-containing rare earth boride crystals, *J. Appl. Phys.* 97 (2005) 093703. doi:10.1063/1.1883726.
- [120] M.M. Korsukova, V.N. Gurin, Y.B. Kuzma, N.F. Chaban, S.I. Chykhrii, V. V. Moshchalkov, N.B. Brandt, A.A. Gippius, K.K. Nyan, Crystal Structure, Electrical, and Magnetic Properties of the New Ternary Compounds  $LnAIB_{14}$ , *Phys. Status Solidi.* 114 (1989) 265–272. doi:10.1002/pssa.2211140126.
- [121] G.A. Slack, K.E. Morgan, Crystallography, semiconductivity, thermoelectricity, and other properties of boron and its compounds, especially  $B_6O$ , *Solid State Sci.* 47 (2015) 43–50. doi:10.1016/j.solidstatesciences.2015.04.007.
- [122] M. Takeda, M. Terui, N. Takahashi, N. Ueda, Improvement of thermoelectric properties of alkaline-earth hexaborides, *J. Solid State Chem.* 179 (2006) 2823–2826. doi:10.1016/J.JSSC.2006.01.025.
- [123] M. Gürsoy, M. Takeda, B. Albert, High-pressure densified solid solutions of alkaline earth hexaborides (Ca/Sr, Ca/Ba, Sr/Ba) and their high-temperature thermoelectric properties, *J. Solid State Chem.* 221 (2015) 191–195. doi:10.1016/j.jssc.2014.10.001.
- [124] F. Iga, Y. Takakuwa, T. Takahashi, M. Kasaya, T. Kasuya, T. Sagawa, XPS study of rare earth dodecaborides:  $TmB_{12}$ ,  $YbB_{12}$  and  $LuB_{12}$ , *Solid State Commun.* 50 (1984) 903–905. doi:10.1016/0038-1098(84)90745-2.

- [125] V. Petříček, M. Dušek, L. Palatinus, Crystallographic Computing System JANA2006: General features, *Zeitschrift Für Krist. - Cryst. Mater.* 229 (2014) 345–352. doi:10.1515/zkri-2014-1737.
- [126] O. Sologub, L.P. Salamakha, B. Stöger, P.F. Rogl, T. Mori, G. Eguchi, H. Michor, E. Bauer, On the boron rich phases in the Yb-B system, *J. Solid State Chem.* 255 (2017) 172–177. doi:10.1016/J.JSSC.2017.08.007.
- [127] P. Sauerschnig, K. Tsuchiya, T. Tanaka, Y. Michiue, O. Sologub, S. Yin, A. Yoshikawa, T. Shishido, T. Mori, On the thermoelectric and magnetic properties, hardness, and crystal structure of the higher boride YbB<sub>66</sub>, *J. Alloys Compd.* 813 (2020) 152182. doi:10.1016/J.JALLCOM.2019.152182.
- [128] K.E. Spear, G.I. Solovyev, High Boron Content Rare-Earth Borides, *NIST Spec. Publ. Solid State Chem. Proc. 5th Mater. Res. Symp.* (1972) 597.
- [129] V.V. Novikov, D.V. Avdashchenko, S.L. Bud'ko, N.V. Mitroshenkov, A.V. Matovnikov, H. Kim, M.A. Tanatar, R. Prozorov, Spin glass and glass-like lattice behaviour in HoB<sub>66</sub> at low temperatures, *Philos. Mag.* 93 (2013) 1110–1123. doi:10.1080/14786435.2012.739291.
- [130] J.I. Hoppe, Effective magnetic moment, *J. Chem. Educ.* 49 (1972) 505. doi:10.1021/ed049p505.
- [131] C. Kittel, *Introduction to Solid State Physics*, 8th Edition, Wiley, 2004.
- [132] J. Etourneau, Critical Survey of Rare-Earth Borides: Occurrence, Crystal Chemistry and Physical Properties, *J. Less-Common Met.* 110 (1985) 267–281. doi:10.1016/0022-5088(85)90333-9.
- [133] H. Kim, S.L. Bud'ko, M.A. Tanatar, D. V Avdashchenko, A. V Matovnikov, N. V Mitroshenkov, V. V Novikov, R. Prozorov, Magnetic Properties of RB<sub>66</sub> (R = Gd, Tb, Ho, Er, and Lu), *J. Supercond. Nov. Magn.* 25 (2012) 2371–2375. doi:10.1007/s10948-012-1610-5.
- [134] T. Mori, T. Tanaka, Effect of transition metal doping and carbon doping on thermoelectric properties of YB<sub>66</sub> single crystals, *J. Solid State Chem.* 179 (2006) 2889–2894. doi:10.1016/j.jssc.2006.01.064.
- [135] T. Mori, High temperature thermoelectric properties of B<sub>12</sub> icosahedral cluster-containing rare earth boride crystals, *J. Appl. Phys.* 97 (2005) 093703. doi:10.1063/1.1883726.
- [136] N.F. Mott, E.A. Davis, *Electronic processes in non-crystalline materials*, Oxford University Press, 2012.
- [137] N. Mott, *Metal-Insulator Transitions*, 2nd ed., CRC Press, 1990. doi:10.1201/b12795.
- [138] B.I. Shklovskii, A.L. Efros, *Electronic Properties of Doped Semiconductors*, Springer Berlin Heidelberg, Berlin, Heidelberg, 1984. doi:10.1007/978-3-662-02403-4.

- [139] I.P. Zvyagin, On the Theory of Hopping Transport in Disordered Semiconductors, *Phys. Status Solidi*. 58 (1973) 443–449. doi:10.1002/pssb.2220580203.
- [140] O.E. Parfenov, F.A. Shklyaruk, On the Temperature Dependence of the Thermoelectric Power in Disordered Semiconductors, *Semiconductors*. 41 (2007) 1021–1026. doi:10.1134/S1063782607090035.
- [141] T. Mori, D. Berthebaud, T. Nishimura, A. Nomura, T. Shishido, K. Nakajima, Effect of Zn doping on improving crystal quality and thermoelectric properties of borosilicides, *Dalt. Trans.* 39 (2010) 1027–1030. doi:10.1039/B916028K.
- [142] G.I. Solovyev, K.E. Spear, Phase Behavior in the Sm-B System, *J. Am. Ceram. Soc.* 55 (1972) 475–479. doi:10.1111/j.1151-2916.1972.tb11344.x.
- [143] D. Berthebaud, T. Nishimura, T. Mori, Thermoelectric properties and spark plasma sintering of doped  $\text{YB}_{22}\text{C}_2\text{N}$ , *J. Mater. Res.* 25 (2010) 665–669. doi:10.1557/JMR.2010.0100.
- [144] Rodriguez-Carvajal J, FULLPROF: a program for Rietveld refinement and pattern matching analysis, *Abstr. Satell. Meet. Powder Diffr. XV Congr. Int. Union Crystallogr.* (1990) 127.
- [145] P.K. Liao, K.E. Spear, B-Sm (Boron-Samarium). *Binary Alloy Phase Diagrams*, Second Edition, Ed. T.B. Massalski, ASM International, 1990.
- [146] P.K. Liao, K.E. Spear, B-Yb (Boron-Ytterbium), in: T.B. Massalski (Ed.), *Bin. Alloy Phase Diagrams*, 2nd Editio, 1990: pp. 557–559.
- [147] O. Sologub, L. Salamakha, B. Stöger, Y. Michiue, T. Mori, Zr doped  $\beta$ -rhombohedral boron: Widely variable Seebeck coefficient and structural properties, *Acta Mater.* 122 (2017) 378–385. doi:10.1016/J.ACTAMAT.2016.10.014.
- [148] J.-N. Chazalviel, M. Campagna, G.K. Wertheim, P.H. Schmidt, Study of valence mixing in  $\text{SmB}_6$  by x-ray photoelectron spectroscopy, *Phys. Rev. B.* 14 (1976) 4586–4592. <https://journals.aps.org/prb/pdf/10.1103/PhysRevB.14.4586> (accessed April 5, 2019).
- [149] N. Heming, U. Treske, M. Knupfer, B. Büchner, D.S. Inosov, N.Y. Shitsevalova, V.B. Filipov, S. Krause, A. Koitzsch, Surface properties of  $\text{SmB}_6$  from x-ray photoelectron spectroscopy, (2015). doi:10.1103/PhysRevB.90.195128.
- [150] T. Mori, T. Tanaka, Magnetic properties of terbium  $\text{B}_{12}$  icosahedral boron-rich compounds, *J. Phys. Soc. Japan.* 68 (1999) 2033–2039. doi:10.1143/JPSJ.68.2033.
- [151] K. Flachbart, S. Gabani, T. Mori, K. Siemensmeyer, Magnetic Ordering in Boron-Rich Borides  $\text{TbB}_{66}$  and  $\text{GdB}_{66}$ , *ACTA Phys. Pol. A.* 118 (2010) 875–876.

- [152] T. Tanaka, Y. Shi, T. Mori, A. Leithe-Jasper, Effect of Transition Metal Doping in  $\text{YB}_{66}$ , *J. Solid State Chem.* 154 (2000) 54–60. doi:10.1006/jssc.2000.8811.
- [153] T. Mori, T. Nishimura, Thermoelectric properties of homologous p- and n-type boron-rich borides, *J. Solid State Chem.* 179 (2006) 2908–2915. doi:10.1016/J.JSSC.2006.03.030.
- [154] T. Mori, J. Martin, G. Nolas, Thermal conductivity of  $\text{YbB}_{44}\text{Si}_2$ , *J. Appl. Phys.* 102 (2007) 073510. doi:10.1063/1.2785017.
- [155] V. V. Novikov, D. V. Avdashchenko, A. V. Matovnikov, N. V. Mitroshenkov, S.L. Bud'ko, Heat capacity and thermal expansion of icosahedral lutetium boride  $\text{LuB}_{66}$ , *J. Therm. Anal. Calorim.* 116 (2014) 765–769. doi:10.1007/s10973-013-3593-2.
- [156] A.K. Suri, C. Subramanian, J.K. Sonber, T.S.R.C. Murthy, Synthesis and consolidation of boron carbide: a review, *Int. Mater. Rev.* 55 (2010) 4–40. doi:10.1179/095066009X12506721665211.
- [157] Joshua L. Watts, Peter C. Talbot, Jose A. Alarco, Ian D. R. Mackinnon, In-Situ Carbon Control in the Preparation of Precursors to Boron Carbide by a Non-Aqueous Solution Technique, *J. Mater. Sci. Eng. A.* 5 (2015) 8–20. doi:10.17265/2161-6213/2015.1-2.002.
- [158] A. Sinha, T. Mahata, B.. Sharma, Carbothermal route for preparation of boron carbide powder from boric acid–citric acid gel precursor, *J. Nucl. Mater.* 301 (2002) 165–169. doi:10.1016/S0022-3115(02)00704-3.
- [159] I. Yanase, R. Ogawara, H. Kobayashi, Synthesis of boron carbide powder from polyvinyl borate precursor, *Mater. Lett.* 63 (2009) 91–93. doi:10.1016/J.MATLET.2008.09.012.
- [160] M. Kakiage, Y. Tominaga, I. Yanase, H. Kobayashi, Synthesis of boron carbide powder in relation to composition and structural homogeneity of precursor using condensed boric acid–polyol product, *Powder Technol.* 221 (2012) 257–263. doi:10.1016/J.POWTEC.2012.01.010.
- [161] J.L. Watts, P.C. Talbot, J.A. Alarco, I.D.R. Mackinnon, Morphology control in high yield boron carbide, *Ceram. Int.* 43 (2017) 2650–2657. doi:10.1016/J.CERAMINT.2016.11.076.
- [162] S. Sasaki, M. Takeda, K. Yokoyama, T. Miura, T. Suzuki, H. Suematsu, W. Jiang, K. Yatsui, Thermoelectric properties of boron-carbide thin film and thin film based thermoelectric device fabricated by intense-pulsed ion beam evaporation, *Sci. Technol. Adv. Mater.* 6 (2005) 181–184. doi:10.1016/j.stam.2004.11.010.
- [163] B. Feng, H.-P. Martin, F.-D. Börner, W. Lippmann, M. Schreier, K. Vogel, A. Lenk, I. Veremchuk, M. Dannowski, C. Richter, P. Pfeiffer, G. Zikoridse, H. Lichte, J. Grin, A. Hurtado, A. Michaelis, Manufacture and Testing of Thermoelectric Modules Consisting of  $\text{B}_x\text{C}$  and  $\text{TiO}_x$  Elements, *Adv. Eng. Mater.* 16 (2014) 1252–1263. doi:10.1002/adem.201400183.

- [164] T.L. Aselage, R.G. Tisot, Lattice Constants of Boron Carbides, *J. Am. Ceram. Soc.* 75 (1992) 2207–2212. doi:10.1111/j.1151-2916.1992.tb04485.x.
- [165] K. Rasim, R. Ramlau, A. Leithe-Jasper, T. Mori, U. Burkhardt, H. Borrmann, W. Schnelle, C. Carbogno, M. Scheffler, Y. Grin, Local Atomic Arrangements and Band Structure of Boron Carbide, *Angew. Chemie Int. Ed.* 57 (2018) 6130–6135. doi:10.1002/anie.201800804.
- [166] K. Kirihaara, M. Mukaida, Y. Shimizu, Electrical transport and thermoelectric properties of boron carbide nanowires, *Nanotechnology.* 28 (2017) 145404. doi:10.1088/1361-6528/aa610c.
- [167] A.J.E. Rettie, W.D. Chemelewski, D. Emin, C.B. Mullins, Unravelling Small-Polaron Transport in Metal Oxide Photoelectrodes, *J. Phys. Chem. Lett.* 7 (2016) 471–479. doi:10.1021/acs.jpcclett.5b02143.
- [168] C. Wood, D. Emin, P.E. Gray, Thermal conductivity behavior of boron carbides, *Phys. Rev. B.* 31 (1985) 6811–6814. doi:10.1103/PhysRevB.31.6811.
- [169] D.S. Smith, A. Alzina, J. Bourret, B. Nait-Ali, F. Pennec, N. Tessier-Doyen, K. Otsu, H. Matsubara, P. Elser, U.T. Gonzenbach, Thermal conductivity of porous materials, *J. Mater. Res.* 28 (2013) 2260–2272. doi:10.1557/jmr.2013.179.
- [170] T. Moriya, Y. Takahashi, Spin Fluctuations in Itinerant Electron Magnetism, *Le J. Phys. Colloq.* 39 (1978) C6-1466-C6-1471. doi:10.1051/jphyscol:19786588.
- [171] T. Okabe, Spin-fluctuation drag thermopower of nearly ferromagnetic metals, *J. Phys. Condens. Matter.* 22 (2010) 115604. doi:10.1088/0953-8984/22/11/115604.
- [172] Y. Nishino, M. Kato, S. Asano, K. Soda, M. Hayasaki, U. Mizutani, Semiconductorlike Behavior of Electrical Resistivity in Heusler-type  $\text{Fe}_2\text{VAl}$  Compound, *Phys. Rev. Lett.* 79 (1997) 1909–1912.
- [173] H. Miyazaki, K. Renard, M. Inukai, K. Soda, Y. Nishino, Electronic structure of Heusler-type  $\text{Fe}_2\text{V}_{1+x}\text{Al}_{1-x}$  thermoelectric materials, *J. Electron Spectros. Relat. Phenomena.* 195 (2014) 185–188. doi:10.1016/J.ELSPE.2014.07.007.
- [174] I. Knapp, B. Budinska, D. Milosavljevic, P. Heinrich, S. Khmelevskiy, R. Moser, R. Podloucky, P. Prenzinger, E. Bauer, Impurity band effects on transport and thermoelectric properties of  $\text{Fe}_{2-x}\text{Ni}_x\text{VAl}$ , *Phys. Rev. B.* 96 (2017) 45204. doi:10.1103/PhysRevB.96.045204.